1992

The characterization of organic monolayers at gold surfaces using scanning tunneling microscopy and atomic force microscopy: Correlation with macrostructural properties

Carla Ann Alves
Iowa State University

Order Number 9301994

The characterization of organic monolayers at gold surfaces using scanning tunneling microscopy and atomic force microscopy: Correlation with macrostructural properties

Alves, Carla Ann, Ph.D.

Iowa State University, 1992

U·M·I
300 N. Zeeb Rd.
Ann Arbor, MI 48106

The characterization of organic monolayers at gold surfaces using scanning tunneling microscopy and atomic force microscopy: Correlation with macrostructural properties

by

Carla Ann Alves

A Dissertation Submitted to the
Graduate Faculty in Partial Fulfillment of the
Requirements for the Degree of
DOCTOR OF PHILOSOPHY

Department: Chemistry
Major: Analytical Chemistry

Approved:

Signature was redacted for privacy.

In Charge of Major Work

Signature was redacted for privacy.

For the Major Department

Signature was redacted for privacy.

For the Graduate College

Iowa State University
Ames, Iowa

1992

TABLE OF CONTENTS

ACKNOWLEDGMENTS

First, I would like to thank my major professor, Dr. Marc Porter, for his guidance and endless supply of new research ideas. He has taught me that, sometimes, the seemingly impossible is not so and that perseverance almost always pays off, except when using an LB trough. I would also like to thank my other colleagues, including the Porter group members, past and present. In particular, I am grateful to Dr. Cindra Widrig for her unique insights into problems as well as helpful suggestions. Also, the comradeship of Earl Smith and Darwin Popenoe made the sometimes tedious task of research less so, and was an invaluable source of helpful suggestions.

For all of his day-to-day support and encouragement, I thank my husband Luis. He not only shared my joy but also my disappointments, and made the frequently encountered stressful situations more bearable. I also appreciate the constant support of my dad and mom and the rest of my family through all of my academic endeavors.

Lastly, but not least, I want to thank my high school chemistry teachers, especially Ron Crampton, for making chemistry fun and sparking an interest in chemisty that has led me to where I am today.

This work was performed at Ames Laboratory under contract no. W-7405-eng-82 with the U.S. Department of Energy. The United States government has assigned the DOE report IS-T 1628 to this thesis.

GENERAL INTRODUCTION

Overview of Dissertation

The microscopic characterization of organic monolayers at Au surfaces was performed primarily using scanning tunneling microscopy (STM) and atomic force microscopy (AFM). The literature review provides basic theory and principles of operation for STM and AFM, as well as providing a literature review of some recent applications of each technique. The remaining papers deal with the experimental results obtained from the characterization of self-assembled thiolate monolayers at Au(111). The STM and AFM were used to investigate the structure of *n*-alkanethiolates at Au(111). The details are presented in Paper 1 (STM) and Paper 2 (AFM). The spatial arrangement of a fluorinated thiol, $CF_3(CF_2)_7(CH_2)_2SH$ is revealed in Paper 3, along with the supporting infrared reflection spectroscopic and electrochemical details. The final paper, Paper 4, describes the apparent oxidation of the thiolate monolayers to elemental sulfur. Again, supporting electrochemical evidence is included. Together, these papers provide the first molecularly-resolved STM and AFM images of the alkane and fluorinated thiolates at Au(111) and reveal their two-dimensional packing arrangements. Following these papers is a general conclusion as well as the list of references for the literature review.

LITERATURE REVIEW AND GENERAL THEORY OF SCANNING TUNNELING MICROSCOPY AND ATOMIC FORCE MICROSCOPY

Introduction

The scanning tunneling microscope (STM) and the atomic force microscope (AFM) are redefining the concept of microscopy. Each is capable of resolving surface detail down to the atomic level. The development of the STM, by Gerd Binnig and Heinrich Rohrer in 1982, provided scientists the first atomically-resolved view of semiconducting[1] surfaces with the possibility for the first time to obtain direct, real-space determinations of surface structure. Only four years later, Binnig and Rohrer shared the Nobel Prize in Physics (1986) for this accomplishment, indicating the perceived importance of the new instrument. The success of STM for achieving atomically resolved images of surfaces triggered the development of a variety of other scanning probe microscopes. Among these, and the most popular, is the AFM. Developed in 1986 by Gerd Binnig, Calvin Quate and Christoph Gerber,[2] AFM has gained a status similar to that of the STM for its atomic-scale imaging capabilities of nonconductive surfaces, something the STM cannot do.

Still in their infancy, these techniques have already established themselves in the hierarchy of surface analytical techniques such as low energy electron diffraction (LEED) and Auger electron spectroscopy (AES) which provide a wealth of information about the surface but are inherently limited to the ultrahigh vacuum (UHV) environment. Although the first

STM experiments were performed under UHV, STM and AFM are capable of achieving atomic resolution in air and in liquid environments, a property which has escalated their use.

Scanning Tunneling Microscopy

Principles of Operation

In scanning tunneling microscopy (STM), an atomically sharp metal tip is placed a few angstroms away from a conducting surface. At this distance, the wave functions of the sample and tip (both decay exponentially in the vacuum barrier) overlap. A bias voltage, V, is applied between the tip and the sample surface and a quantum mechanical tunneling current begins to flow. The tip can be moved in three directions using either three orthogonal piezoelectric drivers or a piezoelectric tube. As will be discussed, the tunneling current depends exponentially on the tip-surface distance, typically varying about an order of magnitude for a 1 Å change in the separation distance. As the tip scans over the surface, topographical changes, such as the presence of a surface step, will appear as changes in the tunneling current or height of the tip, depending on the imaging mode.

There are two imaging modes for STM: constant current and constant height, as illustrated in Figure 1. In the constant current mode (Figure 1(a)), the tip is scanned over the surface while the tunneling current, I_t, is measured. A feedback network changes the height of the tip to maintain a constant current and the tip-surface separation distance remains essentially constant. An image consists of a map of tip height as a function of the lateral

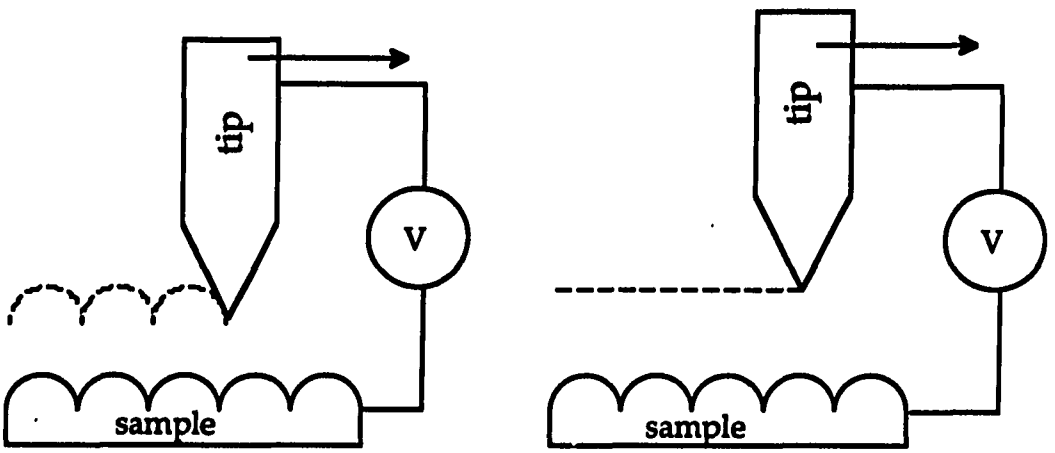

Figure 1. An illustration of two imaging modes available in STM. In (a), the constant current mode is represented and (b) depicts the constant height mode. The dashed lines represent the path of the tip as it scans.

position of the tip on the sample. This mode is the more popular of the two, and can be used to probe surfaces that are not atomically flat.

The second mode of operation for the STM is the constant height mode (Figure 1(b)). Here, the tip is scanned across the surface at a nearly constant height and constant bias voltage, V, while the current is monitored. In this case, the feedback loop responds to maintain the average tunneling current. The rapid variation in the current as the tip passes over features on the surface (atoms) is monitored as a function of the lateral position of the tip and a map of the surface is prepared similarly to that for the constant current mode. The advantage of the constant height mode is that much higher scan rates can be used because only the electronic response, not the z translator (tip height), is changed. Fast imaging, besides decreasing scanning time, minimizes image distortion due to thermal drift and piezoelectric creep.

Theory

Images from STM appear in many cases to be direct topographs of the surface. However, this is not always the case. A discussion of STM theory is required for a more complete understanding and interpretation of the images. The relationship between I_t and V is obtained from the equations for one-dimensional vacuum tunneling at low voltage and temperature:[3]

$$I_t \propto \exp(-2\kappa d) \qquad (1)$$

where κ is the decay constant of the wave functions in the tunneling barrier, and d is the separation between sample and tip. This equation relates the tunneling current to the effective work function of the surface, ϕ, since

$$\kappa = \hbar^{-1}\sqrt{2m\phi} \tag{2}$$

where $\hbar$ is Planck's constant divided by 2π, and m is the mass of an electron.

Using a typical work function of 4 eV and a κ of 1.0 $Å^{-1}$, the tunneling current changes by an order of magnitude for a 1 Å change in separation, d. If the current is kept constant (± 2%) then d will be constant to within ± 0.01 Å. This approach leads one to conclude that a topographical map of the surface is obtained. However, it is uncertain what distance d actually represents. The tunneling involves Fermi level states which have very complex spatial structures, leading to electronic interactions which reflect this spatial complexity.

To characterize more completely how vacuum tunneling takes place between the tip and surface, a more complex representation of the tunneling current must be considered. One of the most widely used theories of STM is that of Tersoff and Hamann.[4] Using Bardeen's approximation[5] for the tunneling current between weakly coupled electrodes, Tersoff and Hamann calculated the tunneling current using first-order perturbation theory as:

$$I_t = \left(\frac{2\pi e}{\hbar}\right)\sum_{\mu\nu} f(E_\mu)[1 - f(E_\nu + eV)]\,|M_{\mu\nu}|^2\,\delta(E_\mu - E_\nu) \tag{3}$$

where $M_{\mu\nu}$ is the tunneling matrix element between states ψ_μ of the tip and ψ_ν of the surface, $f(E_\mu)$ and $f(E_\nu)$ are the corresponding Fermi functions, e is the elementary electron charge, V is the applied potential between the tip and the surface, ψ_μ and ψ_ν are nonorthogonal eigenstates of different Hamiltonians, and E_μ is the energy of the state μ, where μ and ν include all states of the tip and surface, respectively. Assuming that the experiments take place at or below room temperature (so no reverse tunneling occurs) and at small voltages (~10 meV for metal-metal tunneling), the limits can be taken under these conditions to yield the following equation:

$$I_t = \left(\frac{2\pi}{\hbar}\right) e^2 V \sum_{\mu\nu} |M_{\mu\nu}|^2 \, \delta(E_\nu - E_F) \; \delta(E_\mu - E_F) \tag{4}$$

where E_F is the Fermi level.

The essential problem now is determining $M_{\mu\nu}$. Bardeen has shown[5] that the tunneling matrix element $M_{\mu\nu}$ can be written such that the wave functions of the tip and electrode only need to be known separately. So,

$$M_{\mu\nu} = \frac{\hbar^2}{2m} \int d\vec{S} \cdot (\psi_\mu^* \vec{\nabla} \psi_\nu - \psi_\nu \vec{\nabla} \psi_\mu^*) \tag{5}$$

where the integral is taken over any surface within the vacuum barrier region separating the tip and electrode. Equations (4) and (5) are, in principle, all that are needed to calculate I_t and hence, the STM image.

Ideally, a direct relation of the STM image to a property of the surface is desired. However, I_t is a complex convolution of the electronic properties of the surface and tip. Tersoff and Hamann were able to model the tip such that the tip properties no longer were a part of the problem. Modeling the tip with a localized potential and wave form, the tunneling conductance, σ (σ is used instead of I_t since at small voltages, σ is independent of voltage), with the limits of low voltage, is

$$\sigma \propto \rho(\vec{r}_t, E_F) \tag{6}$$

where $\vec{r}_t$ is the tip position and

$$\rho(\vec{r}_t, E_F) \equiv \sum_{\nu} |\psi_\nu(\vec{r}_t)|^2 \delta(E_\nu - E) \tag{7}$$

is the surface local density of states (LDOS) at point $\vec{r}$ and energy E. The STM images can now be interpreted as contour plots of the constant Fermi level surface LDOS of the bare surface at the position of the tip. This result is valid for a tip of arbitrary size as long as the tip wave function at E_F can be approximated by an s-wave wave function. Tersoff and Hamann also show that the effective lateral resolution for an STM image is approximately

$$[(2\kappa^{-1})\,(R + d)]^{1/2} \tag{8}$$

where R is the radius of curvature of the tip. Because $2\kappa^{-1} \approx 1.6$ Å^{-1}, the resolution is approximately $[(2\text{ Å})(R + d)]^{1/2}$.

The theory developed by Tersoff and Hamann has provided insights into issues related to the resolution of the microscope,[6] interpretation of STM images,[6-9] and the influence of the tip on imaging.[10,11] Calculations using this theory were compared to the experimental results obtained by Binnig et al[12] for the reconstructed surfaces of Au(110). This surface is known to reconstruct into a (2 x 1) structure with a missing row geometry[13] and, in some instances, into a (3 x 1) structure as well.[14] Binnig imaged the (2 x 1) and the (3 x 1) structures on separate regions of the same surface with the same tip, finding a corrugation of 0.45 Å and 1.4 Å for the (2 x 1) and (3 x 1) surface, respectively. From these results, Binnig concluded that the (3 x 1) surface consisted of two missing rows in the first layer and one missing row in the second layer, which resulted in the large 1.4 Å corrugation compared to 0.45 Å for the (2 x 1) surface.

Tersoff calculated $\rho(\vec{r}, E_F)$, the LDOS at the Fermi-level, for the two reconstructed surfaces found on Au(110) using a linearized augmented-plane-wave (LAPW) method and a tip with a radius $R = 9$ Å. This value was chosen so that the tunneling conductance yields a corrugation of 0.45 Å for the (2 x 1) surface at a tunneling resistance matching Binnig's experimental conditions. The resultant corrugation calculated for the (3 x 1) surface was 1.4 Å, agreeing well with the experimental value.

The above supposition is consistent with experimental data when the surface is of an ordered nature. Unfortunately, many surfaces consist of disordered structures such as terrace steps, kinks, and impurities. Tersoff's computational treatment of these nonperiodic surface structures was based

on the assumption that the calculated $\rho(\vec{r}, E_F)$ for the Au(110) reconstructed surface resembled the total charge density. Using the assumption that the charge can be represented by the superposition of atom charge densities then

$$\rho(\vec{r}, E_F) \propto \rho(\vec{r})/E_o \tag{9}$$

where $\rho(\vec{r})$ is the total charge and $E_o \propto E_F/(\kappa z)$. By using $R = 4$ Å, this value being fitted to yield the corrugation of the (2 x 1) surface as before, agreement was found between the calculated and experimental corrugation for the (3 x 1) surface.

From these calculations, it can be assumed that the atomic corrugations measured in the constant current mode are proportional to the Fermi level LDOS of the bare metal surface. Thus, the image yielded is simply a contour topographic map of the surface. This view, however, is too simplistic. The image is actually a convolution of both geometric and electronic structures of the sample and tip so the nature of the tip must play an important role in the imaging process.

Lang[15,16] considered this in a theory assuming that there was an adsorbed atom at each electrode. In effect, this theory takes into account the total current due to real atoms on the sample and tip, not imposed potential wells. In the exact calculation, the real wave functions of the tip and sample are considered. For his work, a Na atom as the tip was scanned over different surfaces consisting of Na, He, and S atoms. A plot of tip displacement versus lateral separation was then compared to contour plots

of constant Fermi level local density of states and constant total density for each of the three surfaces versus the Na tip. It was found that when Na and He were the surface, the tip-displacement curve agrees quite well with the contour plots of constant Fermi level LDOS and constant total density. In the case of the S surface, tip displacement and constant Fermi level LDOS curves match closely but the curve of constant total density is higher. This is explained by the fact that the almost filled 3p state of the S atom lies close enough to the Fermi level to contribute to the total charge.

These results also revealed how chemically different atoms gave distinctively different tunneling current behaviors. When the tip was scanned over the Na atom versus the S atom, a larger tip displacement was obtained. This can be explained in part because the Fermi level LDOS for S is much smaller than for a Na atom. The He atom imaged as a depression because its closed valence shell is lower than the Fermi energy of the metal which causes the tip to displace negatively. These results show that the chemical nature of the adsorbate on the sample and tip will influence the behavior of the tunneling current as well.

One of the main difficulties in the theory of STM remains its interpretation solely in terms of the unperturbed density of states. The Bardeen approximation ceases to be valid under particular circumstances such as at the energies of surface states, impurity states or other localized states at one of the surfaces, or states associated with the barrier.[17] Also, while the observation of surface states of semiconductors is well established,[18,19] this is not the case for metal surfaces.[20] Atomic resolution

is also found on some compact metal surfaces[21,22] (i.e. Cu and Au) which is not predicted by the LDOS. Intensive theoretical calculations incorporating the strong coupling between the tip and surface have been considered in several studies.[23-31] These more intensive STM theories will not be examined here. Although not complete, the theory of Tersoff and Hamann has increased the knowledge of the STM mechanism and has become a relatively simple approach for the interpretation of STM images.

Applications of STM

The use of STM has spread to many fields including physical and life sciences. It can be used to obtain images from the angstrom scale to microns. Table I contains a list of examples of the use of STM to image semiconductor, metal and organic interfaces in the ultrahigh vacuum (UHV), air and liquid environments.

The observation of atomic resolution of close-packed metal atoms on surfaces was made by Hallmark et al.[22] They were the first to obtain atomic corrugation for a close-packed metal surface, Au(111), in air and UHV. The Au surfaces were prepared by the epitaxial growth of Au onto heated mica substrates (300° C) at 10^{-6} torr. A hexagonal packing arrangement with an atomic spacing of 2.8 ± 0.3 Å was observed, which compares favorably with the expected 2.88 Å interatomic Au spacing.[75] The vertical corrugation was typically ~0.3 Å. This corrugation is much larger than the atomic corrugation for close-packed metals.[76] Electronic enhancements have been observed previously for semiconductor[77] and semimetal surfaces.[78] For the Au

Table I. Survey of Applications of STM

Sample surface	Environment	Reference
Au(111) films at mica	air, UHV and aqueous solution	22, 32-38
Au(111)	aqueous solution	39
Au(111) single crystal	aqueous solution	40
Cu and Au films on Ru(0001)	UHV	41
Cu adlayers at Au(100) and Au(111)	aqueous solution	42
CO on Pt(100)	aqueous solution	43
I on Pt(111)	air and aqueous solution	44, 45
S on Re(0001)	UHV	46, 47
S on Mo(001)	air	48
Pb UPD[a] on Au(111)/mica	aqueous solution	49
Pt films at mica	air	50
Si(111) 7 x 7	UHV	51
NH_3 on Si(111) 7 x 7	UHV	52
Ge on Si(111) 7 x 7	UHV	53
GaAs on Si	UHV	54
InSb(110)	UHV	55
Benzene on Rh(111)	UHV	56
Cu-phthalocyanine on Cu(100)	UHV	57
Naphthalene on Pt(111)	UHV	58, 59
Alkanethiolate self-assembled monolayers at Au(111)	air	60

Polyimide LB monolayers on graphite	air	61
Lipid LB bilayers on graphite	air	62, 63
Alkylcyanobiphenyl (liquid crystals) on graphite	air	64
Polypyrrole on graphite and Au	air	65
Isopolyanion arrays on graphite	air	66
Detergent monolayer on graphite	aqueous solution	67
Glycine on graphite	glycerol/water solution	68
Tosylated β-cyclodextrin on graphite	air	69
DNA	air and water	69-73
Streptavidin adsorbed on biotin-functionalized self-assembled monolayers	air	74

[a]Underpotential deposition.

surface, a surface state near the Fermi level may contribute strongly to the tunneling current. Results from scanning tunneling spectroscopy[79,80] and photoemission studies[81] of Au(111) indicate the continuation of a surface state above the Fermi level, making it possible to tunnel into or out of this state. Further investigation of the Au(111) films on mica by STM has revealed the $(23 \times \sqrt{3})$ reconstruction of the Au(111) surface,[33] a phenomenon previously observed by low-energy electron diffraction,[82] reflection high-energy electron diffraction,[83] and helium atom scattering.[84]

The arrangements of adsorbates on metal surfaces has been the focus of many studies. Schardt et al have investigated the adsorption of iodine on Pt(111) in air[45] and in aqueous solution[44] by STM. Two iodine adlattice unit cells were obtained in air: $(\sqrt{7} \times \sqrt{7})$R19.1° and (3 x 3) with surface coverages of 3/7 and 4/9, respectively. At 3/7 coverage, the position of the I adatoms with respect to the underlying Pt(111) lattice was assigned by varying the tunneling parameters I_t and V. Depending on the tunneling parameters, 1/3, 2/3 or all of the I adatoms in the unit cell could be observed, but exhibit different vertical corrugations. The difference in the vertical corrugation and the spacing of the I adatoms led to the assignment of 1/3 of the I adatoms adsorbed at atop sites, 1/3 at three-fold hollows with a second layer Pt atom below it, and 1/3 at three-fold hollows without a second layer Pt atom below it. At the coverage of 4/9, the (3 x 3) adlattice was observed. Again, not all atoms have equal corrugation and the I atoms were assigned to one atop site and three atoms at two-fold sites in the unit cell.

The in situ investigation on I on Pt was performed in 0.1 M $HClO_4$ under potential control (electrochemical STM). At the rest potential, the $(\sqrt{7} \times \sqrt{7})R19.1°$ adlayer structure was observed, the same as in air. However, at 500 mV below this rest potential, a $(\sqrt{3} \times \sqrt{3})R30°$ adlayer structure was observed, with the registry of the I atoms in three-fold hollow sites. This $(\sqrt{3} \times \sqrt{3})R30°$ structure was never observed in air. Registry of the I adatoms could be determined because the I adlattice was observed typically at 200 mV to 35 mV bias voltages and the Pt substrate at bias voltages less than 35 mV, allowing for subsequent images of the I adlattice and Pt lattice.

The observation of organic species and films by STM has proven to be quite interesting, although difficult. Atomic resolution images of Langmuir-Blodgett (LB) bilayers and self-assembled monomolecular films have been obtained. Smith et al[62] have investigated LB bilayer films of cadmium arachidate on highly ordered pyrolytic graphite (HOPG). They observed a packing arrangement with a triclinic unit cell and spacings in the a and b directions of 5.8 Å and 4 Å, respectively. This structure agrees with data collected from such techniques as infrared spectroscopy, Raman spectroscopy, electron diffraction, x-ray diffraction and fluorescence microscopy. The ability to obtain STM images from such structures is quite remarkable because these bilayers are ~50 Å thick. Smith et al[62] suggest that electrons are transported through the long alkane chains to the conducting surface. However, it seems unlikely that the chains are conductive enough for a tunneling current to flow. Instead, they believe that the electrons must somehow propagate rather than tunnel through the chains. A study of self-

assembled alkanethiolate monolayers at Au surfaces was conducted by Widrig et al[60] and a hexagonal packing arrangement with nearest-neighbor and next-nearest-neighbor spacings of 5 Å and 8.7 Å was observed, spacings consistent with a $(\sqrt{3} \times \sqrt{3})R30°$ adlayer structure on Au(111). Unlike the conclusion for the LB films that the tip was near the monolayer-air interface and electrons were transported through the alkane chains, here it is suspected that the tip is near the surface and tunneling is occurring near or through the Au-sulfur linkage. However, no conclusive data has been obtained to identify the exact position of the tip during scanning of these organic monolayers. The new technique AFM has recently become a very popular tool for these types of systems and the results of these studies will be presented in the following section.

Atomic Force Microscopy

Principles of Operation

The basic principle of force microscopy can be explained using an analog to Hook's Law for the restoring force at a spring. A sharp probe tip mounted on a small spring (cantilever) is tracked across the sample surface. The spring deflects according to the force between the tip and surface, and this deflection is monitored as a function of the lateral displacement of the tip. As with the STM, the interaction of interest in atomic force microscopy (AFM) is between a single atom at the apex of the tip and a single atom on the surface of the sample. Unlike the STM, no current flows between the

sample and the tip in the AFM, allowing nonconducting surfaces to be characterized.

Because AFM essentially uses the displacement of springs to measure forces, a maximum spring deflection for a given force is desired. Thus, springs (cantilevers) with very small force constants are required. However, soft springs are very susceptible to vibration which can severely limit the resolution of the AFM. The sensitivity of the cantilever to vibration in the AFM depends on the lowest resonant frequency, f_o, of the AFM mechanical system. It is desired that f_o of this system be much greater than the frequency of the interfering vibration (e.g. building vibrations, noise, etc.). Rigid mechanical components are needed as well as cantilevers with high resonant frequencies.

The resonant frequency of a spring system is given by

$$f_o = \frac{1}{2\pi}\left(\frac{k}{m_o}\right)^{1/2} \tag{10}$$

where k is the spring constant and m_o is the effective mass that loads the spring. To keep f_o large, it is necessary to keep (k/m_o) large. Thus, to have a softer spring (smaller k) it is necessary to counterbalance by decreasing m_o, so cantilevers with small masses are necessary. With microfabrication techniques, it is possible to make cantilevers with masses less than 0.1 picogram. These low mass cantilevers have resonant frequencies greater than 2 kHz. Thus, force microscopes can have very soft springs and yet be less sensitive to vibration. Typical cantilevers are made of triangular shaped

silicon nitride or bent wires with etched tips and have force constants of 0.1 to 10 N/m.

Force microscopy can be operate in two distinct modes; the contact mode and the noncontact mode. In the contact mode, the mode used most frequently to determine topography, the tip actually touches the sample surface during scanning. Interatomic forces between the apex of the tip and atoms on the surface are recorded. Typical forces measured in this mode are 10^{-6} to 10^{-9} N.[85] By doing measurements in liquid (e.g. water, ethanol), it is possible to further decrease these forces due to decreasing van der Waals forces and elimination of meniscus forces between the tip and sample.[86]

Deflections of the cantilever are used to monitor the force between the tip and sample. Here

$$\text{Force} = k(\Delta z) \tag{11}$$

where Δz is the cantilever displacement from equilibrium in the direction perpendicular to the surface. For topography, the surface is scanned relative to the tip and the sample is moved toward or away from the cantilever tip via a feedback loop to maintain a constant cantilever deflection. These vertical movements are recorded and a topographical map is obtained. Alternately, it is possible to fix the cantilever position as it scans above the surface allowing the cantilever to deflect toward or away from the surface with the variations from the set zero position recorded. The end result of each, a topographical map of the surface, is the same.

In the noncontact mode, the tip is generally 10 to 100 nm from the surface.[87] It is possible to measure long-range forces, such as electrostatic, magnetic and van der Waals forces.[88] A different type of force detection other than static cantilever deflection is used in this case. Here, the cantilever is driven to vibrate near its resonant frequency by a small piezoelectric element. The presence of a force gradient changes the spring constant of the cantilever. If k_0 is the spring constant of the isolated cantilever, then

$$k = k_0 + (\delta F_z/\delta z) \tag{12}$$

with $(\delta F_z/\delta z)$ being the gradient of the force in the z direction. If the sample exerts an attractive force on the cantilever ($(\delta F_z/\delta z)$ is negative) then k will decrease and the spring will essentially soften.

Because k changes in the presence of the force, the resonant frequency also changes (recall Equation (10)) and this change in resonant frequency is detected by measuring the amplitude phase or frequency change of the vibration. An interferometry optical detector[89] is typically used. Two of the most often used noncontact techniques are magnetic and electrostatic force microscopies.

Types of Forces

When two bodies come into close proximity there are numerous interactions arising between them, depending on the nature of the two

bodies. Some interactions, such as van der Waals forces, are always present and are detectable over hundreds of angstroms. Other interactions occur only if the surfaces are not more than a few angstroms apart.

The van der Waals and contact repulsion forces in general reveal the topography of the sample. Other forces, such as magnetic and electrostatic, lead to an additional attraction or repulsion, while adhesion and binding forces play a role in friction and can lead to an atomic scale "stick-and-slip" behavior of the tip. Van der Waals interactions are always present between the tip and the surface. These include induction forces (interaction of a dipole with an induced dipole), orientation forces (interaction between two oriented permanent dipoles) and dispersion forces (induced dipole-induced dipole interaction and are quantum mechanical in origin). They are long range (2 Å to > 100 Å) and can be attractive or repulsive.[90] Adhesion, surface tension, and physisorption are macroscopic phenomena which are a result of van der Waals interactions.

Ionic repulsion occurs when the tip and surface come closer together than a few angstroms (i.e. at high contact forces) and the electron clouds of their respective ions start to overlap, giving rise to a rapidly increasing repulsive force. This is the reason for the repulsive part of the Lennard-Jones[90] potential, which approximately describes the total intermolecular pair interaction. Most of the topographic imaging work by force microscopy is done in this high contact force regime.

Theory

A description of the forces at a given surface and their influence on a probe tip is quite complex. Recently, a theoretical description of scanning force microscopy has appeared for scanning in the contact force regime.[91] The geometry of the cantilever and sample positions is shown in Figure 2. The position of the tip and piezo-tube are denoted z and u respectively. The distance between the tip and sample is s, and $g(x,y)$ is the sample surface corrugation. Forces which are dependent on the tip-sample gap can include atomic or molecular forces (i.e. van der Waals and ionic repulsion forces) ($F_1(x,s)$), electrostatic forces ($F_2(x,s)$), or magnetostatic forces ($F_3(x,s)$). If the tip is scanned only in the x direction, then the total tip-sample force equals the restoring force (Equation (11)) of the cantilever

$$\sum_{i=1}^{3} F_i(x,s) = k[u - (z - z_0)] \tag{13}$$

where the summation is on the three forces, z_0 is the cantilever position with no forces acting on it, and $(z-z_0)$ is the displacement of the cantilever from equilibrium. Expressing Equation (13) in differential form yields

$$\sum_{i=1}^{3} \left(\frac{\partial F_i(x,s)}{\partial s} ds + \frac{\partial F_i(x,s)}{\partial x} dx \right) = k(du - dz). \tag{14}$$

In the case of scanning in the constant force mode (where the cantilever retains a constant deflection) the right half of Equation (14) is zero (since

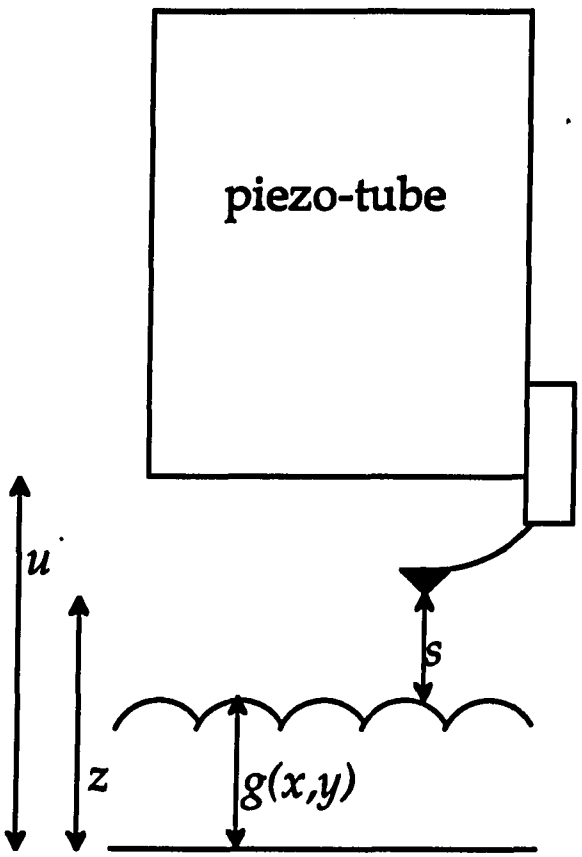

Figure 2. A schematic of the cantilever and sample positions in an AFM. The surface corrugation is represented by $g(x,y)$ and z and u are the positions of the tip and piezo-tube, respectively. The distance, s, is that between the tip and sample surface.

$du=dz$), yielding

$$\sum_{i=1}^{3}\left(\frac{\partial F_i(x,s)}{\partial s}ds+\frac{\partial F_i(x,s)}{\partial x}dx\right)=0. \tag{15}$$

Since $dz = ds + dg(x)$ and $du = dz$, then $ds = du - dg(x)$. Substituting for ds in Equation (15) gives

$$du = dg(x) - \alpha\sum_{i=1}^{3}\left(\frac{\partial F_i(x,s)}{\partial x}dx\right) \tag{16}$$

where α is an amplification factor and

$$\alpha=\sum_{i=1}^{3}\left(\frac{\partial F_i(x,s)}{\partial s}ds\right)^{-1}. \tag{17}$$

Thus, the piezo-tube will follow the topography of the sample surface, $g(x)$, for forces which are constant on the surface (independent of x, as is the case when the sample has the same atoms all across the surface). Also, when the feedback maintains the lever at a fixed deflection, as is the case for the above derivation, the response of the piezo-tube is independent of the cantilever force constant. Amplification of the resulting AFM image can occur. The amplification (α) of the image depends on tip-sample gap and interaction forces. If the force acting on the tip is small (as when the tip is far from the surface), then the laterally dependent forces, $\partial F_i/\partial x$, will be amplified.

The strength of adhesion forces between the probe tip and the sample surface has been the focus of several investigations.[86,92-94] Calculations suggest that the force between the tip and sample should not exceed 10^{-11} N for biological surfaces[95] and 10^{-9} N for "hard" surfaces.[96] Another calculation has actually determined that at 5×10^{-8} N an AFM tip can actually "puncture" the surface of graphite.[97] Thus, measurement and minimization of forces when scanning a surface with a force probe is very important.

Weisenhorn et al[86] measured the absolute force between a tip and a mica surface. The force was measured by first bringing the tip and sample into close proximity. When approached to the sample, the cantilever suddenly jumps into contact with the surface. On retraction, the cantilever has to be pulled a large distance away from the surface until it snaps back, breaking all contact with the surface. This phenomenon is well known form various force measurement techniques. When the gradient of the measured force becomes larger than the force constant of the force probing system, the situation becomes unstable and the cantilever jumps into a stable position. From this process, a force versus distance curve can be obtained. An example of such a curve is shown in Figure 3. In region A, the tip and surface are in contact and the tip adheres to the surface as the two are pulled apart. At point B, the force between the tip and the surface is no longer sufficient to allow continued contact and the cantilever snaps back to its equilibrium position. In the region C, the cantilever does not sense any forces from the surface. The sample and tip are again approaching each other in region D and not until region E does the tip again sense the interaction forces of the

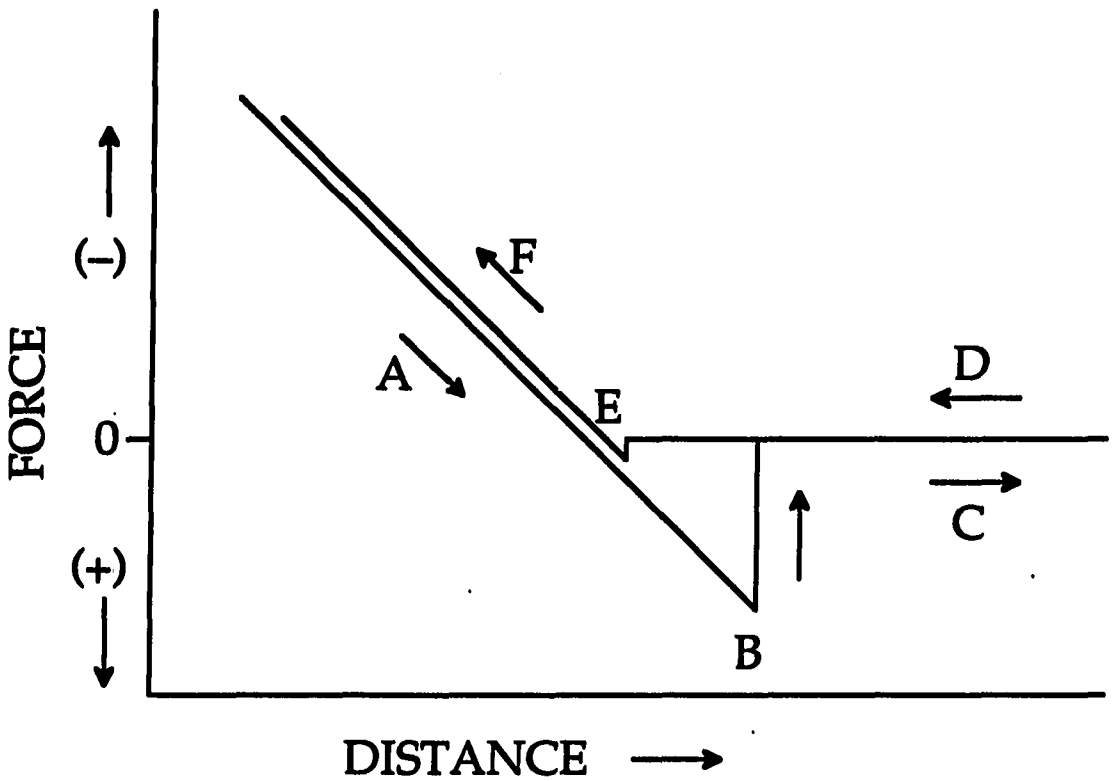

Figure 3. An example of a force versus distance curve. The y-axis is force, with negative (–) being repulsive and (+) being attractive. The distance is that which the piezo-tube is moving, bringing the tip and sample closer (to the left) and further (to the right) from each other. The arrows indicate the direction of the scan cycle. Regions A-F are described in the text.

surface and it then jumps into contact with the surface. This region can be used to measure the attractive forces between the tip and sample surface. The tip and sample are again in contact in region F. By measuring the deflection at which the contact between the tip and sample is broken (point B) the adhesive force can be determined. This is the approach used by Weisenhorn et al[86] to measure the forces between a silicon nitride pyramidal tip, with a cantilever force constant of 3 N/m, and a mica surface. A force of ~4 x 10^{-7} N was measured in air and <5 x 10^{-9} N in water. The large difference in the measured forces in air versus water is due to the decrease in the van der Waals forces (by about an order of magnitude) and the elimination of attractive surface tension (meniscus) forces in liquid.

Burnham et al[93] performed a similar study using a tungsten tip and a series of substrates coated with Langmuir-Blodgett (LB) monolayer films. They found that as the surface energy of the sample increased, the measured forces systematically increased. An Al_2O_3 surface coated with an alkanoic acid LB film, which has a lower surface energy (21 mJ/m^2) than does the bare Al_2O_3 substrate (45 mJ/m^2), also has a lower adhesive force (by ~65 nN). When the monolayer is prepared such that the functional group exposed to the tip is changed from -CH_3 to -CF_3, the surface energy decreases to 20 mJ/m^2 yet the adhesive force decreases by 15 nN. This study indicates the great sensitivity of the AFM to changes in the surface being characterized.

Applications of AFM

The greatest efforts in force microscopy so far have been put into its application as an imaging device. With AFM it has become possible to get atomic resolution images of nonconducting samples. The first atomic resolution image of a nonconductor was that of boron nitride.[98] As a result of this capability, the use of AFM for organic surfaces, especially biological surfaces, has become popular.

Table II includes a listing of some of the applications of AFM from metal surfaces, to biological surfaces, to in situ electrochemical processes. Particularly interesting are those involving atomic or molecular resolution of organic interfaces as well as the in situ investigation of electrochemical and adsorption processes. Some examples will be described in detail.

The use of AFM to obtain molecular resolution images of Langmuir-Blodgett (LB) films is demonstrated by Weisenhorn et al.[104] Four different lipids were used to create LB films with different surface charges (i.e. cationic, anionic, and zwitterionic). These films were deposited on cadmium arachidate or octadecyltrichlorosilane coated mica. For the film of L-α-dipalmitoyl-phosphatidylglycerol on cadmium arachidate coated mica, they observed a molecular arrangement similar to that obtained from the 3D crystal data. This information was obtained at ~10 nN. When the force between the tip and surface was increased to ~100 nN, a hexagonal structure with a lattice spacing consistent with that of mica was observed. Thus, these films, which are not covalently linked to the mica surface, were destroyed by the high applied force. When a covalently linked monolayer

Table II. A Survey of Applications of AFM

Sample surface	Environment	Reference
Au(111) films on mica	air and water	99
Bi films on mica	air and aqueous solution	100
Bi UPD[a] on Au(111)	aqueous solution	101
Ag UPD on Au(111)	aqueous solution	102
Cu UPD on Au(111)	aqueous solution	103
Langmuir-Blodgett films	air and aqueous solution	104-106
Polymeric films	air and aqueous solution	107-109
Alkanethiolate monolayers at Au(111)	air	110
Lipid-protein membranes	aqueous solution	111
Polyanaline on glass	air and aqueous solution	112
DNA	air and aqueous solution	104,113,114
Red blood cells	air	115
Immunoglobulin adsorption dynamics	aqueous solution	116
Photodimerization of cinnamic acid and anthracene	air	117,118

[a]Underpotential deposition

(octadecyltrichlorosilane) coated the mica, the increased force caused distortion and eventual disappearance of the molecularly-resolved image, but the mica structure was not observed. Also, when the force was then reduced, molecular resolution of the layer was again obtained. Molecules of single-stranded DNA were adsorbed on top of the charged surfaces of the LB films and images were obtained by AFM under buffer solution in hopes of sequencing the DNA. Unfortunately, the electrostatic attraction between the DNA and LB film was not strong enough to prevent the DNA from moving and thus, no reproducible scans were obtained, so sequencing was not possible. This study emphasizes the need for strong linkages of the molecules to the underlying substrates in order to withstand the force of the scanning probe.

The AFM can also be used to obtain information about dynamic processes. Lin et al[116] studied the adsorption dynamics of immunoglobulin on mica in a buffer solution. After obtaining an image of the underlying substrate in aqueous solution, the immunoglobulin was injected into the AFM cell and small raised patches appeared on the surface. After about five minutes, ridges began to appear which gradually began to grow and finally encompassed the entire surface. During this process, the molecules which adsorbed near the ridges stayed on the surface, yet those which adsorbed as isolated patches desorbed from the surface. Apparently only those molecules with sufficient lateral interaction had the capability to remain on the surface. Although it is certain that the scanning probe is pushing the molecules on the surface, the extent to which this occurs is not known. Thus, it is possible

to obtain information of dynamic processes using AFM. With the advent of cantilever technology, it may soon be possible to study these processes with little or no influence from the scanning probe.

The AFM has also been useful in the in situ characterization of electrochemical processes at electrode surfaces. Gewirth and co-workers have been studying the underpotential deposition (UPD) of Cu[103] and Ag[102] at Au(111). For Cu at Au(111), the UPD monolayer of Cu was observed to have a different structure depending on the electrolyte. In perchloric acid, a closest-packed structure of Cu atoms was observed, with the nearest-neighbor spacing of 0.29 ± 0.02 nm. However, when sulfuric acid is used, the Cu atoms are not closest-packed and the spacing between neighboring atoms is 0.49 ± 0.02 nm. In both cases, as the Cu overlayer grew, the Cu atoms converged to a (111)-oriented layer with a lattice spacing of 0.26 ± 0.02 nm. Registry of the Cu lattice with respect to the underlying Au(111) lattice was determined from an image in which the Cu monolayer was being removed. Half of the image exhibits the characteristic spacing and corrugation of Au(111) and the other half that of Cu, with a step between the two halves of 0.18 ± 0.05 nm, indicating the presence of only one monolayer of Cu. This image shows that the Cu lattice is rotated 30° with respect to the Au(111) lattice. As with the Cu UPD at Au(111), Ag UPD at Au(111) also shows electrolyte dependent structures. A 3 x 3 Ag overlayer structure was observed in sulfuric acid, a 4 x 4 overlayer structure in nitrate- and carbonate-containing electrolytes, a more complex structure, which is not closest-packed, in perchloric acid and a closest-packed overlayer in acetate. In general, this difference in packing of

metal atoms is attributed to the size of the electrolyte. In electrolytes which can complex with Ag, the packing structures of the Ag atoms are more open, with the larger electrolytes yielding more open structures due to coadsorption. The coverage determined by AFM (based on the structures observed) and the coverage from coulometric data do not agree. Thus, further investigation of the system is needed. However, this study clearly identifies the capability of AFM to obtain real-time images under potential control.

Conclusion

The scanning tunneling (STM) and the atomic force microscopies (AFM) have opened a new world to scientists, one in which the observation of atoms and molecules has become almost commonplace. The ability of these techniques to provide fundamental physical and chemical information about surfaces has made it possible for scientists to actually observe atomic and molecular surface structure as well as to study the reactivity of these surfaces at the atomic and molecular level. The number of applications of these techniques grows larger everyday; from manipulating atoms with the STM, to sequencing DNA with the AFM. The popularity of these techniques with physical and life scientists, as well as engineers, assures that these techniques will continue to develop and their applications become limitless.

PAPER 1. SCANNING TUNNELING MICROSCOPY OF ETHANETHIOLATE AND *n*-OCTADECANETHIOLATE MONOLAYERS SPONTANEOUSLY ADSORBED AT GOLD SURFACES

ABSTRACT

Monolayer films from ethanethiol (ET) and *n*-octadecanethiol (OT) spontaneously adsorbed onto epitaxially grown Au(111) films on mica were examined by scanning tunneling microscopy (STM). The resulting atomically resolved images are the first reported for gold-adsorbed organothiolate molecules and reveal the packing arrangement of the overlayer. Tunneling is presumed to occur between the microscope tip and the gold-bound sulfur of the *n*-alkanethiolate head-group. For both the ET and OT monolayers, an image that corresponds to a hexagonally packed array of adsorbates with respective nearest-neighbor and next-nearest-neighbor spacings of 0.50 ± 0.02 and 0.87 ± 0.04 nm was observed. This packing agrees well with the $(\sqrt{3} \times \sqrt{3})R30°$ structure determined for long-chain *n*-alkanethiolate monolayers on Au(1$\bar{1}$1) in recent helium diffraction[1] and electron diffraction[2] studies. Furthermore, images with the above spacings were found to exhibit continuity over areas from a few nm^2 up to about 600 nm^2, indicating the potential utility of STM for probing both the short- and long-range order of organic monolayer films. Structural interpretations of these images are presented and examined within the context of molecular level descriptions that have been recently developed from macroscopic characterization studies of these monolayers.

INTRODUCTION

Spontaneously adsorbed monolayer films of *n*-alkanethiolates[3] and their functionalized analogs have been extensively examined as model molecular systems for elucidating structure-reactivity relationships at metal-liquid interfaces.[1, 2, 4-6] As a result of such efforts, details concerning the macroscopic (average) structure, electronic properties, surface free energy, and imperfections of these layers are beginning to emerge. To utilize these results fully, however, it is also necessary to possess a microscopic understanding of the monolayer structure, including descriptions of the short- and long-range packing arrangement within the film. The relatively new technique of Scanning Tunneling Microscopy (STM) provides the real-space atomic resolution required to obtain such information[7] at both organic[8] and inorganic[9] adsorbate layers. In this report, we show that the application of STM to ethanethiolate- (ET) and *n*-octadecanethiolate- (OT) coated gold surfaces reveals the two-dimensional structure of the adsorbate.

In the following sections, we present and discuss the first STM images obtained for ET and OT monolayers spontaneously adsorbed on epitaxially grown Au(111) films. As discussed, we believe our images result from electrons tunneling between the microscope tip and the sample surface through the gold-bound sulfur of the *n*-alkanethiolate head group. For both ET and OT, an image that corresponds to a hexagonally packed adsorbate overlayer with respective nearest-neighbor and next-nearest-neighbor spacings of 0.50 (± 0.02) and 0.87 (± 0.04) nm was observed. The two-

dimensional arrangement suggests that the surface is covered predominantly with a $(\sqrt{3} \times \sqrt{3})R30°$ overlayer on an underlying Au(111) lattice. This arrangement agrees with that reported by helium[1] and transmission electron[2] diffraction studies. In addition, images with the above spacings were found to exhibit continuity over areas of a few nm^2 up to about 600 nm^2. Such images suggest that STM can provide important evidence regarding the size and distribution of ordered domains within these monolayers. A structural interpretation of the images is presented and examined in the context of the molecular level descriptions that have been developed from recent studies with various macroscopic characterization techniques.[1,2,4]

EXPERIMENTAL

Monolayer Preparation.

Gold substrates with a predominant (111) texture were prepared by the epitaxial growth of 200 nm gold films onto freshly cleaved mica sheets.[10, 11] The mica sheets were nominally 1 inch by 1/2 inch. The deposition was carried out by resistive evaporation in a cryogenically pumped Edwards 306A vacuum chamber (West Sussex, England) at a pressure of ~2 x 10^{-6} torr. Immediately prior to deposition, the mica was heated in vacuum at 200° to 300° C for ~1 hour. Gold was deposited onto the heated mica at a rate of 0.3 nm to 0.7 nm per second. Subsequently, the substrates were allowed to cool radiatively to below 70° C, removed from the vacuum chamber, and immersed immediately in 1 mM ethanolic solutions of ET or OT to form the monolayers.[4b] The substrates were left in solution for 2 to 24 hours, emersed, and rinsed thoroughly with ethanol. Variation of the immersion time did not observably effect the resulting images. These monolayers are structurally comparable to those prepared at Au films deposited at polished silicon wafers, as determined by infrared reflection spectroscopic, contact angle, and electrochemical capacitance measurements.[3] The ET was used as received (Aldrich); OT (Aldrich) was recrystallized twice from methanol.

Instrumentation.

All images were acquired with a Digital Instruments Nanoscope II STM (Santa Barbara, CA). The instrument was equipped with a 450 nm x 450

nm scanning head and was operated in the laboratory ambient. With this instrument, the images are displayed as though the tip moves from right to left across the computer monitor; the figures in this report maintain this presentation.

Images examining large (0.02 to 0.20 μm^2) sections of the sample were recorded under conditions for constant current (the "height" mode of the Nanoscope II). In this mode, a preselected tunneling current between the tip and sample is maintained via a feedback loop to a piezoelectric tube that adjusts the vertical position of the tip. The adjustments to maintain a constant tunneling current are recorded as the tip is rastered over the sample surface. Typical tunneling currents and bias voltages used for these images were 3 nA and +80 mV, respectively, with the sign of the bias voltage given with respect to the grounded substrate. The tips used for these large scans were fabricated from 0.010 inch diameter tungsten wire cut diagonally with wire cutters.

For atomically resolved images, conditions for constant height imaging were found more useful (the "current" mode of the Nanoscope II). In this mode, the vertical position of the tip is held constant with variations in the tunneling current recorded as the tip moves across the sample surface. Images were obtained under a range of bias voltages (-200 to +200 mV) and tunneling currents (1 to 10 nA). The tips used for the atomically resolved images were fabricated by etching electrolytically a 0.010 inch diameter tungsten wire in a solution of 1M KOH.[12] Only those tips which readily provided well defined images of highly ordered pyrolytic graphite (HOPG)

were used. The lateral distances in these images were determined using HOPG for calibration.

RESULTS AND DISCUSSION

To develop a basis for the discussion of our results, we first describe the various control experiments performed to verify that our STM images result from the presence of the monolayer. We next present images for our uncoated Au films, which reveal both the topography and predominate (111) crystallinity of the surface. The latter images serve as a reference for the presentation and discussion of the images of the spontaneously adsorbed monolayers of ET and OT. We conclude with a structural assessment of these images in the context of molecular level descriptions that have been developed from various macroscopic characterization techniques, and a brief discussion of a possible mechanism that gives rise to these images.

Reproducibility of Imaging *n*-Alkanethiolates on Au with STM.

To date, the tunneling conditions which consistently allow the observation of a well defined image have been difficult to define fully. We attribute this primarily to preparative variability of the shape and/or composition of the tip. "Good" and "bad" tips were distinguished solely on the basis of their ability or inability to resolve atomic structure at HOPG. Once constructed, a good tip was often used repeatedly. Also, images recorded upon initial engagement of a good tip at the sample surface frequently show no evidence of recognizable surface structure; it is only with time, displacement of the tip, and/or variation of the tunneling conditions that periodic features at an atomic level become apparent. It is usual that

once a structure is observed, successive scans over the same area reproduce the image for several minutes up to an hour, after which time the image gradually or suddenly disappears. Moderate variation in the tunneling current (0.5 to 10 nA) and bias voltage (±20 to ± 300 mV) during the time that the image is "in focus" usually does not lead to loss of the image. Instabilities in the tip shape or composition may cause this focusing and loss of atomically resolved images.[8n,9e,11]

Because of the above difficulties, we cannot directly conclude that our images are representative of the structure across the entire surface of the sample. Such an extrapolation is also complicated because the actual surface area examined is very small (~10^{-13}-10^{-12} cm^2). We are confident, however, that the images described below result from the presence of the monolayer and extend in some cases over areas as large as 600 nm^2. Several control experiments support our contention.[13] First, each of the images reported has been observed on several (≥20) samples of each adsorbate. Second, we have yet to observe images comparable to those of the thiol adsorbate at our uncoated Au or at uncoated Au exposed to neat ethanol. Third, preliminary experiments with monolayers containing long perfluorocarbon chains (e.g. $CF_3(CF_2)_7(CH_2)_2SH$) yield images with a larger nearest-neighbor separation than found for the ET and OT layers. The latter observation is consistent with the packing limitations of the ~5.6 Å diameter of perfluoromethylene chains[2b] as opposed to that of the ~4.2 Å diameter of methylene chains.[14] Together, these results indicate that our images result from the presence of the sulfur-bound alkanethiolate.

STM Characterization of Uncoated Au Films on Mica.

Figure 1 is a STM image of a 450 nm x 450 nm section of a thin gold film that was epitaxially deposited onto freshly cleaved mica. This image was recorded using the constant current mode. This and all other images shown are grey-scale images in which the lighter areas correspond to higher regions of the surface and the darker areas to lower regions of the surface. The color scale for the height range of each figure is shown to the right of the image. As previously observed,[10,11] the image in Figure 1 shows the gold film to be comprised of atomically flat crystallites that are a few hundred nanometers in diameter and are separated by grain boundaries of varied width. Profiles of the grain boundaries are difficult to assess because of possible tunneling between the side of the tip and the sides of the crystallites. The image shown was recorded immediately after removal of the sample from the evaporator, though continued storage of the bare substrate in the laboratory ambient does not effect the images at a noticable level.

An atomically resolved 2.3 nm x 2.3 nm image of an uncoated gold substrate is shown in Figure 2A. Hexagonal arrays of bright spots are evident throughout the image. This is the only periodic feature on our uncoated Au substrates that we have observed to date, having examined more than 30 samples. Figure 2B is a topographical contour plot taken along the black line overlaying the image in Figure 2A. The distance between the markers in Figure 2B gives a nearest-neighbor spacing of 0.29 ± 0.02 nm, which compares well with the 0.288 nm interatomic separation of Au atoms[11] of a (111) surface. Larger area scans show that the spacing exists for lateral tip

Figure 1. STM image of a 450 x 450 nm section of an uncoated epitaxially grown Au film on mica. The image was recorded in the constant current mode, without filtering, using a bias voltage of +80 mV and a tunneling current of 3 nA.

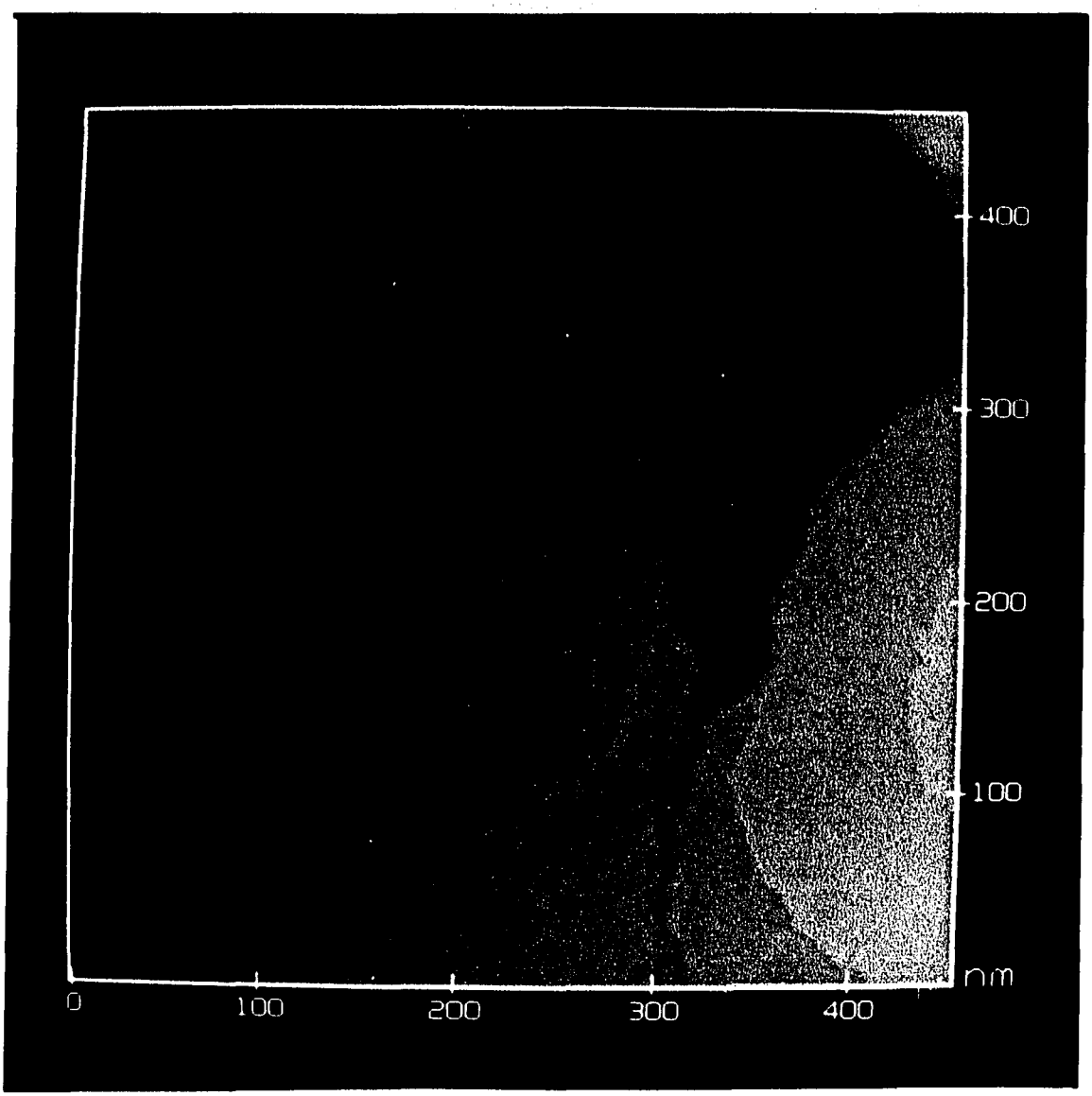
400
300
200
100
nm
0
100
200
300
400

Figure 2. (A). An atomically resolved 2.3 x 2.3 nm section of an epitaxially deposited Au on mica film. The image was recorded in the constant height mode using a bias voltage of 100 mV and a tunneling current of 1.5 nA. This image was low-pass filtered.

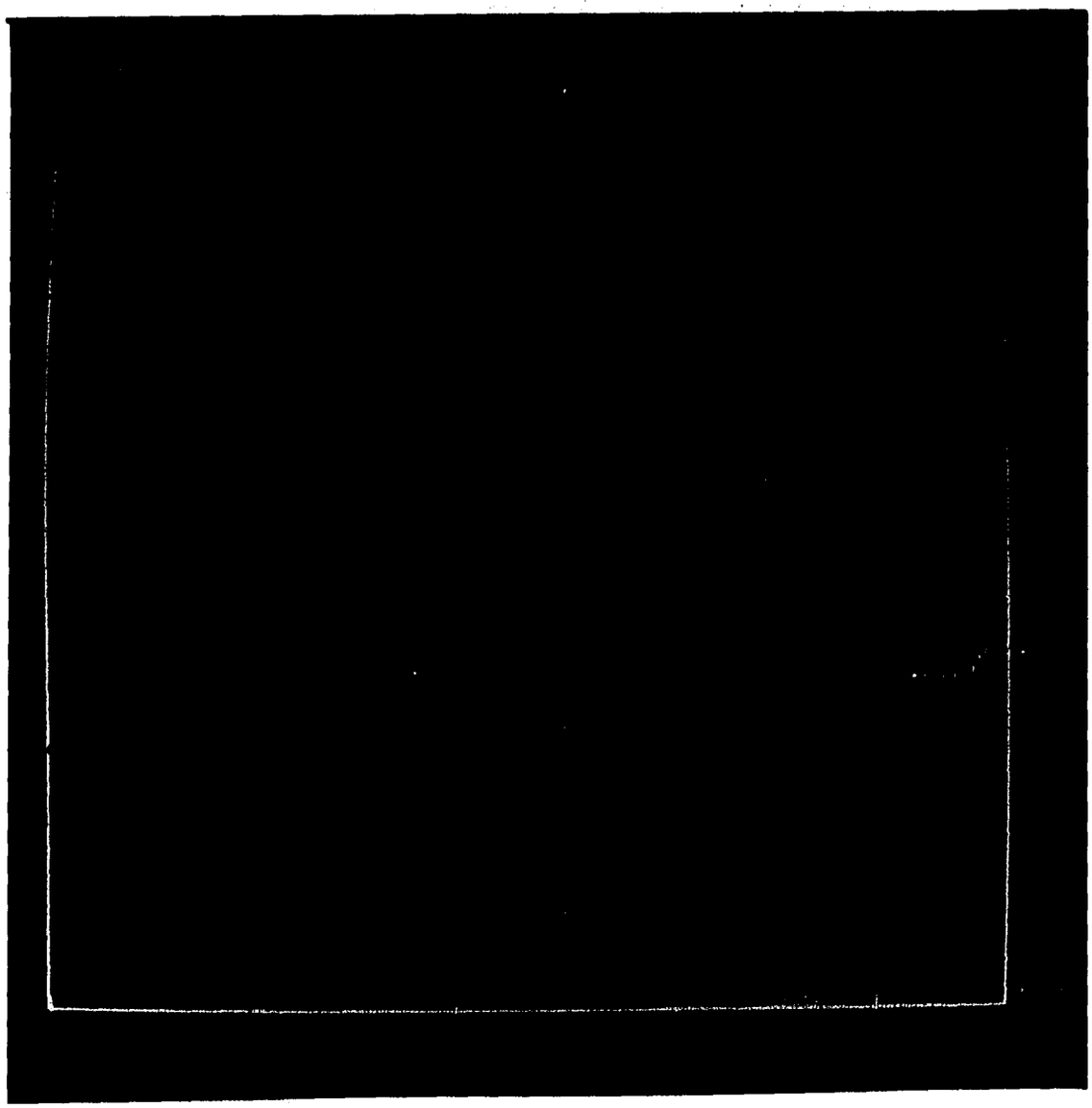

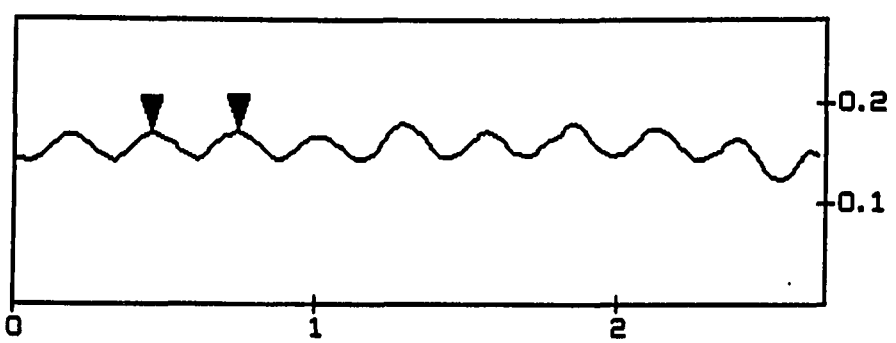

Figure 2 (cont'd). (B). A contour of the surface for the black line that is superimposed on the image in Figure 2A. The markers on the contour indicate a nearest-neighbor spacing of 0.29 nm.

translations of tens of nanometers. In examining the figures, it is important to note that the vertical corrugation along the contour is a manifestation of the density of states in the electronic band structure at the surface, as opposed to an actual topographical distance.[11]

The predominance of the (111) character of our Au films is consistent with that indicated by the current-potential curves for the underpotential deposition of Pb(II) by linear sweep voltammetry.[3, 15] Earlier studies with both low energy electron diffraction[11] and x-ray diffraction[10] support our conclusion. Based on these results, we will refer to our Au substrates simply as Au(111).

STM Images of Ethanethiolate Monolayers on Au(111).

All of the images presented in this section were obtained using constant height imaging. Also, as noted in the figure captions, several of the images have been smoothed with an eight-point moving average algorithm, i.e. the low-pass filter utility of the Nanoscope II software. The remaining images are not smoothed.

Figure 3 shows STM images found for a spontaneously adsorbed monolayer of ET at Au(111). Figure 3A is an image slightly less than 8 nm x 8 nm. Figure 3B is an expanded view of the middle right portion of Figure 3A, and is slightly greater than 2.5 nm x 2.5 nm. In both images, a hexagonal pattern with a spacing markedly different from that of the Au(111) lattice is evident. The spacings of this pattern are given by contour plots in Figure 3C, which are taken along the dark lines overlaying the image of

Figure 3. (A) STM image of a 7.7 nm x 7.7 nm section of an ethanethiolate monolayer on an epitaxially grown Au film on mica. Figure 3A is unfiltered and recorded in a constant height mode using a bias voltage and tunneling current of -200 mV and 2 nA, respectively.

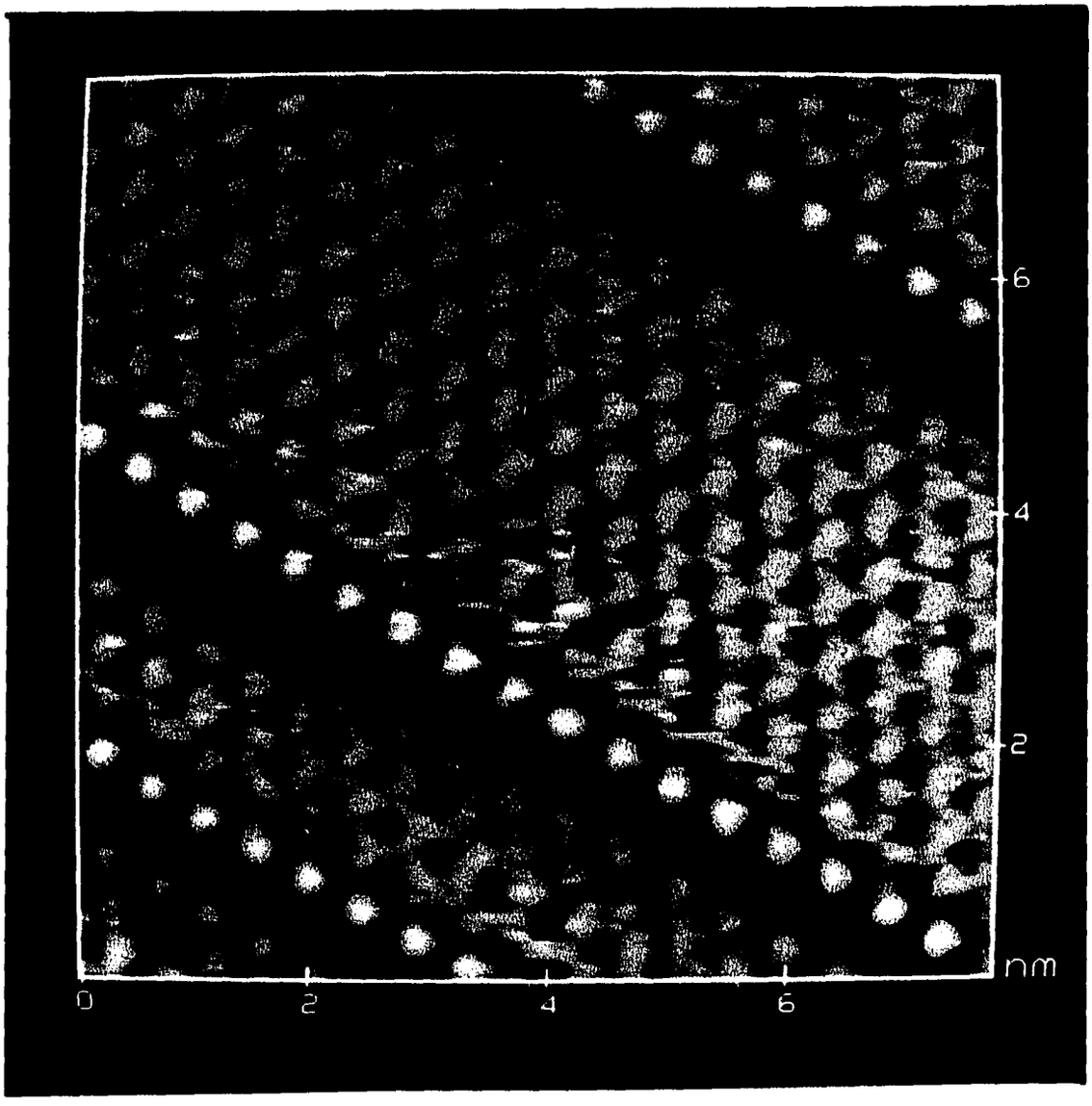
6
4
2
nm
0
2
4
6

Figure 3 (cont'd). (B) STM image of a 2.65 nm x 2.65 nm section of an ethanethiolate monolayer on an epitaxially grown Au film on mica imaged under the same conditions as Figure 3A.

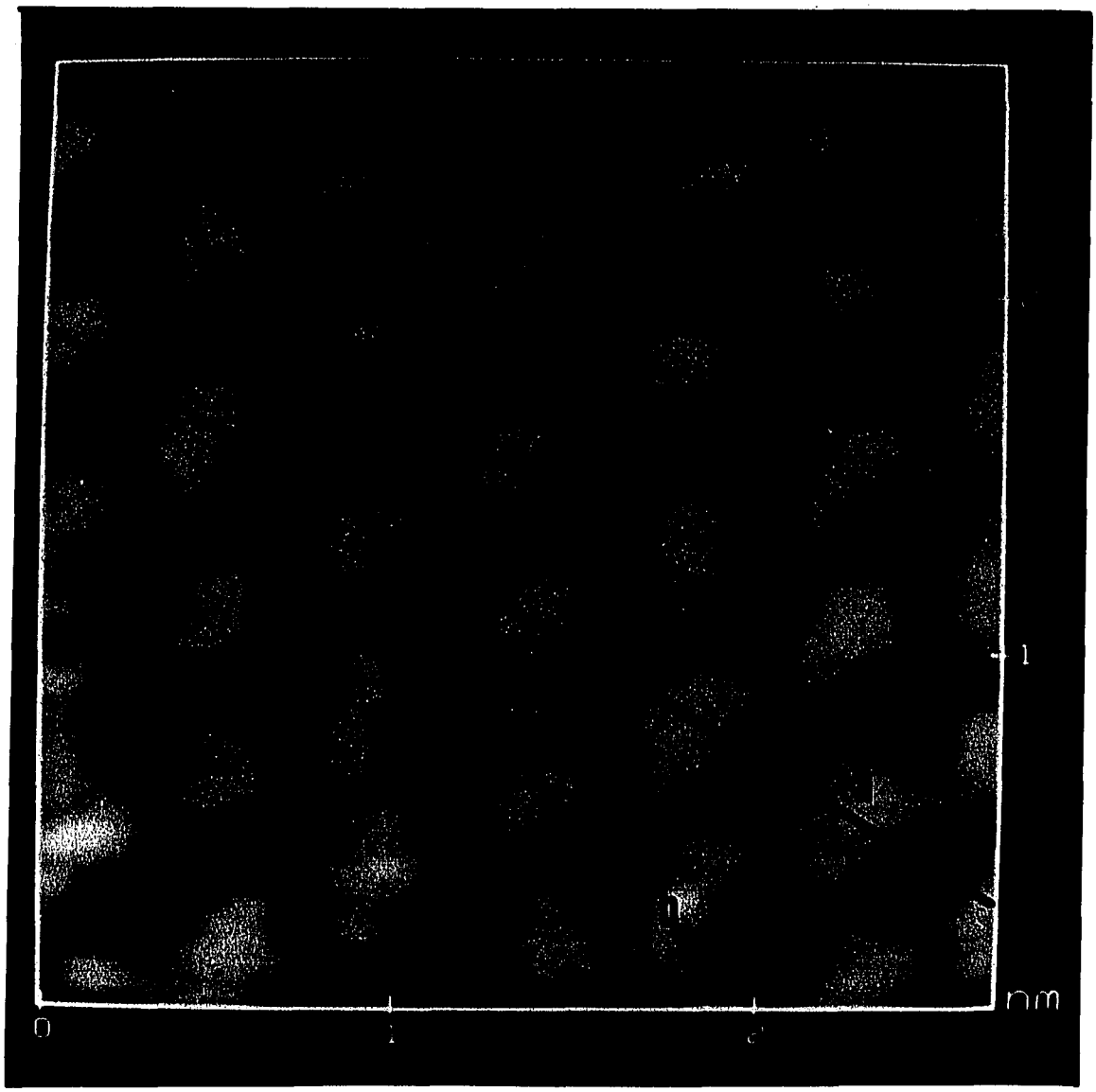
1
nm
0

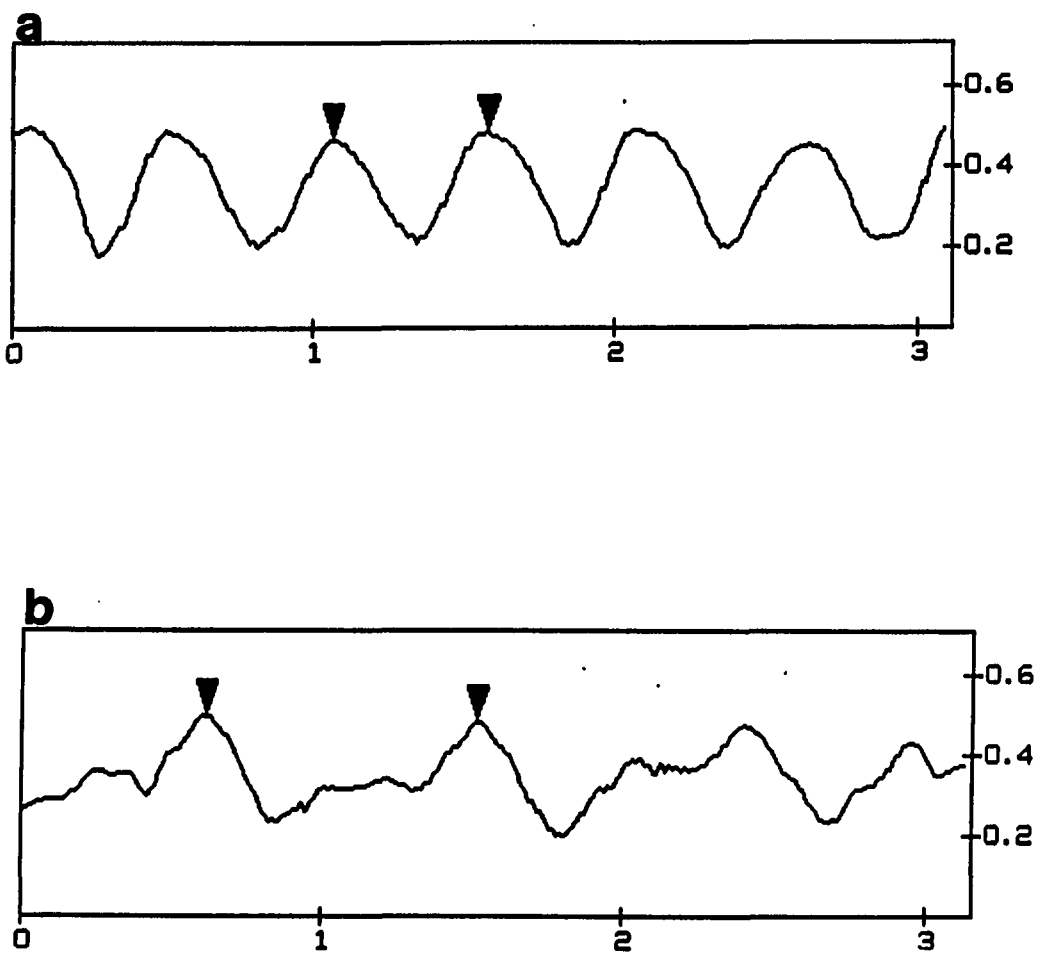

Figure 3 (cont'd). (C) Contours of the image along the lines (a) and (b) in Figure 3B. The markers in the upper contour indicate the nearest-neighbor spacing of 0.51 ± 0.02 along line (a). The markers in the lower contour indicate the next-nearest-neighbor spacing of 0.91 ± 0.04 nm along line (b).

Figure 3B. The triangular markers in the upper and lower contours of Figure 3C indicate respective nearest-neighbor and next-nearest-neighbor spacings of 0.51 (± 0.02) and 0.91 (± 0.04) nm. The uncertainties in the spacings are consistent for all of our ET samples. The average nearest-neighbor and next-nearest-neighbor spacings from more than 20 samples is 0.50 (± 0.02) and 0.87 (±0.04), respectively, which are consistent with a $(\sqrt{3} \times \sqrt{3})R30°$ adsorbate layer on a Au(111) surface. Such a two-dimensional arrangement has also been found for long-chain *n*-alkanethiols adsorbed at Au(111) via helium[1] and electron[2] diffraction studies. Additionally, the spacings in the images are comparable to those found at our OT-coated samples (*vida infra*) as well as to those found in a few preliminary scans of monolayers from *n*-decanethiol.

For comparison to the image in Figure 3B, Figure 4 provides a scale drawing of a Au(111) surface (open circles) with a commensurate overlayer of adsorbate molecules (shaded circles) representing an *n*-alkanethiolate monolayer. The packing of the overlayer was determined by assuming that each adsorbate molecule binds at an equivalent site. The 0.42 nm diameter of the overlayer structure equals that for a closest-packed array[14] of alkyl chains. Although our images do not provide information concerning registry with the underlying substrate, we have placed the adsorbates in equivalent three-fold hollow sites as previously suggested.[2,9b] An identical overlayer structure may be drawn with *n*-alkanethiolate molecules centered at either on-top or two-fold bridging sites. In all three cases, the respective nearest- and next-nearest-neighbor spacings of the overlayer structure are 0.498 nm and 0.864 nm, which agree with those of Figure 3B.

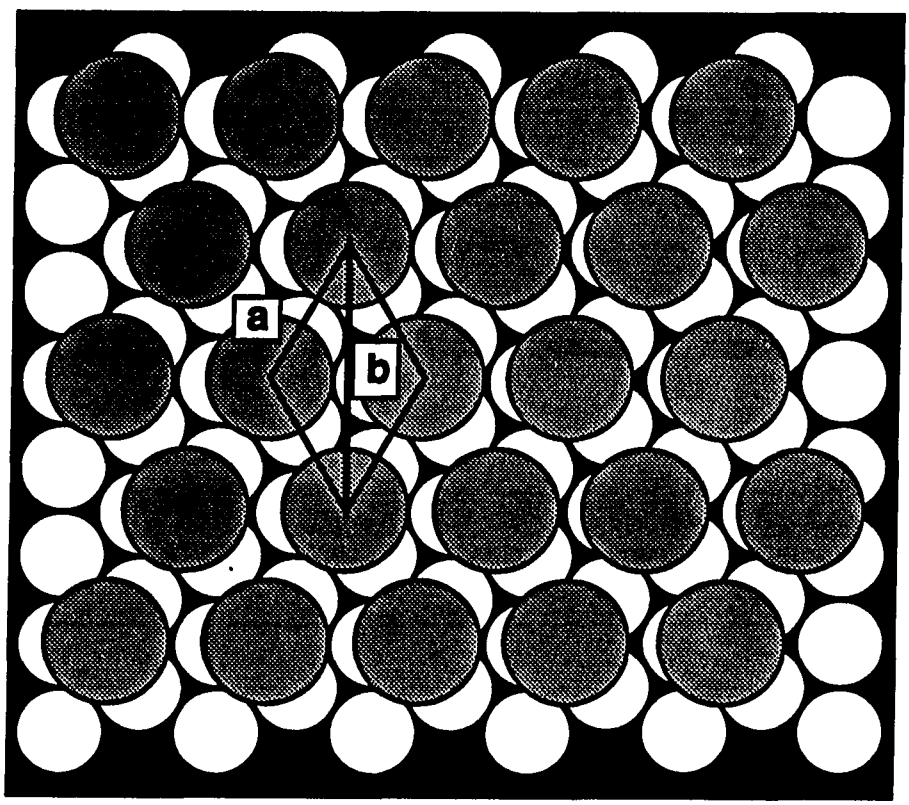

Figure 4. A scale drawing of the $(\sqrt{3} \times \sqrt{3})R30°$ overlayer with the underlying Au(111) surface. The open circles represent the Au atoms and the shaded circles represent the hydrocarbon chain. The nearest- and next-nearest-neighbor spacings are (a) 0.50 nm and (b) 0.87 nm, respectively, as marked on the figure (see text for additional details).

In addition to packing information, the large area scan in Figure 3A shows that the hexagonal periodicity extends over an 8 nm x 8 nm region. We have occasionally seen continuous periodicity over much larger areas (~600 nm^2). Such a finding suggests the potential value of STM for probing relationships between macroscopic properties such as wetting[4h,4i,6] and the domain size of the monolayers.

Also apparent in Figure 3A are rows of the adsorbate that appear brighter than others. We believe these rows correspond to single atomic steps on the substrate surface, though it is not clear if their "raised" appearance has chemical significance or is an artifact of imaging. For example, binding at edge sites should involve different adsorbate-substrate orbitals, which may be manifested in the images. However, this "brightness" may also occur because electrons can tunnel both vertically and laterally between the tip and substrate as the tip approaches the step edge from the upper surface.

STM Images of *n*-Octadecanethiolate Monolayers on Au(111).

Figures 5A and 5B show STM images of an OT-coated Au sample for respective areas of 8.15 nm x 8.15 nm and 2.65 nm x 2.65 nm. As with the ET coated samples, a hexagonal structure is evident with nearest- and next-nearest-neighbor spacings that are markedly different than that for uncoated Au(111). The spacings of the images, which are outlined in black in Figure 5B, are consistent with the $(\sqrt{3} \times \sqrt{3})R30°$ overlayer found at our ET coated samples. We also note that the images for the OT monolayers are

Figure 5. (A) STM image of a 8.15 x 8.15 nm^2 section of *n*-octadecane-thiolate on an epitaxially grown Au film on mica. The image is low pass filtered and recorded in the constant height mode with a bias voltage of -200 mV and a 2 nA tunneling current.

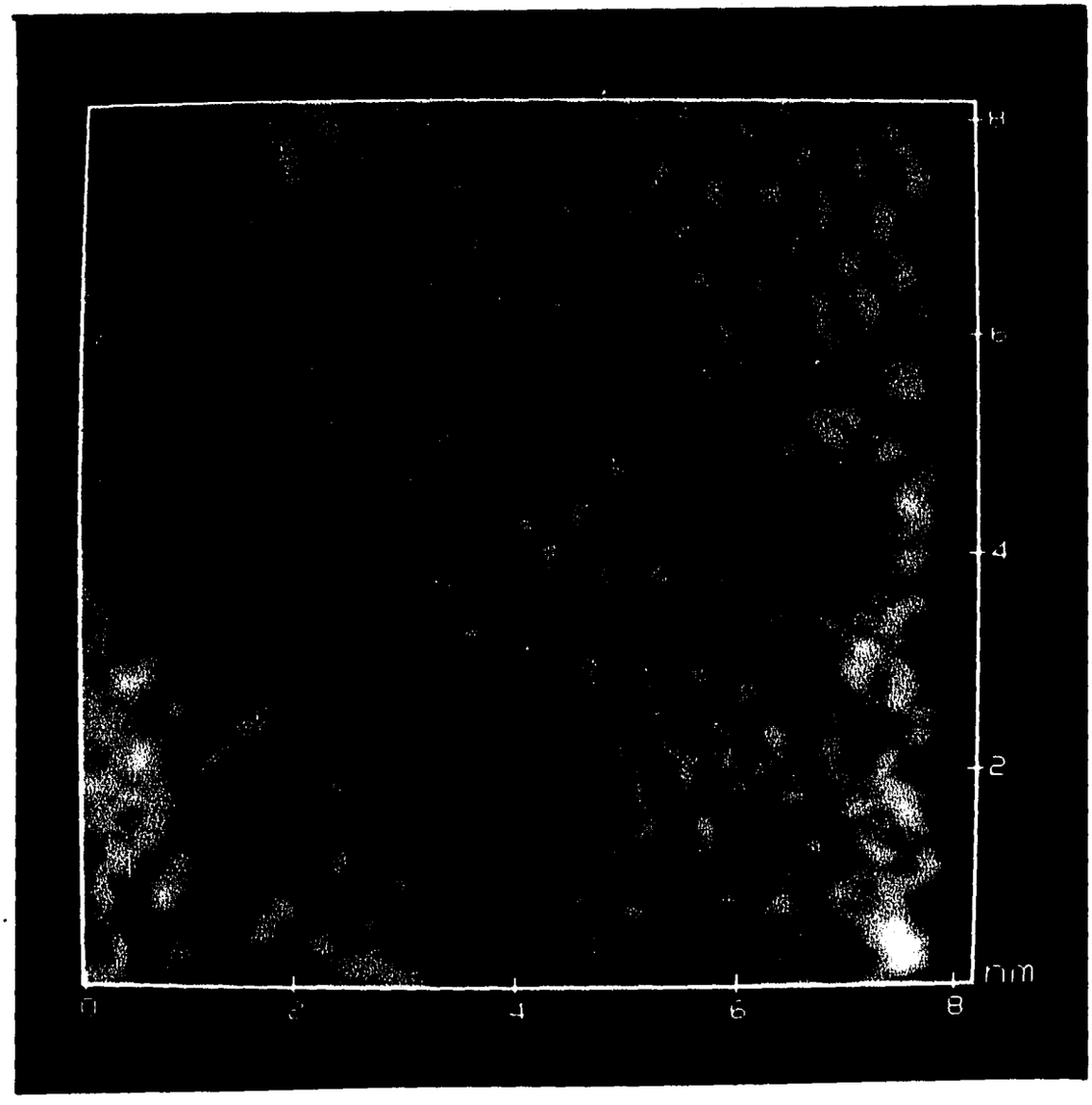
8
6
4
2
nm
0
2
4
6
8

Figure 5 (cont'd). (B) STM image of a 2.65 x 2.65 nm^2 section of *n*-octadecanethiolate on an epitaxially grown Au film on mica using the same conditions as Figure 5A. The spacings marked on Figure 5B are (a) 0.50 ± 0.02 nm and (b) 0.88 ± 0.04 nm.

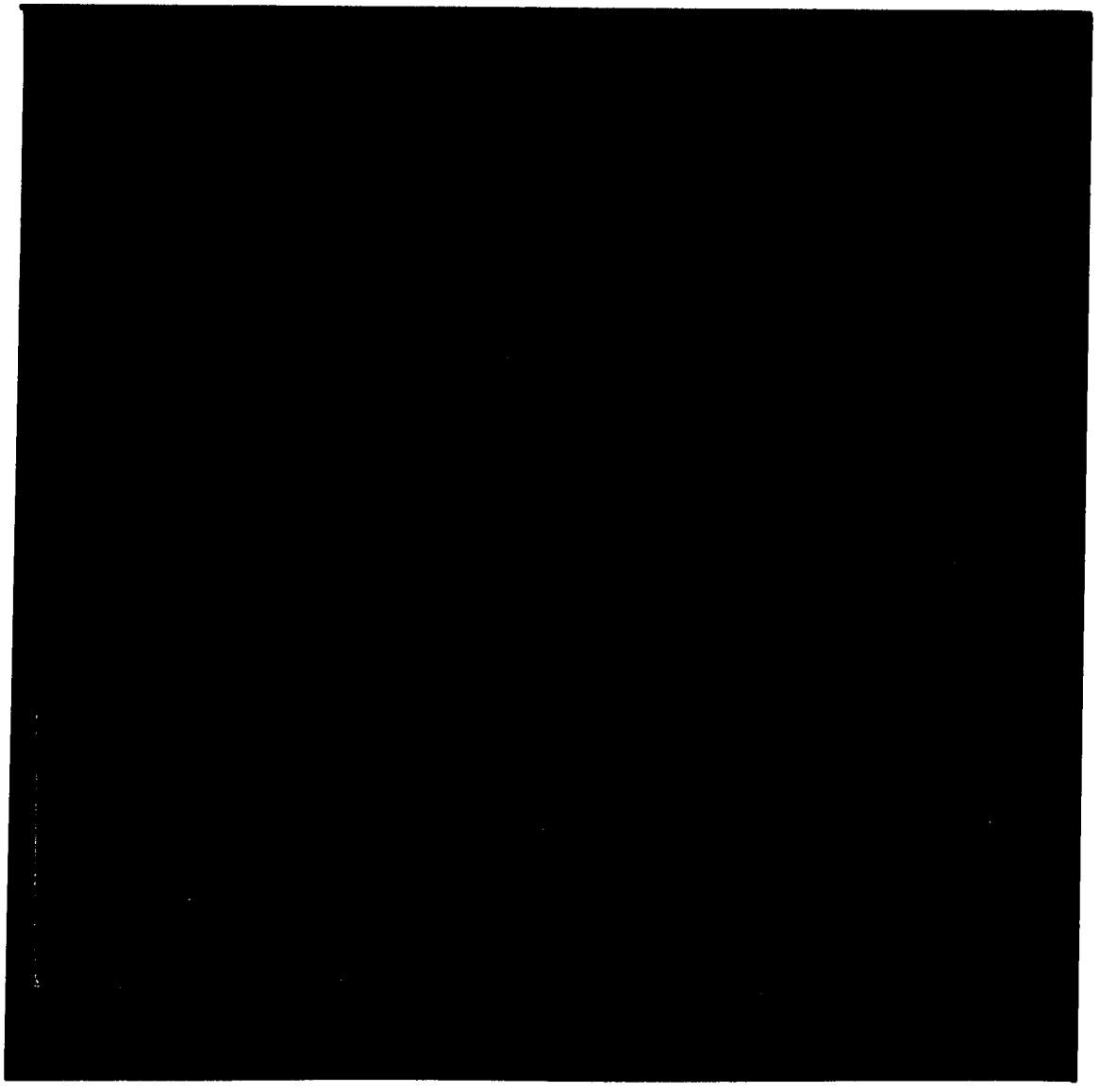

consistently noisier than those observed for the ET coated surfaces and that we have not been able to obtain images for the OT overlayers over as large an area as the ET overlayers. Although not understood, we presently attribute both differences to the presence of the longer alkyl chain of OT.

Taken together, the images in Figures 3 and 5 indicate that our monolayers can be successfully characterized at an atomic scale with STM. These results further reveal that the adsorbate adopts a $(\sqrt{3} \times \sqrt{3})R30°$ overlayer arrangement on a Au(111) lattice.

Comparison with Structural Descriptions of Thiols on Au from Macroscopic Data.

Although our images reveal the two-dimensional arrangement for only an extremely small fractional area of the overlayer, comparisons with structural descriptions developed from "macroscopic" measurements argue that the observed packing is a reasonable representation of the predominant structure at the surface. For example, we have recently discovered that *n*-alkanethiolate monolayers at Au(111) can be desorbed by a one-electron reduction[3]. Integration of the charge for the desorption provides a measure of the adsorbate surface coverage. After accounting for roughness, we found a surface coverage of 8.4 ($\pm$ 0.7) x 10^{-10} moles/cm^2 for all of the thiolate monolayers tested ($CH_3(CH_2)_nSH$, n = 3-18). This value agrees reasonably well with the theoretical 7.6 x 10^{-10} moles/cm^2 coverage expected for a $(\sqrt{3} \times \sqrt{3})R30°$ overlayer at Au(111). In addition, a closest-packed array of alkyl chains in a $(\sqrt{3} \times \sqrt{3})R30°$ overlayer structure would exhibit a chain tilt of

~35° from the surface normal[14]. Such a tilt is consistent with the 30° to 40° average tilts determined for long chain alkanethiol monolayers by an orientational analysis of infrared reflection spectroscopic data.[4d,4i] Taken together, the similarities of the structural descriptions provided by these macroscopic measurements and by our STM images suggest that the ($\sqrt{3}$ x $\sqrt{3}$)R30° overlayer is the predominant two-dimensional arrangement of our *n*-alkanethiolate monolayers at Au(111). To develop this description further, we are beginning experiments to assess the relationship between imperfections in the substrate (e.g. grain boundaries) and structural imperfections in the monolayer.

Possible Mechanism for the Imaging of Alkanethiolate Adsorbates.

Assumptions concerning the relative position of the microscope tip from the sample surface during imaging influence the structural interpretation of the images. As previously stated, we believe that our images result from electrons tunneling between the tip and the Au-bound S of the alkanethiolate adsorbate. The conclusion is based primarily on the observation that both the coated and uncoated Au samples can be successfully imaged with comparable tunneling currents and bias voltages. This argues that imaging under our experimental conditions is not observably affected by the presence of the hydrocarbon layer, although, as noted, the "long chain" images are typically noisier that the "short chain" images. As such, we believe that the tip is positioned near the Au-S interface during imaging. Interestingly, recent studies of Langmuir Blodgett films of

cadmium arachidate, phospholipids[8d,8j] and adsorbed detergent layers[8k] have yielded images indicative of the structure of the outer boundaries of the organic film, a separation distance of 3 to 5 nm between the tip and the substrate. Such large separation distances suggest that a "through-bond" long-range electron-transfer mechanism[16] may also be operative in imaging with STM.[8k] The ability to image both our coated and uncoated Au samples under the same conditions, however, argues that a "through-bond" mechanism plays a minor role in imaging our monolayers. We are presently assessing the validity of our interpretation through measurements of the heights of the tunneling barriers of the layers and considerations of current theoretical models.[17]

CONCLUSION

The most significant statement concerning these results herein is that we have found it possible to resolve atomically sized features of monomolecular organic films on gold by STM under ambient conditions. This finding adds to the rapidly growing list of imageable adsorbates and suggests a promising future for the utilization of STM in a number of areas in which detailed information concerning the structure at a metal/adsorbate interface in a non-ultra high vacuum environment is desired. Our results also complement and enhance the current understanding of the packing arrangement of *n*-alkanethiolate films on gold. We have observed domains of adsorbate surface structure that are well described as $(\sqrt{3} \times \sqrt{3})R30°$ overlayers commensurate with a Au(111) substrate. This is in agreement with structures proposed for *n*-alkanethiolate layers based on the results of helium diffraction[1] and transmission electron diffraction[2] studies. We have also been able to observe continuous domains of this structure for areas as large as 25 x 25 nm. Though sampling has not yet been extensive enough to determine if such domain sizes are typical, such an observation suggests the potential value of STM for addressing important questions about the long-range order within the adsorbate layer. Experiments are underway to evaluate further the capability to image these and various other hydrocarbon-based monolayers.

ACKNOWLEDGEMENTS

MDP gratefully acknowledges the support of a Dow Corning Assistant Professorship. Acknowledgement is also made to the donors of the Petroleum Research Fund, administered by the American Chemical Society. Ames Laboratory is operated for the U.S. Department of Energy by Iowa State University under Contract No. W-7405-eng-82. This work was supported by the Office of Basic Energy Sciences, Chemical Science Division.

REFERENCES AND NOTES

1. Chidsey, C.E.D.; Liu, G-Y.; Rowntree, P.; Scoles, G. *J. Chem. Phys.* **1989**, *91(7)*, 4421-4423.

2. (a) Strong, L.; Whitesides, G.M. *Langmuir* **1988**, *4*, 546-558, and for additional details (b) Chidsey, C.E.D.; Loiacono, D.N. *Langmuir* **1990**, *6*, 682-691.

3. Evidence that these monolayers form as an *n*-alkanethiolate at the Au surface is given in Widrig, C.A.; Chung, C.; Porter, M.D. *J. Electroanal. Chem.*, accepted.

4. Examples concerning organosulfur monolayers at Au include: (a) Nuzzo, R.G.; Allara, D.L. *J. Am. Chem. Soc.* **1983**, *105*, 4481-4483.
(b) Li, T-T.; Weaver, M.J. *J. Am. Chem. Soc.* **1984**, *106*, 6107-6108.
(c) Nuzzo, R.G.; Zegarski, B.R.; Dubois, L.H. *J. Am. Chem. Soc.* **1987**, *109*, 733-740.
(d) Porter, M.D.; Bright, T.B.; Allara, D.L.; Chidsey, C.E.D. *J. Am. Chem. Soc.* **1987**, *109*, 3559-3568.
(e) Sabatani, E.; Rubinstein, I. *J. Phys. Chem.* **1987**, *91*, 6663-6669.
(f) Bain, C.D.; Troughton, E.B.; Tao, Y-T.; Evall, J.; Whitesides, G.M.; Nuzzo, R.G. *J. Am. Chem. Soc.* **1989**, *111*, 321-335.
(g) Finklea, H.O.; Snider, D.A.; Fedyk, J. *Langmuir* **1990**, 6, 371-376.
(h) Dubois, L.H.; Zegarski, B.R.; Nuzzo, R.G. *J. Am. Chem. Soc.* **1990**, *112*, 570-579.
(i) Nuzzo, R.G.; Dubois, L.H.; Allara, D.L. *ibid.*, 558-569.

5. (a) Sandroff, C.J.; Garoff, S.; Leung, K.P. *Chem. Phys Lett.* **1983**, *96*, 547-551. (b) Joo, T.H.; Kim, K.; Kim, M.S. *J. Phys. Chem.* **1986**, *90*, 5816-5819. (c) Blackman, L.C.F.; Dewar, M.J.S.; Hampson, H. *J. Appl. Chem* **1957**, *7*, 160-171.

(d) Prince, N.P.; Seymour, D.L.; Woodruff, D.P.; Jones, R.G.; Walter, W. *Surface Science* **1989**, *215*, 566-576.

(e) Sobocinski, R.L.; Bryant, M.A.; Pemberton, J.E. *J. Am. Chem. Soc.* **1990**. *112*, 6177-6183.

(f) Walczak, M.M; Chung, C.; Stole, S.M.; Widrig, C.A.; Porter, M.D. *J. Am. Chem. Soc.*, accepted.

6. For additional leading references see: Whitesides, G.M. and Laibinis, P.E. *Langmuir* **1990**, *6*, 87-96.

7. Binnig, G.; Rohrer, H. *Surf. Sci.* **1983**, *126*, 236-244.

8. See, for example: (a) Feng, L.; Hu, C.Z.; Andrade, J.D. *J. Microscopy* **1988**, *152(3)*, 811-816.

(b) Hubacek, J.S.; Brockenbrough, R.T.; Gammie, G.; Skala, S.L.; Lyding, J.W.; Latten, J.L.; Shapley, J.R. *J. Microscopy* **1988**, *152(1)*, 221-227.

(c) Braun, H.G.; Fuchs, H.; Shrepp, W. *Thin Solid Films* **1988**, *159*, 301-314. (d) Lang, C.A.; Horber, J.K.H.; Hansch, T.W.; Heckl, W.M.; Mohwald, H. *J. Vac. Sci. Technol. A* **1988**, *6(2)*, 368-370.

(e) Eng, L.; Hidber, H.-R.; Rosenthaler, L.; Staufer, U.; Wiesendanger, R.; Guntherodt, H.-J.; Tamm, L. *J. Vac. Sci. Technol. A* **1988**, *6(2)*, 358-359.

(f) Smith, D.P.E.; Horber, H.; Gerber, Ch.; Binnig, G. *Science* **1989**, *245*, 43-45. (g) Smith, D.P.E.; Horber, J.K.H.; Binnig, G.; Nejoh, H. *Nature* **1990**, *344*, 641-644.

(h) Foster, J.S. and Frommer, J.E. *Nature* **1988**, *333*, 542-545.

(i) Smith, D.P.E.; Bryant, A.; Quate, C.F.; Rabe, J.P.; Gerber, Ch.; Swalen, J.P. *Proc. Natl. Acad. Sci. USA* **1987**, *84*, 969-972.

(j) Horber, J.K.H.; Lang, C.A.; Hansch, T.W.; Heckl, W.M.; Mohwald, H. *Chem. Phys. Lett.* **1988**, *145*, 151-158.

(k) Wu, X-L.; Lieber, C.M. *J. Phys. Chem.* **1988**, *92*, 5556-5557.

(l) Rabe, J.P.; Sano, M.; Batchelder, D.; Kalatchev, A.A. *J. Microscopy* **1988**, *152(2)*, 573-583.

(m) Moller, R.; Cohen, R.; Esslinger, A.; Koslowski, B. *J. Vac. Sci. Technol. A* **1990**, *8(1)*, 659-660.

(n) Ohtani, H.; Wilson, R.J.; Chiang, S.; Mate, C.M. *Phys. Rev. Lett.* **1988**, *60(23)*, 2398-2401.

(o) McMaster, T.J.; Carr, H.; Miles, M.J.; Cairns, P.; Morris, V.J. *J. Vac. Sci. Technol. A* **1990**, *8(1)*, 648-651.

(p) Beebe, T.P.; Wilson, T.E.; Ogletree, D.F.; Katz, J.E.; Balhorn, R.; Salmeron, M.B.; Siekhaus, W.J. *Science* **1989**, *243*, 370-372.

(q) Hameroff, S.; Simic-Krstic, Y.; Vernetti, L.; Lee, Y.C.; Sarid, D.; Wiedmann, J.; Elings, V.; Kjoller, K.; McCuskey, R. *J. Vac. Sci Technol. A* **1990**, *8(1)*, 687-691.

(r) Sotobayashi, H.; Schilling, T.; Tesche, B. *Langmuir* **1990**, *6*, 1246-1250.

9. See, for example: (a) Schardt, B.C.; Yau, S-L.; Rinaldi, F. *Science* **1989**, *243*, 1050-1053.
(b) Ogletree, D.F.; Ocal, C.; Marchon, B.; Somorjai, G.A.; Salmeron, M.; Beebe, T.; Siekhaus, W. *J. Vac. Sci. Technol. A* **1990**, *8(1)*, 297-301.
(c) Marchon, B.; Ogletree, D.F.; Bussell, M.E.; Somorjai, G.A.; Salmeron, M.; Siekhaus, W. *J. Microscopy* **1988**, *152(2)*, 427-439.
(d) Tokumoto, H.; Miki, K.; Murakami, H.; Bando, H.; Ono, M.; Kajimura, K. *J. Vac. Sci. Technol. A* **1990**, *8(1)*, 255-258.
(e) Avouris, Ph.; Wolkow, R. *Phys. Rev. B* **1989**, *39(8)*, 5091-5100.

10. Chidsey, C.E.D.; Loiacono, D.N.; Sleator, T.; Nakahara, S. *Surface Science* **1988**, *200*, 45-66.

11. (a) Hallmark, V.M.; Chiang, S.; Rabolt, J.F.; Swalen, J.D.; Wilson, R.J. *Phys. Rev. Lett.* **1987**, *59(25)* 2879-2882.
(b) Emch, R.; Nogami, J.; Dovek, M.M.; Lang, C.A.; Quate, C.F. *J. Appl. Phys.* **1989**, *65*, 79-84.

12. Yau, S-L.; Vitus, C.M.; Schardt, B.C. *J. Am. Chem. Soc.* **1990**, *112*, 3677-3679.

13. We have occasionally found complex images that we have not yet been able to interpret. Interestingly, we have not found these complex images with atomic force microscopy; only images comparable to Figures 3 and 5 have been observed. Presently, we do not know what variation in experimental parameters causes these complex images.

14. Ulman, A.; Eilers, J.E.; Tillman, N. *Langmuir* **1989**, *5*, 1147-1152.

15. This determination was based on comparing the underpotential deposition (UPD) of Pb(II) onto the Au films on mica to published UPD curves on Au single crystal faces (J.W. Schultze and D. Dickertman, *Surf. Sci.* **1976**,*54*, 489, and K. Engelsman, W.J. Lorenz, E. Schmidt, *J. Electroanal. Chem.* **1980**, *114*, 1).

16. (a) Closs, G.L.; Calcaterra, L.T.; Green, N.J.; Penfield, K.W.; Miller, J.R. *J. Phys. Chem.* **1986**, *90*, 3673.

(b) Penfield, K.W.; Miller, J.R.; Paddon-Row, M.N.; Cotsaris, E.; Oliver, A.M.; Hush, N.S. *J. Am. Chem. Soc.* **1987**, *109*, 5061.

17. (a) Tersoff, J. and Hamann, D.R. *Phys. Rev. Lett.* **1983**, *50*, 1998-2001.

(b) Tersoff, J. and Hamann, D.R. *Phys. Rev. B* **1985**, *31*, 805-813.

PAPER 2. ATOMIC SCALE IMAGING OF ALKANETHIOLATE MONOLAYERS AT GOLD SURFACES WITH ATOMIC FORCE MICROSCOPY

ABSTRACT

Monolayer films formed by the chemisorption of alkanethiols ($CH_3(CH_2)_nSH$, n=1-17) at epitaxially grown Au(111) films were examined using atomic force microscopy (AFM). Atomically resolved images were found for films with n≥4, directly revealing for the first time the arrangement of the alkyl chain structure. All of the images exhibit a periodic hexagonal pattern of equivalent spacings (e.g. respective nearest- and next-nearest-neighbor distances of 0.52 ± 0.03 nm and 0.90 ± 0.04 nm for n=17, and 0.51 ± 0.02 nm and 0.92 ± 0.06 for n=5). These spacings agree well with the analogous 0.50 nm and 0.87 nm distances of a $(\sqrt{3} \times \sqrt{3})R30°$ adlayer on a Au(111) lattice, the two-dimensional arrangement reported in recent diffraction[1-3] and scanning tunneling microscopy[4,5] studies. In some instances, images with the above spacings were observed to extend continuously over areas as large as 100 nm^2, suggesting the potential of AFM to reveal both the short- and long-range order of the alkyl chains of these and other model interfacial structures. The implications of these findings, including the inability to obtain well-resolved images for films with n≤3, are examined in the context both of the current structural descriptions of alkanethiolate monolayers and of general issues related to imaging organic films with AFM.

INTRODUCTION

The atomic force microscope[6] (AFM) and its predecessor, the scanning tunneling microscope[7] (STM), have emerged as powerful tools for imaging semiconductor,[8] metallic,[9] organic,[10] and biological[11] surfaces with atomic-scale resolution in environments ranging from ultra high vacuum to aqueous solutions. We have recently begun to assess the applicability of both techniques for imaging model organic interfacial systems, such as the alkanethiolate[12] monolayers that form on gold surfaces. The goal is to develop detailed descriptions of the short- and long-range packing arrangements of these monolayers that will serve as a basis for correlating the interfacial microstructure with macroscopic observables (e.g. wettability[13] and electron-transfer properties[2b,14]). In an earlier effort,[4] we demonstrated that STM can reveal the two-dimensional arrangement of alkanethiolate monolayers at gold--observations attributed to electrons tunneling between the STM tip and the gold surface through the thiolate head group. As our explorations of the capabilities of STM and AFM progressed, we discovered that it was also possible to image these monolayers using AFM under ambient conditions. This paper reports the results of our findings.

In the following sections, we present the first atomically resolved AFM images of monolayers formed by the chemisorption of alkanethiols ($CH_3(CH_2)_nSH$) at epitaxially grown Au(111). To set a foundation for the discussion of our images, we first describe the conditions that lead to the observation of atomic structure using AFM. This section also contrasts the

ability to image these adsorbates using AFM and STM. Next, we present an atomically resolved AFM image of our mica-supported gold films. This image defines the (111) texture of the uncoated gold surfaces and functions as a reference for comparison to the images of the alkanethiolate-coated gold samples. The AFM images of the thiolate monolayers are then presented. Though difficult to define fully, we believe these images arise from interactions between the AFM tip and the alkyl chains of the resulting gold(I) alkanethiolate monolayer. Recent literature precedents[10a,11a,15-17] as well as results from attempts to image alkanethiolate monolayers of varied chain length (n=1-17) are used to support this contention. For $n \geq 4$, an image that corresponds to a $(\sqrt{3} \times \sqrt{3})R30°$ adlayer was found, the same two-dimensional arrangement found for these monolayers using diffraction[1-3] and STM[4,5] techniques. Images with a well defined periodicity have not yet been observed for monolayers with $n \leq 3$. We conclude with a brief assessment of images in the context of established and emerging structural descriptions of these monolayers.[12-14,18,19]

EXPERIMENTAL

Substrate Preparation.

Gold substrates with a predominantly (111) crystallinity were prepared by the resistive evaporation of 300 nm of gold onto freshly cleaved green mica sheets (Asheville-Schoonmaker, Newport News, VA) at a rate of 0.3 nm/s. Immediately prior to gold deposition, the mica sheets were heated in the vacuum chamber for ~1 hr at 250-300°C. During deposition, the pressure in a cryogenically pumped Edwards 306A vacuum chamber (Fairfield, CA) was held at ~2×10^{-6} torr. Subsequently, the gold-coated mica was allowed to cool radiatively to below 70°C before backfilling the chamber with dry nitrogen and removing the substrates. The substrates were then immediately immersed into the thiol solutions.

Previous macroscopic level characterizations of our evaporated gold films using STM[4] indicate that the gold films are composed of ~300 nm-wide crystallites that are separated by relatively deep grain boundaries. The roughness factor of the gold substrates, given by the electrochemically determined area[20] divided by the geometric area, equals 1.1 ± 0.1.[21] At a microscopic level, the surfaces of the uncoated gold films are strongly (111) textured[21] (>95%), based on comparisons of the voltammetric curves for the underpotential deposition of Pb(II) to literature data at single crystal gold electrodes.[22] Images from STM[4] routinely exhibit the 0.29-nm interatomic spacing of Au(111). The latter findings are in general agreement with earlier STM[9d,e] and AFM[9a,b] reports as well as electron diffraction[9d,23,24] studies.

Monolayer Film Preparation.

Alkanethiolate monolayers were prepared by the chemisorption of the corresponding thiol on gold from ~1 mM ethanolic solutions using previously described protocols.[14a] Upon removal from solution, the samples were rinsed thoroughly with ethanol and dried in air. Varying immersion times from ~2 to 24 h had no observable effect on the resulting AFM images.

Instrumentation.

Images were obtained in air using a Digital Instruments Nanoscope II (Santa Barbara, CA). The instrument was equipped with a 0.7-μm AFM scan head. After loading a sample, the instrument was allowed to come to thermal equilibrium, which required ~30 min. All images were collected in air with the AFM tip in contact with the sample in the constant force mode (i.e. the height mode of the Nanoscope II). In this mode, the force between the AFM tip and the sample surface is held constant, and the vertical displacements of the sample needed to maintain the preselected force are recorded as the tip rasters across the surface. Triangularly shaped silicon nitride cantilevers with pyramidal tips (Digital Instruments) were used. The force constant of these cantilevers was 0.58 N/m. Images were acquired at a rate of 14 to 28 lines/s, requiring roughly 15 to 25 s per image. Imaging forces were ~50 nN, unless otherwise specified. The horizontal displacement of the tip was calibrated using freshly cleaved mica. Images were either smoothed

with an eight-point moving-average algorithm (i.e. the low-pass filter utility of the Nanoscope II) or lightly filtered with a XY spectrum filter.

Reagents.

Liquid alkanethiols ($CH_3(CH_2)_nSH$) were acquired from several sources (Alfa Products, n=1; Aldrich, n=2,4,6,7,8,15; Eastman Kodak, n=3,5,9,11; and Pfaltz and Bauer, n=13). Tridecanethiol and pentadecanethiol were synthesized from 1-bromotridecane (Aldrich) and 1-bromopentadecane (Aldrich), respectively, according to previous procedures.[18c] Undecanethiol and heptadecanethiol were gifts from Professor George Whitesides (Department of Chemistry, Harvard University). All of these compounds were purified by passage through a neutral alumina (Aldrich) column prior to use. Octadecanethiol (Aldrich) was recrystallized twice from absolute ethanol.

RESULTS AND DISCUSSION

General Observations.

Using the previously described experimental protocols, we have attempted to image alkanethiolate ($CH_3(CH_2)_nSH$) monolayers at our gold-coated mica substrates for a large range of chain lengths (n=1-17). Images with atomically resolved features have been observed only for $n \geq 4$. We have yet to obtain well defined images for $n \leq 3$. As with STM,[4] the conditions that yield a well defined AFM image have been difficult to define. We have found, however, that such images are more readily attained with AFM than with STM. We attribute this primarily to differences in the structural stabilities of the two types of tips. Tips for STM that resolved atomic scale structures functioned effectively for a period between several minutes and a few hours, after which the image gradually or suddenly disappeared. Tips for AFM, on the other hand, were routinely used for several days. We found on numerous occasions that once "in focus", the same area of the sample could be scanned continuously with AFM for several hours with little apparent degradation of the image.

In addition, we have found that the conditions yielding a well defined image varied somewhat with chain length. Both long-chain structures (e.g. n=17) and short-chain structures (e.g. n=5) could effectively be imaged under approximately the same force (~50 nN). However, the long-chain structures were able to withstand greater forces before the image degraded. We attribute the ability of the longer chain structures to withstand greater forces to increasing cohesive interactions between neighboring alkyl

chains.[1,13b,14a,18c,d] We have also observed that scanning at low forces (<20 nN) leads to the loss of image definition. We ascribe this loss of definition to two sources. First, contact between the AFM tip and sample at low forces may be intermittent with the tip repeatedly losing and regaining contact during a scan. Second, the tip may be imaging the extreme outer surface of the chain structure which, at least for longer chain lengths, is disordered with respect to the underlying polymethylene chain. Such disorder reflects the presence of gauche conformational defects at the chain terminus.[25] Further discussion of the implications of our observations is deferred until later.

AFM Images of Uncoated Epitaxially Grown Gold.

An atomically resolved AFM image of uncoated, epitaxially grown gold is shown in Figure 1. The image encompasses an area slightly larger than 3 nm by 3 nm. This and all other images are given in a top-view presentation in which the lighter portions of the gray vertical scale correspond to higher regions of the surface and the darker portions to lower regions of the surface. The image in Figure 1 is composed of a hexagonal pattern of bright spots. This is the only periodic feature found on such samples and is routinely observed in our laboratory with both AFM and STM.[4] The average nearest-neighbor distance, which is represented by the black line (a) overlaying a small portion of the image, is 0.29 ± 0.03 nm. This distance agrees well with the 0.288 nm nearest-neighbor spacing of the (111) face of gold,[26] as found in earlier atomic-scale images of mica-supported

Figure 1. AFM image of uncoated, epitaxially grown Au(111) on mica covering 3.02 nm x 3.02 nm. The image was collected in a constant force mode and was lightly filtered using a XY spectrum filter. The average nearest-neighbor spacing represented by line (a) equals 0.29 ± 0.03 nm and the next-nearest-neighbor spacing represented by line (b) is 0.50 ± 0.04 nm.

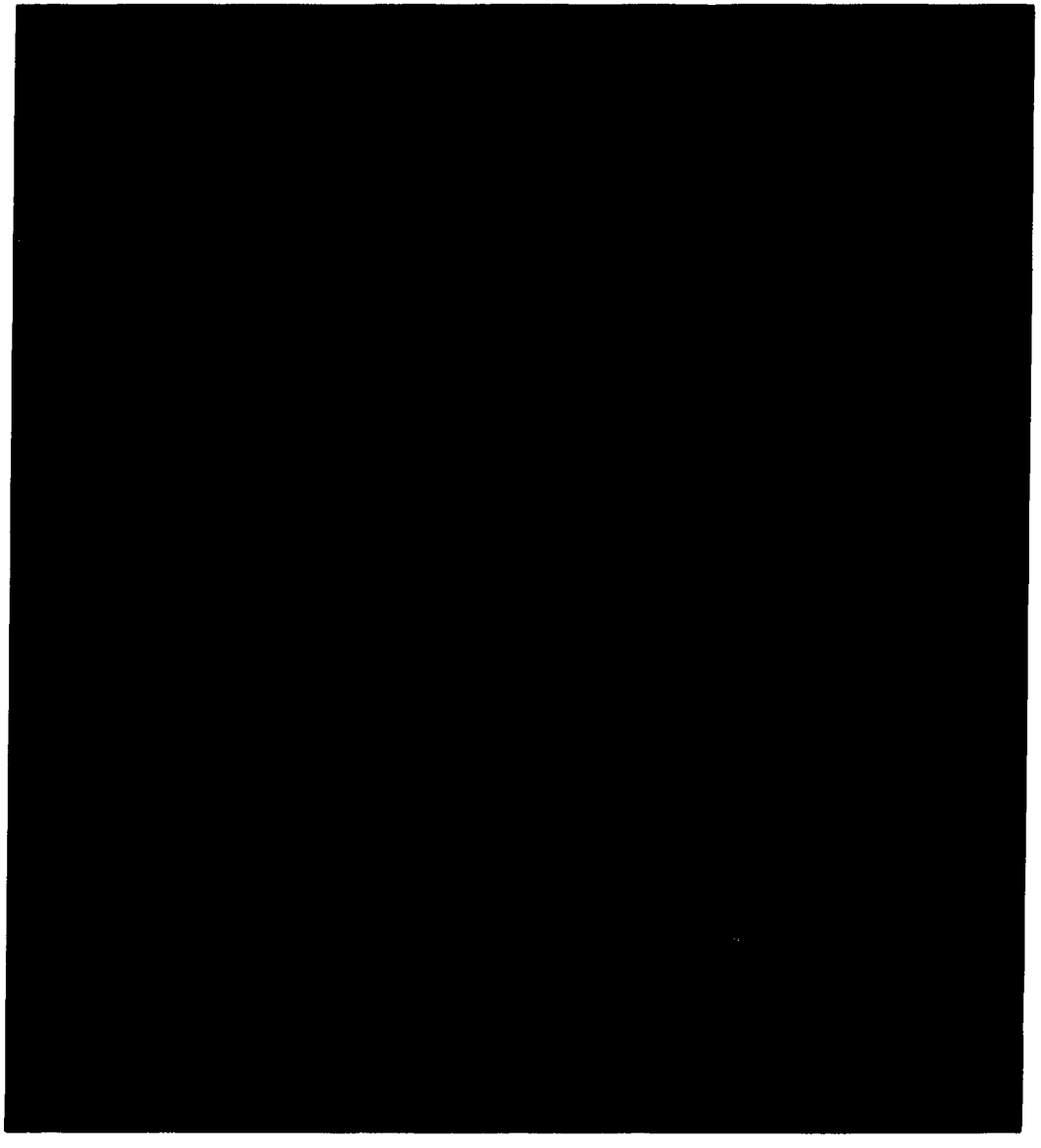

gold.[9a,b, d,e] Larger area scans show that the (111) periodicity extends over hundreds of square nanometers. Based on the combined weight of these and previous characterizations (see Experimental Section), we will refer to our gold substrates simply as Au(111).

AFM Images of Alkanethiolate Monolayers at Au(111).

Figure 2 shows images of alkanethiolate monolayers at Au(111) of three different chain lengths: (A) octadecanethiolate (n=17); (B) decanethiolate (n=9); and (C) hexanethiolate (n=5). Each image is presented with the same horizontal length scales as those in Figure 1. In all three images, a hexagonal pattern of bright spots with similar spacings is observed, the only periodic image observed to date for these films. These spacings are markedly larger than those of uncoated Au(111). The average respective nearest- and next-nearest neighbor distances, which are represented by the black lines in Figure 2A, equal 0.52 ± 0.03 nm and 0.90 ± 0.04 nm for n=17, 0.50 ± 0.02 nm and 0.91 ± 0.04 nm for n=9, and 0.51 ± 0.02 and 0.92 ± 0.06 nm for n=5. We have obtained images with similar spacings and uncertainties for alkanethiolate monolayers for the remainder of the series from n=4 to 17. These distances correspond to those expected for a $(\sqrt{3} \times \sqrt{3})R30°$ adlayer on a Au(111) lattice, the same two-dimensional arrangement that has been found for these monolayers using diffraction[1-3] and STM techniques.[4,5] For illustration,[28] a scale drawing of the $(\sqrt{3} \times \sqrt{3})R30°$ adlayer on Au(111) is shown in Scheme I.

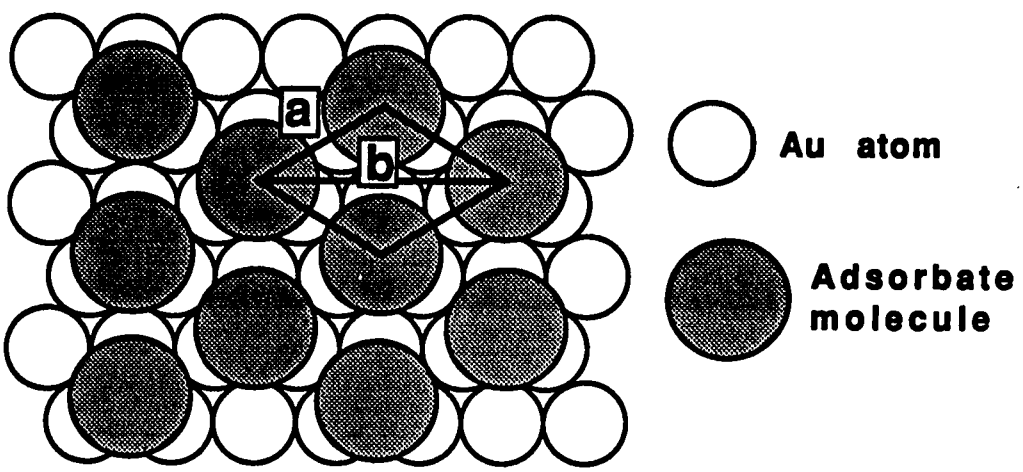

Scheme I

Figure 2. (A) AFM image covering 3.02 nm x 3.02 nm of octadecanethiolate at epitaxially grown Au(111). This image was collected in a constant force mode (~10 nN) and is lightly filtered using a XY spectrum filter. The nearest- and next-nearest-neighbor spacings are represented by the black lines, a and b, respectively. Average spacings for these distances are: a=0.52 ± 0.03 nm and b=0.90 ± 0.04 nm. These spacings correspond to a $(\sqrt{3} \times \sqrt{3})R30°$ adsorbate overlayer on Au(111).

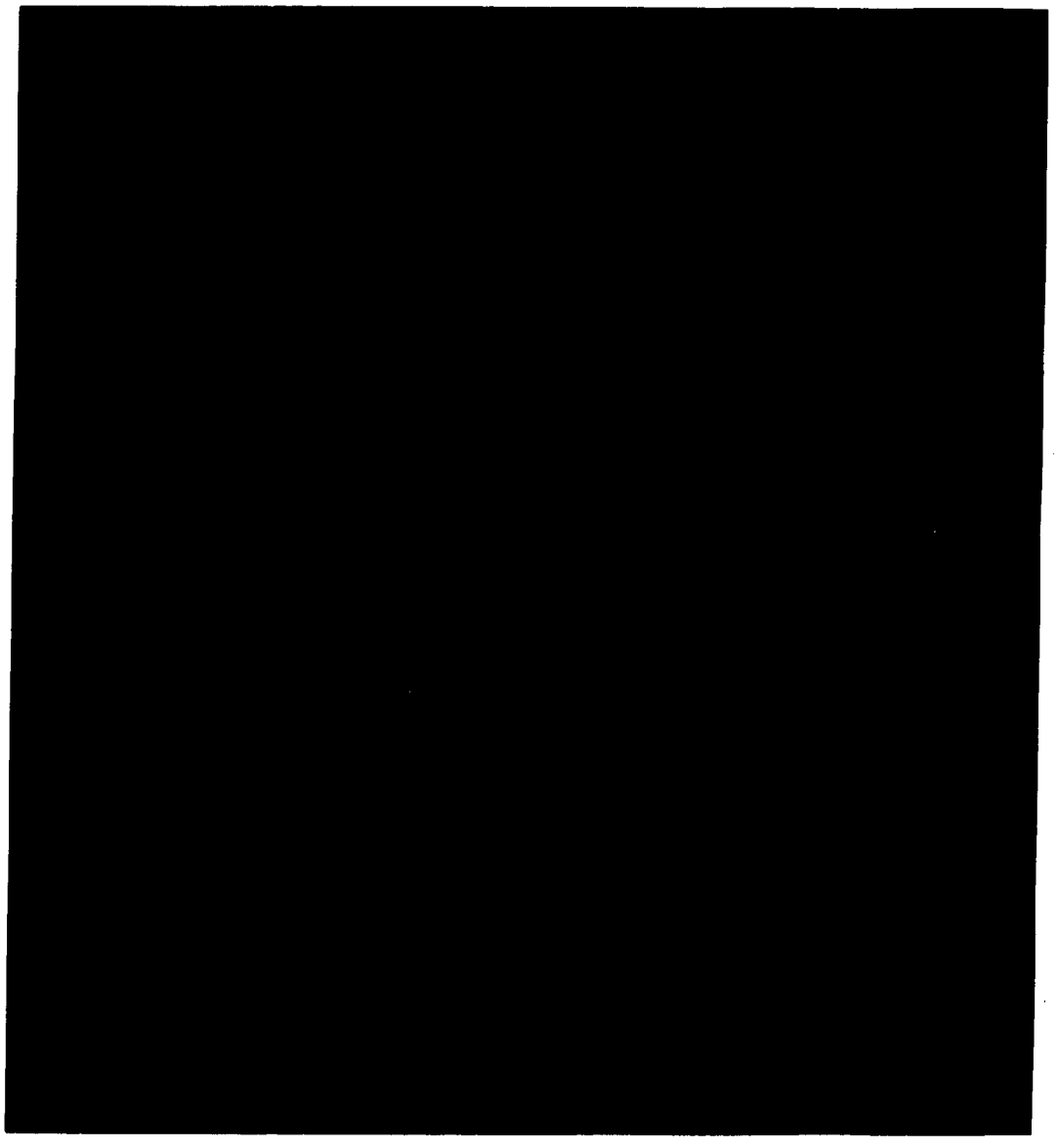

Figure 2 (cont'd). (B) AFM image covering 3.02 nm x 3.02 nm of decanethiolate[27] at epitaxially grown Au(111). This image was collected in a constant force mode (~10 nN) and is low-pass filtered. The nearest- and next-nearest-neighbor spacings are: $a=0.50 \pm 0.02$, $b=0.91 \pm 0.04$ nm

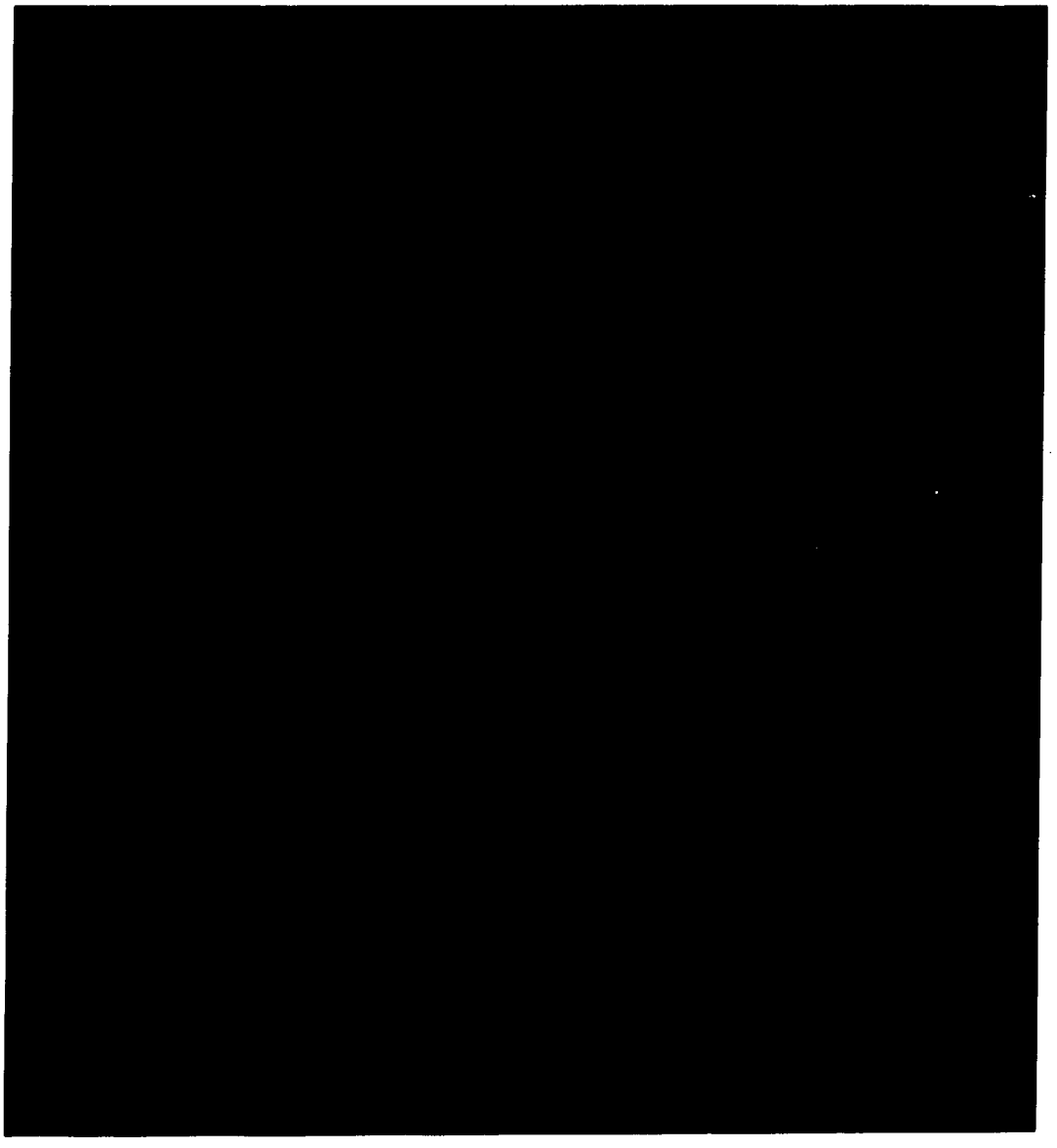

Figure 2 (cont'd). (C) AFM image covering 3.02 nm x 3.02 nm of hexanethiolate at epitaxially grown Au(111). This image was collected in a constant force mode (~10 nN) and lightly filtered using a XY spectrum filter. The nearest- and next-nearest-neighbor spacings are: a=0.51 ± 0.02 nm, b=0.92 ± 0.06 nm.

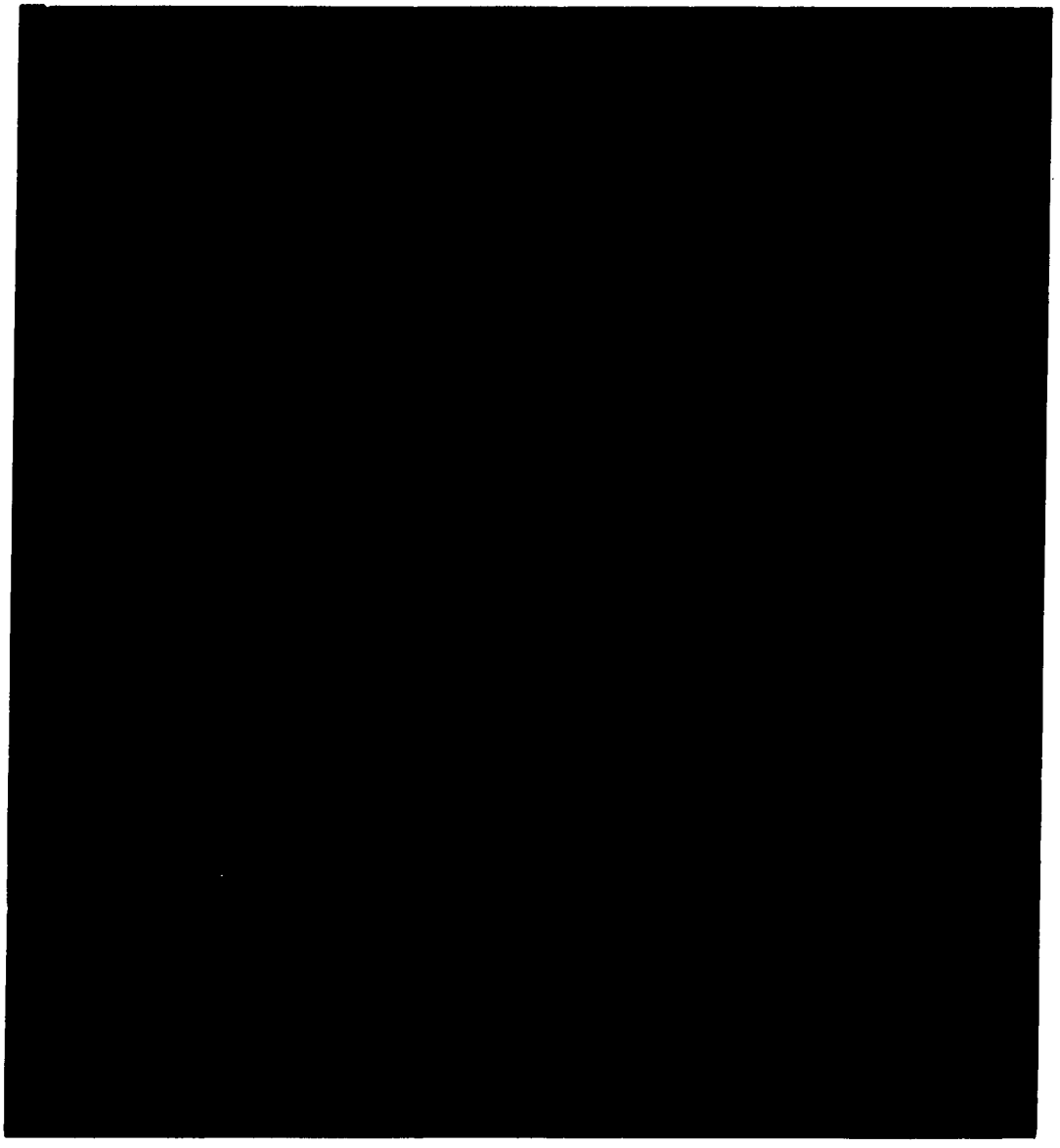

Figure 3 presents larger area images (8.45 nm x 8.45 nm) of the three monolayers shown in Figure 2. As previously noted, areas with a hexagonal pattern extend over a large portion of each image. The ordered areas, which are occasionally as large as 100 nm^2, are separated by regions of poor definition which vary in size. In contrast, areas as large as 600 nm^2 have been observed using STM.[4] Though tempting to ascribe these findings to differences in the long range order (i.e. domain size) of the head group relative to the alkyl chains, more extensive large area scanning is needed before such a conclusion could be reached. Larger area scans may also reveal possible correlations between domain sizes and chain length, as suggested by He diffraction,[1] a technique which probes the two-dimensional arrangement of the terminal methyl groups of these monolayers.

Taken together, the images in Figures 2 and 3, which are representative of findings from several hundred hours of scanning, demonstrate the capability of AFM to image alkanethiolate monolayers at gold surfaces with atomic-scale resolution. The images further reveal that these thiolates form a $(\sqrt{3} \times \sqrt{3})R30°$ adlayer on a Au(111) lattice, in agreement with the noted diffraction[1-3] and STM[4,5] findings. This structural arrangement is also consistent with the chain tilts deduced by infrared spectroscopic characterizations[13b,14a,29] and with surface coverages determined from electrochemical reductive desorption[12a,19] measurements, approaches that probe macroscopic details of interfaces.

Figure 3. (A) AFM image covering 8.45 nm x 8.45 nm of octadecanethiolate at epitaxially grown Au(111). This image is low-pass filtered.

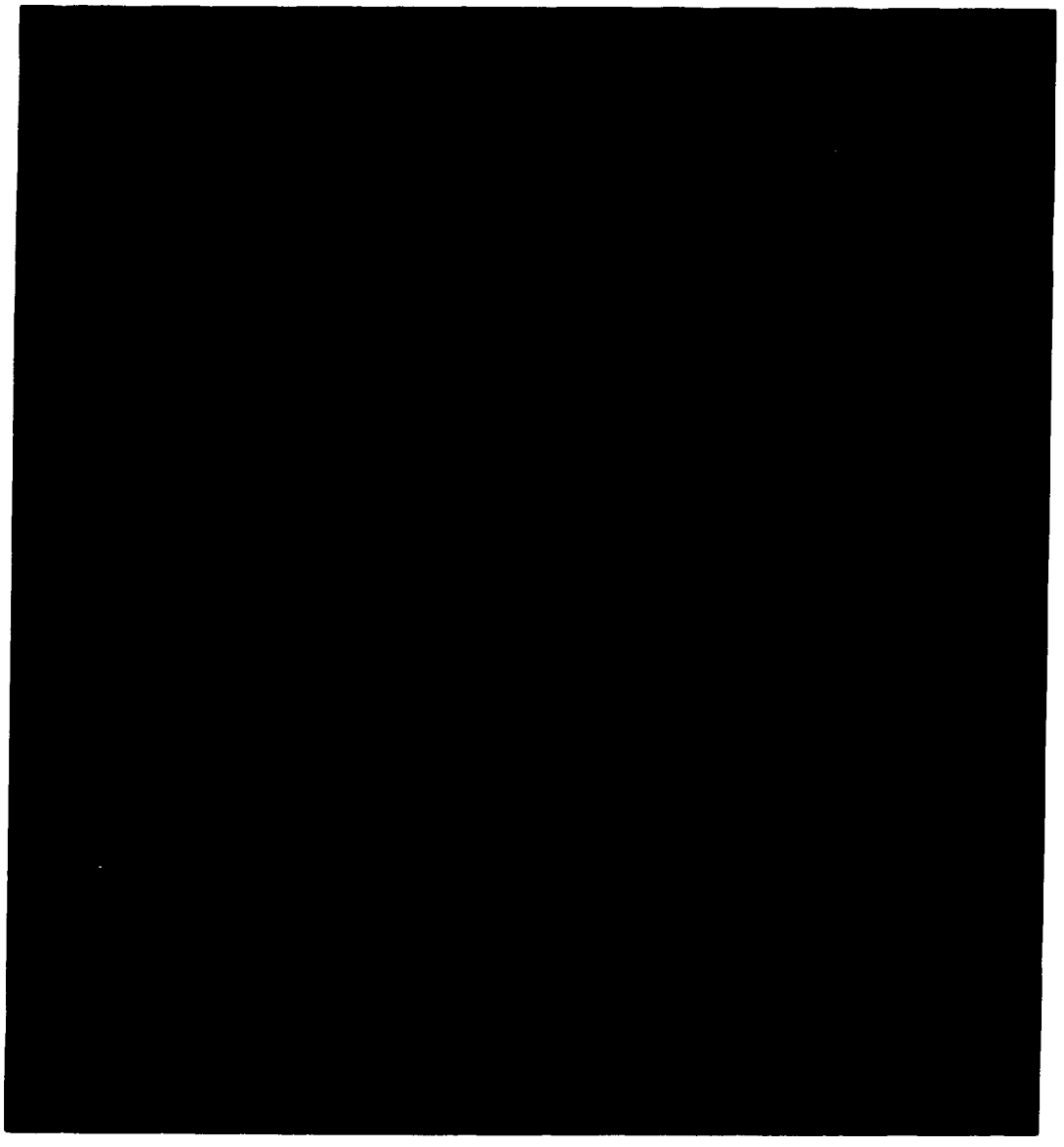

Figure 3 (cont'd). (B) AFM image covering 8.45 nm x 8.45 nm of decanethiolate at epitaxially grown Au(111). This image is low-pass filtered.

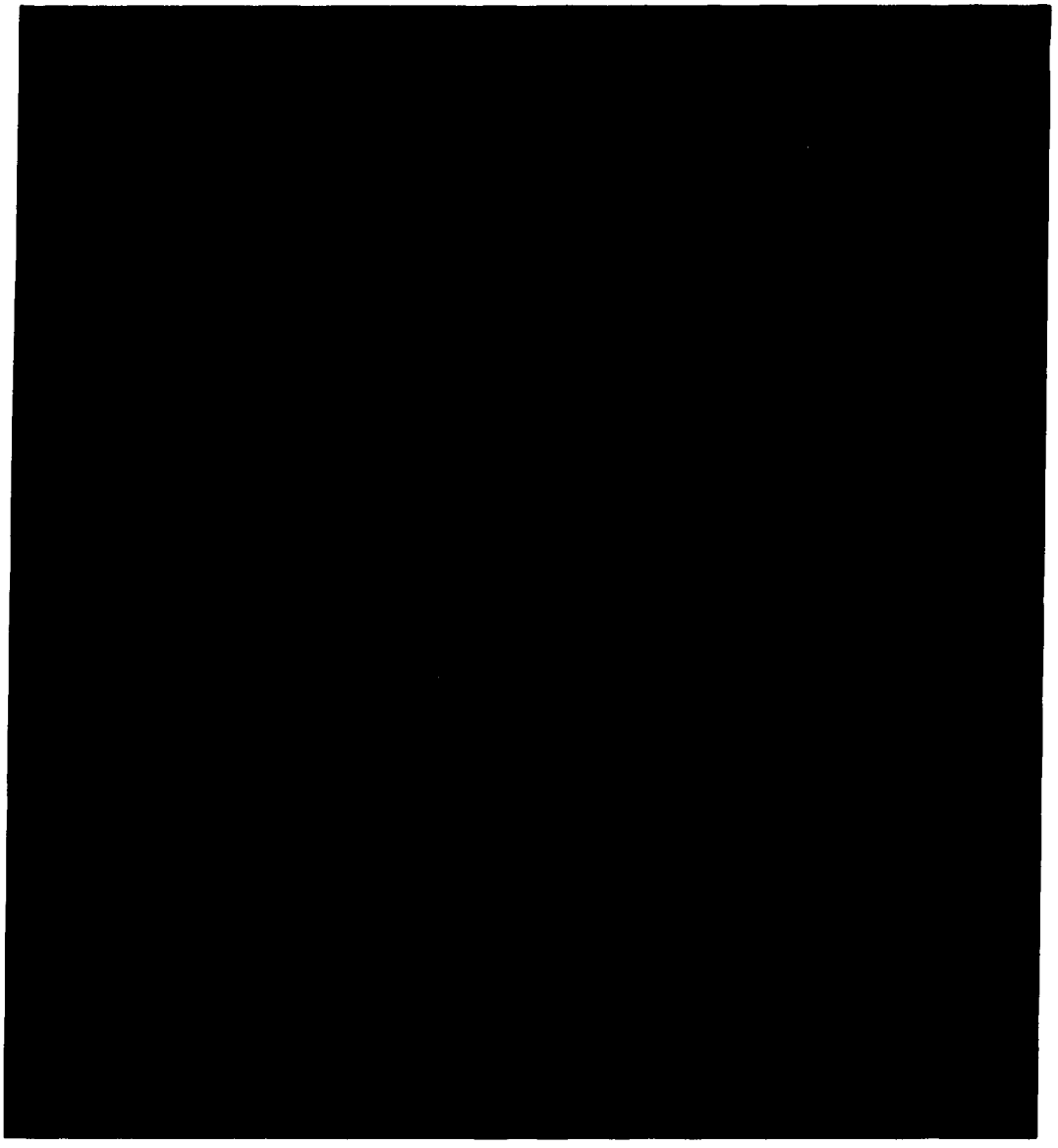

Figure 3 (cont'd). (C) AFM image covering 8.45 nm x 8.45 nm of hexanethiolate at epitaxially grown Au(111). This image is filtered lightly with a XY spectrum filter.

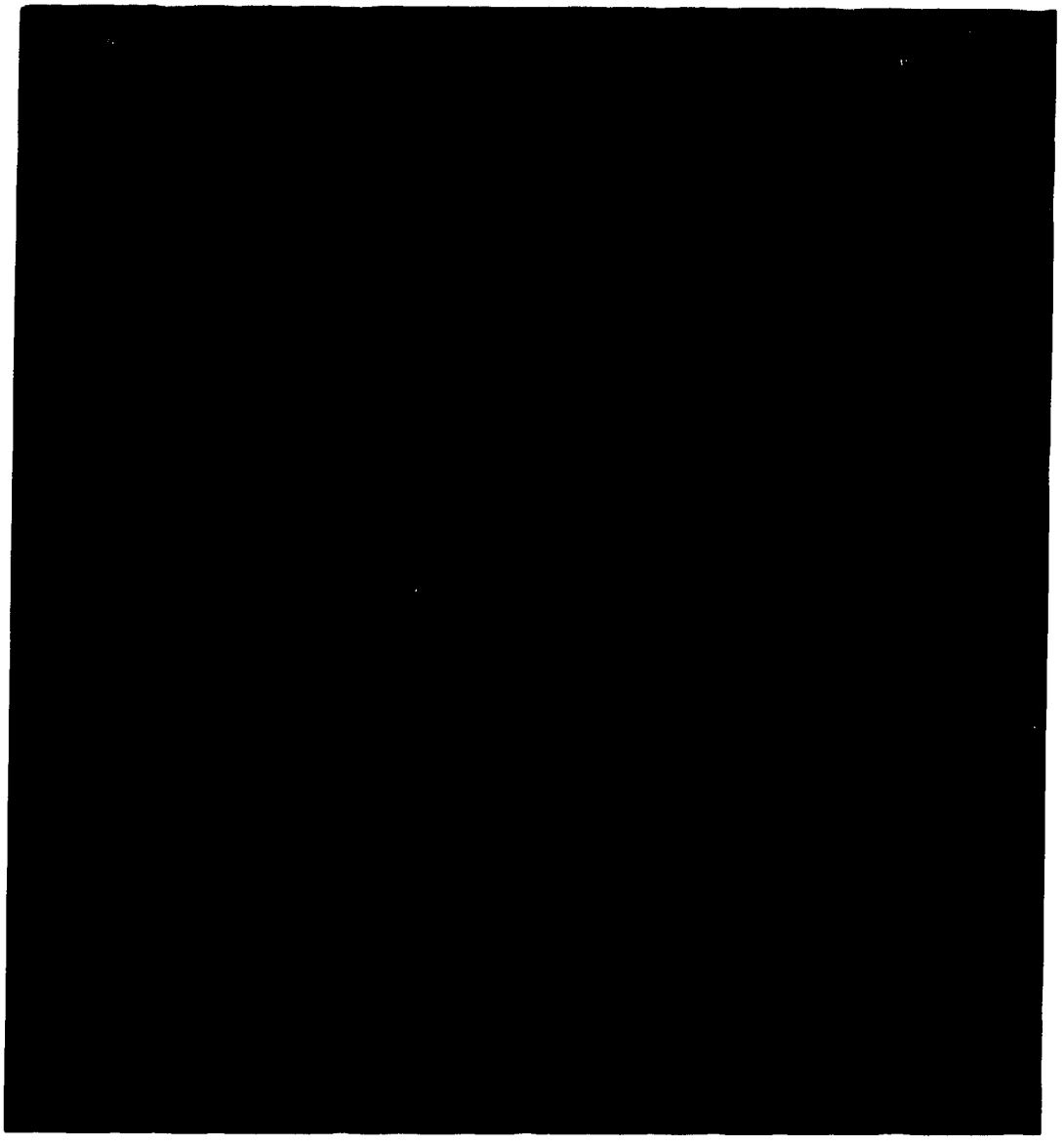

Imaging Mechanism.

To develop a structural interpretation of our images, it is important to determine the position of the AFM tip with respect to the sample surface. Such a determination would effectively identify the portion of the monolayer structure that is probed by the AFM tip (e.g. chain terminus or gold-bound thiolate). Model calculations have suggested that representative images of surfaces of individual biological macromolecules can be obtained only if the force between the AFM tip and sample is on the order of 0.01 nN.[30] Above this limit, the tip may deform the surface of the sample. We believe that both the strong cohesive interactions operative within the array of alkyl chains and the covalent linkage between the sulfur head group and the gold surface enable our alkanethiolate monolayers to withstand much larger imaging forces. These factors were not taken into account in the noted calculations.

Several literature precedents support the importance of both of the above factors in imaging with AFM. With respect to cohesive interactions, the recent atomically resolved images of a multilayer cadmium arachidate film[10a] and of other Langmuir-Blodgett-deposited films[11a] are particularly noteworthy. The images in both studies were acquired at ~10 nN. Force-distance profiles measured as an AFM tip approaches, contacts, and then penetrates into a film of cadmium arachidate[15] are in general accordance with these findings, with penetration occurring at ~7 nN. The importance of a strong linkage between an ordered overlayer and the support has been illustrated in recent friction and wear studies of multilayer films of cadmium

arachidate at the native oxide of a silicon substrate.[17] These studies found that the first layer, which is tethered to the oxide via acid-base chemistry, is ~1000 times more resistive to wear than the subsequent layers held together primarily by van der Waals forces. Together, the above results attest to the ability of organic films with structures similar to alkanethiolate monolayers to withstand forces similar to those used to acquire our images.

As stated previously, we attribute our images to interactions between the AFM tip and the alkyl chain structure of the monolayer. This conclusion, supported by the above literature findings,[10a,11a,15-17] is based on the differences in the capabilities of AFM and STM to image the atomic structure of short-chain ($n \leq 3$) alkanethiolates at Au(111). With STM,[4] for example, we have routinely obtained atomically resolved images of ethanethiolate (n=1) monolayers. We have ascribed these images to electrons tunneling between the STM tip and the gold surface through the sulfur head group, placing the STM tip near the gold surface. If the AFM tip images the gold-bound sulfur, one would then reasonably expect to obtain images with the hexagonal pattern for all chain lengths,[31] not only for $n \geq 4$. This result argues that the atomically resolved images of the longer chain ($n \geq 4$) monolayers arise from interactions between the AFM tip and the alkyl chain structure. The aforementioned chain length dependence of the range of forces that gave atomically resolved images is consistent with this interpretation. Interestingly, the inability to obtain images for $n \leq 3$ further suggests the most likely position of the AFM tip to be near the outermost carbons of the alkyl chains. However, it is not clear if the tip probes the

packing arrangement of the chain terminus or pushes through the first few carbons and images the underlying polymethylene chain structure. The latter possibility may have relevance to the inability to obtain atomically resolved images of the short-chain ($n \leq 3$) monolayers (i.e. the tip induces disorder). The inherent disorder of the short alkyl chain structures[1,13b,14a,18c,d] may also be a contributing (and possibly the dominant) factor. We are currently designing experiments in an attempt to resolve these issues.

CONCLUSIONS

This paper has demonstrated that it is possible to resolve atomic-scale features of organic monolayer films at gold using AFM under ambient laboratory conditions and reaffirms the presence of a $(\sqrt{3} \times \sqrt{3})R30°$ adlayer structure for alkanethiolate on Au(111). This and other recent findings suggest that AFM may prove valuable in providing detailed microscopic information for developing insights into interfacial structure-reactivity relationships. Both cohesive interactions between neighboring chains and the covalent linkage between the sulfur head group and gold surface have been identified as factors that play an important role in the ability to obtain these images. Experiments are in progress to evaluate further the capability of this technique to reveal the structure of various other monolayer films. We are particularly interested in developing further insights into the AFM imaging mechanism to facilitate a detailed comparison of our findings with those from He diffraction,[1] noting the possible complementary nature of the information supplied by the two methods. Extension to characterizations under thin layers of contacting liquids are also underway.

ACKNOWLEDGEMENTS

MDP gratefully acknowledges the support of a Dow Corning Assistant Professorship. We thank Dr. Vickie Hallmark for invaluable advice on the preparation of the mica-supported gold substrates, and Professors Cindra Widrig and Duane Weisshaar for helpful discussions. The synthesis of pentadecanethiol and tridecanethiol by Professor Chinkap Chung is appreciated. We thank Professor Allen Bard and Dr. Abraham Ulman for communicating their preliminary findings. Ames Laboratory is operated for the U.S. Department of Energy by Iowa State University under Contract No. W-7405-eng-82. This work was supported by the Office of Basic Energy Sciences, Chemical Science Division.

REFERENCES AND NOTES

1. Chidsey, C. E. D.; Liu, G.-Y.; Rowntree, P.; Scoles, G. *J. Chem. Phys.* **1989**, *91*, 4421-3.
2. (a) Strong, L.; Whitesides, G. M. *Langmuir* **1988**, *4*, 546-58.
   (b) For additional details: Chidsey, C. E. D.; Loiacono, D. M. *Langmuir* **1990**, *6*, 682-91.
3. Samant, M. G.; Brown, C. A.; Gordon, J. G. II *Langmuir* **1991**, *7*, 437-9.
4. Widrig, C. A.; Alves, C. A.; Porter, M. D. *J. Am. Chem. Soc.* **1991**, *113*, 2805-10.
5. The $(\sqrt{3} \times \sqrt{3})$R30° adlayer structure has also been observed for monolayers formed by the adsorption of 4-aminothiophenol at Au(111). Kim, Y.-T.; McCarley, R. L.; Bard, A. J., private communication.
6. Binnig, G.; Quate, C. F.; Gerber, Ch. *Phys. Rev. Lett.* **1986**, *56*, 930-3.
7. Binnig, G.; Rohrer, H. *Surf. Sci.* **1983**, *126*, 236-44.
8. See for example: a) Becker, R. S.; Swartzentruber, B. S.; Vickers, J. S. *J. Vac. Sci. Technol. A* **1988**, *6*, 472-7.
   b) Köhler, U.; Jusko, O.; Pietsch, G.; Müller, B.; Henzler, M. *Surf. Sci.* **1991**, *248*, 321-31.
   c) Whitman, L. J.; Stroscio, J. A.; Dragoset, R. A.; Celotta, R. J. *J. Vac. Sci. Technol. B* **1991**, *9*, 770-4.
   d) Chang, H.; Bard, A. J.; *J. Am. Chem. Soc.* **1991**, *113*, 5588-96.

9. See for example: a) Manne, S.; Butt, H. J.; Gould, S. A. C.; Hansma, P. K. *Appl. Phys. Lett.* **1990**, *56*, 1758-9.

b) Manne, S.; Hansma, P. K.; Massie, J.; Elings, V. B.; Gewirth, A. A. *Science* **1991**, *251*, 183-6.

c) Weisenhorn, A. L.; Henriksen, P. N.; Chu, H. T.; Ramsier, R. D.; Reneker, D. H. *J. Vac. Sci. Technol. B* **1991**, *9*, 1333-5.

d) Hallmark, V. M.; Chiang, S.; Rabolt, J. F.; Swalen, J. D.; Wilson, R. J. *Phys. Rev. Lett.* **1987**, *59*, 2879-82.

e) Emch, R.; Nogami, J.; Dovek, M. M.; Lang, C. A.; Quate, C. F. *J. Appl . Phys* . **1989**, *65*, 79-84.

f) Yau, S.-L.; Gao, X.; Chang, S.-C.; Schardt, B. C.; Weaver, M. J. *J. Am. Chem. Soc.* **1991**, *113*, 6049-56

g) Schardt, B. C.; Yau, S.-L.; Rinaldi, F. *Science* **1989**, *243*, 1050-3.

h) Ogletree, D. F.; Hwang, R. Q.; Zeglinski, D. M.; Vazquez-de-Parga, A. L.; Somorjai, G. A.; Salmeron, M. *J. Vac. Sci. Technol. B* **1991**, *9*, 886-90.

i) Magnussen, O. M.; Hotlos, J.; Beitel, G.; Kolb, D. M.; Behm, R. J. *J. Vac. Sci. Technol. B* **1991**, *9*, 969-75.

10. See for example: a) Meyer, E.; Howald, L.; Overney, R. M.; Heinzelmann, H.; Frommer, J.; Güntherodt, H.-J.; Wagner, T.; Schier, H.; Roth, S. *Nature* **1991**, *349*, 398-400.

b) Drake, B.; Prater, C. B.; Weisenhorn, A. L.; Gould, S. A. C.; Albrecht, T. R.; Quate, C. F.; Cannell, D. S.; Hansma, H. G.; Hansma, P.K. *Science* **1989**, *243*, 1586-9.

c) Mate, C. M.; Lorenz, M. R.; Novotny, V. J. *J. Chem. Phys.* **1989**, *90*, 7550-5.

d) Smith, D. P. E.; Hörber, J. K. H.; Binnig, G.; Nejoh, H. *Nature* **1990**, *344*, 641-4.

e) Ohtani, H.; Wilson, R. J.; Chiang, S.; Mate, C. M. *Phys. Rev. Lett.* **1988**, *60*, 2398-2401.

f) Hallmark, V. M.; Chiang, S.; Wöll, Ch. *J. Vac. Sci. Technol. B* **1991**, *9*, 1111-4.

g) Magonov, S. N.; Kempf, S.; Rotter, H.; Cantow, H.-J. *Synth. Met.* **1991**, *40*, 73-86.

11. See for example: a) Weisenhorn, A. L.; Egger, M.; Ohnesorge, F.; Gould, S. A. C.; Heyn, S.-P.; Hansma, H. G.; Sinsheimer, R. L.; Gaub, H. E.; Hansma, P. K. *Langmuir* **1991**, *7*, 8-12

b) Lin, J. N.; Drake, B.; Lea, A. S.; Hansma, P. K.; Andrade, J. D. *Langmuir* **1990**, *6*, 509-11.

c) Egger, M.; Ohnesorge, F; Weisenhorn, A. L.; Heyn, S. P.; Drake, B.; Prater, C. B.; Gould, S. A. C.; Hansma, P. K.; Gaub, H. E. *J. Struct. Biol* **1990**, *103*, 89-94.

d) Gould, S. A. C.; Drake, B.; Prater, C. B.; Weisenhorn, A. L.; Manne, S.; Hansma, H. G.; Hansma, P. K.; Massie, J.; Longmire, M.; Elings, V.; Northern, B. D.; Mukergee, B.; Peterson, C. M.; Stoeckenius, W.; Albrecht, T. R.; Quate, C. F. *J. Vac. Sci. Technol. A* **1990**, *8*, 369-73.

e) Beebe, T. P. Jr.; Wilson, T. E.; Ogletree, D. F.; Katz, J. E.; Balhorn, R.; Salmeron, M. B.; Siekhaus, W. J. *Science* **1989**, *243*, 370-2.

f) Salmeron, M.; Beebe, T.; Odriozola, J.; Wilson, T.; Ogletree, D. F.; Siekhaus, W.; *J. Vac. Sci. Technol. A.* **1990**, *8*, 635-41.

12. Evidence that these monolayers form as the corresponding thiolates at Au, is given in: a) Widrig, C. A.; Chung, C.; Porter, M. D. *J. Electroanal. Chem.* **1991**, *310*, 335-59; b) Raman studies confirm the absence of a S-H linkage (Bryant , M. A.; Pemberton, J. E. *J. Am. Chem. Soc.*, submitted.);

c) Bain, C. D.; Biebuyck, H. A.; Whitesides, G. M. *Langmuir* **1989**, *5*, 723-7.

13. a) Whitesides, G. M.; Laibinis, P. E. *Langmuir* **1990** *6*, 87-96.

b) Nuzzo, R. G.; Dubois, L. H.; Allara, D. L. *J. Am. Chem. Soc.* **1990**, *112*, 558-69.

c) Dubois, L. H.; Zegarski, B. R.; Nuzzo, R. G. *J. Am. Chem. Soc.* **1990**, *112*, 570-9.

14. a) Porter, M. D.; Bright, T. B.; Allara, D. L.; Chidsey, C. E. D. *J. Am. Chem. Soc.* **1987**, *109*, 3559-69.

b) Li, T. T.-T.; Weaver, M. J. *J. Am. Chem. Soc.* **1984**, *106*, 6107-8.

c) Sabatani, E.; Rubinstein, I. *J. Phys. Chem.* **1987**, *91*, 6663-9.

d) Finklea, H. O.; Snider, D. A.; Fedyk J. *Langmuir* **1990**, *6*, 371-6.

e) De Long, H. C.; Buttry, D. A. *Langmuir* **1990**, *6*, 1319-22.

f) Chidsey, C. E. D. *Science* **1991**, *251*, 919-22.

g) Creager, S. E.; Rowe, G. K. *Anal. Chim. Acta*, **1991**, *246*, 233-9.

h) Tarlov, M. J.; Bowden, E. F. *J. Am. Chem. Soc.* **1991,** *113,* 1847-9.

15. Blackman, G. S.; Mate, C. M.; Philpott, M. R. *Phys. Rev. Lett.* **1990,** *65,* 2270-3.

16. Burnham, N. A.; Dominguez, D. D.; Mowery, R. L.; Colton, R. J. *Phys. Rev. Lett.* **1990,** *64,* 1931-4.

17. Novotny, V.; Swalen, J. D.; Rabe, J. P. *Langmuir* **1989,** *5,* 485-9.

18. a). Nuzzo, R. G.; Zegarski, B. R.; Dubois, L. H. *J. Am. Chem. Soc.* **1987,** *109,* 733-40.

b) Ulman, A.; Eilers, J. E.; Tillman, N. *Langmuir* **1989,** *5,* 1147-52.

c) Bain, C. D.; Troughton, E. B.; Tao, Y.-T.; Evall, J.; Whitesides, G. M.; Nuzzo, R. G. *J. Am. Chem. Soc.* **1989,** *111,* 321-35.

d) Nuzzo, R. G.; Korenic, E. M.; Dubois, L. H. *J. Chem. Phys.* **1989,** *93,* 767-73.

e) Nuzzo, R. G.; Allara, D. L. *J. Am. Chem. Soc.* **1983,** *105,* 4481-3.

f) Evans, S. D.; Urankar, E.; Ulman, A.; Ferris, N. *J. Am. Chem. Soc.* **1991,** *113,* 4121-31.

19. Walczak, M. M.; Popenoe, D. D.; Deinhammer, R. S.; Lamp, B. D.; Chung, C.; Porter, M. D. *Langmuir,* accepted.

20. The electrochemically determined area is based on measurements of the oxidative desorption of iodine. (Rodriguez, J. F.; Mebrahtu, T.; Soriaga , M. P. *J. Electroanal. Chem.* **1987,** *233,* 283-9).

21. Walczak, M. M.; Alves, C. A.; Deinhammer, R. S.; Lamp, B. D.; Chung, C.; Porter, M. D., in preparation.

22. a) Schultze, J. W.; Dickertmann, D. *Surf. Sci.* **1976,** *54,* 489-505.

b) Engelsmann, K.; Lorenz, W. J.; Schmidt, E. *J. Electroanal. Chem.* **1980,** *114,* 1- 10.

23. Chidsey, C. E. D.; Loiacono, D. M.; Sleator, T.; Nakahara, S. *Surf. Sci.* **1988,** *200,* 45-66.

24. Golan, Y.; Margulis, L.; Rubinstein, I. *Surf. Sci,* submitted.

25. For an overview of the spatial and conformation arrangement of these monolayers, see reference 13a,b and 14a. Detailed discussions on temperature effects can be found in references 1 and 18d. Recent molecular dynamics simulations (Hautman, J.; Klein, M. *J. Chem. Phys* . **1990,** *93,* 7483-92) have also revealed the accumulation of thermally-activated conformational disorder at the chain terminus.

26. Kittel, C. *Introduction to Solid State Physics,* 5 ed. (Wiley, New York, 1976).

27. The slight distortion in the image is attributed to thermally-induced drift.

28. The distances labeled in Scheme I indicate the nearest- and next-nearest-neighbor spacings (a and b, respectively) of 0.50 nm and 0.87 nm, respectively, for an adsorbate forming a $(\sqrt{3} \times \sqrt{3})R30°$ adlayer on Au(111). Assuming each adsorbate binds at an equivalent site, identical $(\sqrt{3} \times \sqrt{3})R30°$ overlayer structures can be constructed at the three-fold hollow sites, two-fold bridging sites, or on-top sites. The three-fold hollow sites are the most likely candidates as suggested by: a) reference 2a; b) Ogletree, D. F.; Ocal, C.; Marchon, B.; Somorjai, G. A.; Salmeron, M.; Beebe, T.; Siekhaus, W. *J. Vac. Sci. Technol. A*

1990, *8*, 297-301. Recent ab initio calculations also point to the three-fold hollows as the preferred site (A. Ulman, Eastman Kodak Co., private communication).

29. Walczak, M. M.; Chung, C.; Stole, S. M.; Widrig, C. A.; Porter, M. D. *J. Am. Chem. Soc.* **1991**, *113*, 2370-8.

30. Persson, B. N. *J. Chem. Phys. Lett.* **1987**, *141*, 366-8.

31. This contention is further supported by recent electrochemical measurements of surface coverage (references 12 and 19). These studies found that the surface coverage of alkanethiolate monolayers at Au(111) is constant from n=2-17. We also note that the measured coverage of $8.4 \pm 0.7 \times 10^{-10}$ moles/cm^2 compares reasonably well with the 7.6×10^{-10} moles/cm^2 coverage expected for a $(\sqrt{3} \times \sqrt{3})R30°$ adlayer on Au(111).

PAPER 3. THIOLATE MONOLAYERS AT GOLD WITH A FLUOROCARBON TAIL: MICROSTRUCTURAL AND MACROSTRUCTURAL DESCRIPTIONS FROM ATOMIC FORCE MICROSCOPY, ELECTROCHEMISTRY, AND INFRARED REFLECTION SPECTROSCOPY

ABSTRACT

Monolayer films formed by the chemisorption of $CF_3(CF_2)_7(CH_2)_2SH$ (FT) at epitaxially grown Au(111) films were examined using atomic force microscopy (AFM), electrochemistry, and infrared reflection spectroscopy (IRS). The AFM images exhibit a periodic hexagonal pattern with average nearest- and next-nearest-neighbor distances of 0.58 ± 0.02 nm and 1.0 ± 0.02, respectively. A packing model for such an arrangement is a (2 x 2) adlayer structure at Au(111). The surface coverage of the monolayer, as determined by the electrochemical reductive desorption of the monolayer from the Au substrate is $(6.3 \pm 0.8) \times 10^{-10}$ mol/cm^2, a value consistent with the 0.25 monolayer coverage expected for a (2 x 2) structure. Evidence from IRS also supports the existence of the (2 x 2) adlayer structure as determined by AFM. The usefulness of AFM for determination of the structure of densely packed monolayers will be discussed as will the value of correlating the microscopic data from AFM with macroscopic descriptions.

INTRODUCTION

Scanning tunneling (STM)[1] and atomic force microscopies (AFM)[2] have become important techniques for the atomic-scale characterization of surfaces. Notable studies include the surface structure of semiconductor,[3-5] metallic,[6-8] electrochemical,[9-12] organic,[13-22] and biological,[23-27] interfaces. Both techniques have also proven valuable as probes of model organic monolayer films, such as those formed by Langmuir-Blodgett deposition[16,17,19-21] and by self-assembly.[13,14,27] A major goal of the latter efforts is the determination of the long- and short-range packing arrangements of the model monolayers that will serve as a basis for correlations with macroscopic interfacial properties (e.g. wettability,[28-30] electron-transfer,[31,32] and metal overlayer adhesion[33-35]).

We have been exploring the utility of STM and AFM for imaging monolayers formed by the self-assembly of various thiol-containing compounds at gold surfaces. Our earlier efforts[13,14] have demonstrated that both techniques can reveal details of the two-dimensional arrangement of *n*-alkanethiolate[36,37] monolayers formed at Au(111) epitaxially grown gold films at mica. In this report, we apply AFM to probe the atomic-scale structure of a different type of thiolate monolayer, namely that formed from $CF_3(CF_2)_7(CH_2)_2SH$ (abbrev. FT) at Au(111). Our interest in this type of monolayer stems from two primary sources. First, monolayers that contain a terminal perfluorocarbon chain may prove useful as models of the surface of fluorinated polymers.[15,31,38-40] Second, the FT monolayers will serve as an

important test case for further assessment of the atomic-scale imaging capabilities of AFM for ordered organic interfaces. The larger diameter (van der Waals diameter of 5.6 Å)[31] of the $CF_3(CF_2)_7$-tail should lead to a difference in the packing of the FT monolayers at Au(111) relative to the analogous alkanethiolate monolayers (van der Waals diameter of 4.2 Å).[41] Thus, a delineation of the two-dimensional arrangement of this adsorbate-substrate system is of fundamental importance.

In the following sections, we present the first atomic-level AFM images of monolayers formed by the adsorption of FT at Au(111). As discussed, a periodic image with a hexagonal packing arrangement consistent with that expected from a molecular model for densely packed perfluorocarbon chains is found. These images are compared with those obtained for monolayers formed from the analogous chain length *n*-alkanethiol (i.e.$CH_3(CH_2)_9SH$, abbrev. DT).[13] The difference in the ability to obtain atomically resolved images of the two different types of monolayers is also examined. In addition, we describe the results from characterizations using electrochemical measurements of surface coverage, and infrared reflection spectroscopy (IRS), techniques that provide a macrostructural description in agreement with that based on our interpretations of the AFM images.

EXPERIMENTAL

Monolayer and Gold Substrate Preparation.

Gold substrates with a predominantly (111) surface crystallinity were prepared by the resistive evaporation of 300 nm of gold onto freshly cleaved green mica sheets (Asheville-Schoonmaker, Newport News, VA), as previously described.[13,14] The roughness factor of the gold substrates, given as the electrochemically determined area divided by the geometric area, equals 1.1 ± 0.1,[42] this value was determined by the oxidative desorption of iodine.[43] At a microscopic level, the surfaces of the uncoated gold films are strongly (111) textured (>99%), based on comparisons of the voltammetric curves for the underpotential deposition of Pb(II) to literature data at single crystal gold electrodes.[44,45] Images from STM and AFM routinely exhibit the 0.29 nm interatomic spacing[46] of Au(111)[13,14] over areas as large as several hundred square nanometers. The above findings are in general agreement with the results of earlier bulk and surface[42,47] crystallinity results as well as earlier STM,[7,8] AFM,[48] and electron diffraction [49] studies.

The monolayers were prepared by chemisorption at gold from 1 mM ethanolic solutions of the thiols using previously described protocols.[32] Formation times were typically 2-4 hrs. Upon removal from solution, the samples were rinsed thoroughly with ethanol and dried in air. The wettabilities of both types of monolayers, using water and hexadecane as probe liquids for contact angle measurements, were comparable to those reported previously.[31,50]

Instrumentation.

AFM. Images were obtained in air using a Digital Instruments Nanoscope II (Santa Barbara, CA). The instrument was equipped with a 0.7 μm AFM scan head. After loading a sample, the instrument was allowed to come to thermal equilibrium, which required ~30 min. All images were collected in air with the AFM tip in contact with the sample in the constant force mode. In this mode, the force between the AFM tip and the sample surface is held constant, and the vertical displacements of the sample needed to maintain the preselected force are recorded as the surface rasters below the tip. Triangularly shaped silicon nitride cantilevers with pyramidal tips (Digital Instruments) were used. The force constant of the cantilevers was 0.58 N/m. Images were acquired at a rate of 14 to 28 lines/s, requiring roughly 15 to 25 s of collection time per image. Imaging forces were typically 50 nN. The horizontal displacement of the tip was calibrated using freshly cleaved mica. Images were smoothed with an eight-point moving-average algorithm (i.e. the low-pass filter utility of the Nanoscope II).

Electrochemical Measurements. Electrochemical experiments were performed in 0.5 M KOH solutions using a CV-27 potentiostat (Bioanalytical Systems), a Houston Instruments 2000 XY recorder, and a conventional three-electrode cell. The exposed area of the working electrode, as defined by the diameter of a Teflon O-ring, was 0.55 cm^2. All voltages are reported with respect to a Ag/AgCl/saturated KCl electrode.

Infrared Spectroscopy. Infrared spectra were acquired with a Nicolet 740 FT-IR interferometer. Monolayer spectra were obtained using p-

polarized light incident at 80° with respect to the surface normal and are reported as $-\log(R/R_0)$, where R is the reflectance of the sample and R_0 is the reflectance of a bare Au reference substrate. A home-built sample holder was used to position reproducibly the substrates in the spectrometer.[51] Transmission spectra were obtained by the dispersion of bulk FT in KBr. All spectra are the average of 1024 scans of both the sample and reference. All spectra were collected at 2 cm^{-1} resolution (zero-filled) with Happ-Genzel apodization. A liquid N_2 cooled HgCdTe detector was used. The spectrometer and sample chamber were both purged with boil-off from liquid N_2. Further details of the spectroscopy, and sample and reference handling, are given elsewhere.[52]

Orientational Analysis of the Monolayer. Spatial orientation of these monolayers develops from consideration of the infrared surface selection rule,[53] with the average tilts between transition dipole moments (m) and the surface normal (z) calculated from[54,55]

$$\cos^2\theta_{mz} = A_{obs}/\ 3(A_{calc}) \qquad (1)$$

where θ_{mz} is the angle of average tilt of a vibrational mode with respect to the surface normal, A_{obs} is the observed absorbance, and A_{calc} is the absorbance calculated for an isotropic collection of adsorbate precursors with comparable packing density. Therefore, relating the molecular axis of the carbon backbone to the transition dipole, the spatial orientation of the monolayer can be determined. Inputs into the electromagnetic

formulation[56] for the calculated spectra include the angle of incidence and polarization of incoming light, and the complex optical constant ($\hat{n}$) of each of the phases of the experimental system (i.e. air, monolayer, and Au substrate). The optical function for the monolayers was calculated from a Kramers-Kronig analysis of the IR spectrum of the adsorbate precursor dispersed in KBr. The optical function for Au was extrapolated from the literature.

Reagents.

Absolute ethanol (Quantum) and KOH (Aldrich, 99.99%) were used as received. Hexadecane (Aldrich, anhydrous, 99+%) was stored under N_2 and used as received. Decanethiol (Kodak) was passed through an alumina column prior to use. The fluorinated thiol ($CF_3(CF_2)_7(CH_2)_2SH$) was a gift from Dr. F. Behr (3M), and was used as received.

RESULTS AND DISCUSSION

The following sections present and discuss the results of a detailed characterization of the structure of the monolayer formed by the chemisorption of $CF_3(CF_2)_7(CH_2)_2SH$ at Au(111). Microscopic features are probed using AFM giving information on the spatial arrangement of the FT monolayer. A molecular model for the spatial arrangement of molecules for the FT monolayer is presented and compared to that for the *n*-alkanethiolates. Macroscopic features are probed by contact angle measurements, and infrared reflection spectroscopy; techniques that provide information related respectively to the wettability and spatial orientation of the layers.

Atomic Scale Characterization with AFM.

Images of FT and DT at Au(111). Figure 1 contains an AFM image of FT at Au(111). The image encompasses an area of 9 nm^2 and is given in a top-view presentation with a gray vertical scale. A hexagonal array of bright spots is observed. The topographical contour plots taken along the black lines overlaying the image, are shown in Figure 1B; the lines a and b represent the nearest-neighbor (nn) and next-nearest-neighbor (nnn) spacings, respectively. The respective average nn and nnn spacings are 0.58 ± 0.02 nm and 1.0 ± 0.02 nm. This arrangement has been observed for areas up to 100 nm^2.

Figure 1. (A) A 3.0 x 3.0 nm^2 AFM image of FT at Au(111). This image is unfiltered.

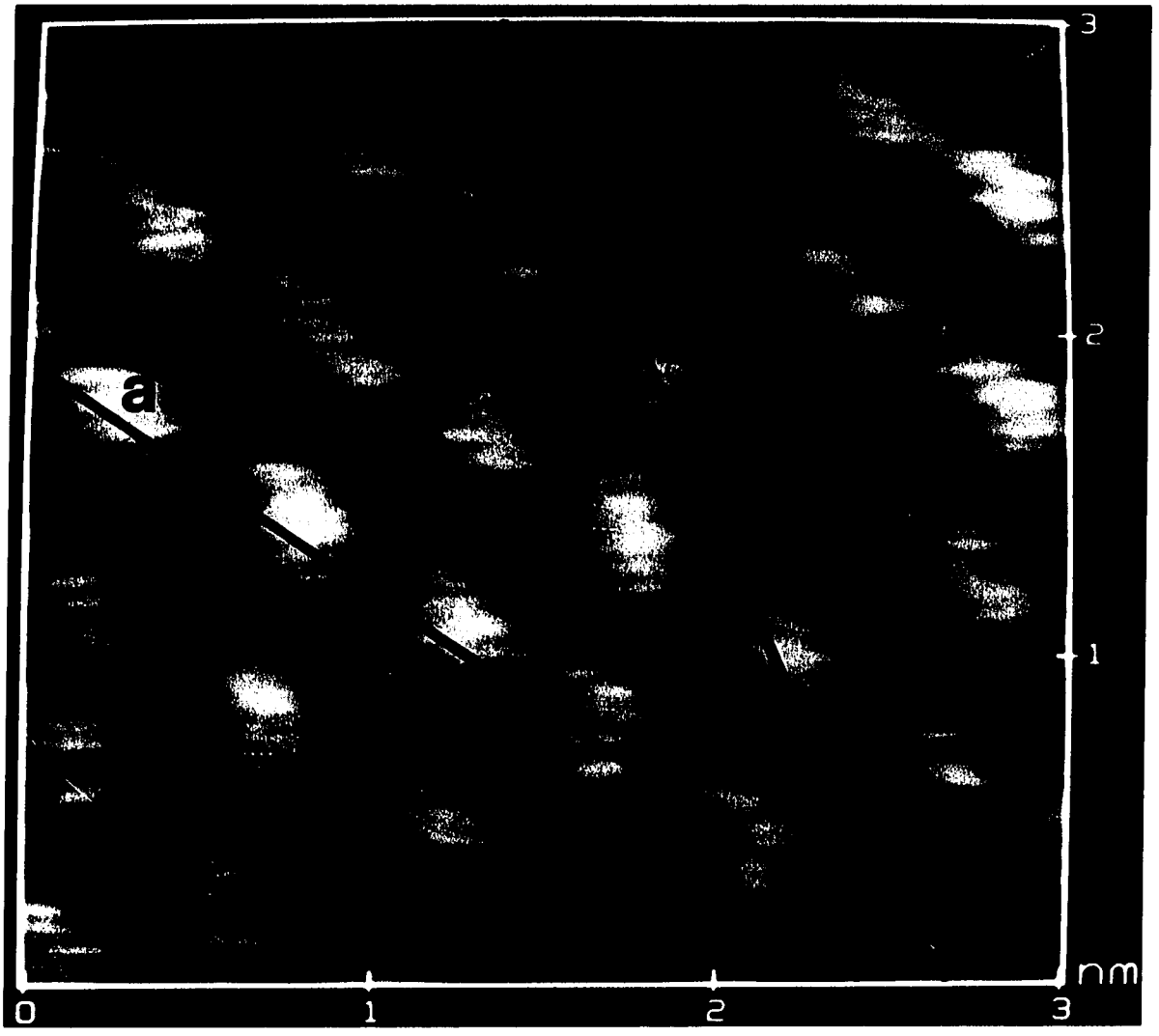
a
3
2
1
nm
0
1
2
3

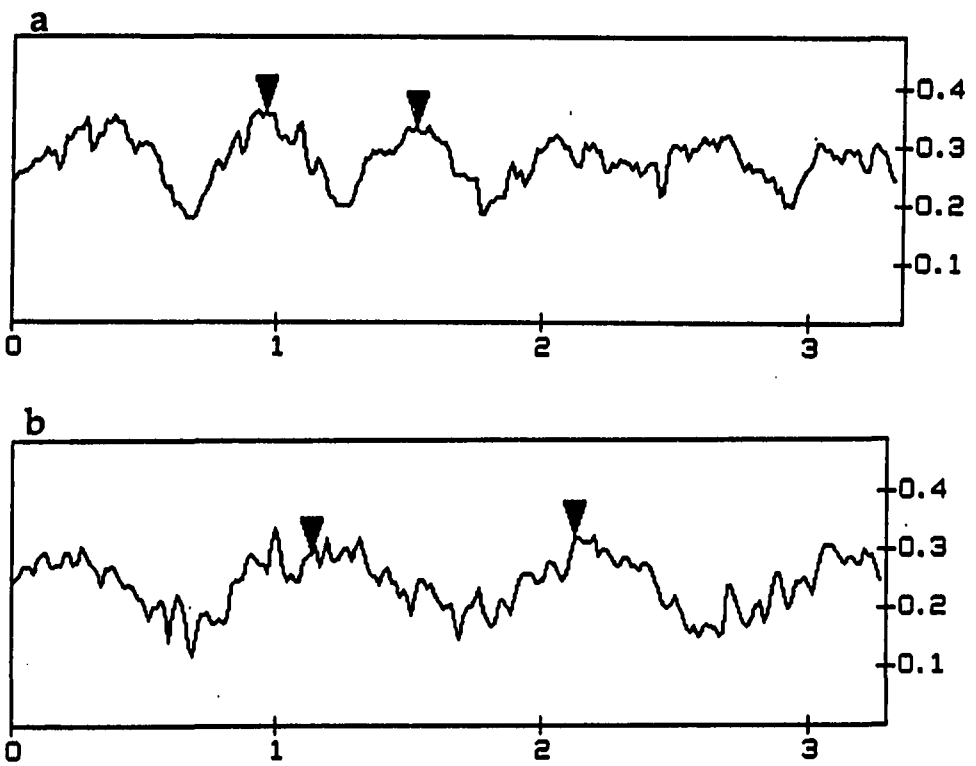

Figure 1 (cont'd). (B) The cross-sections indicated by lines (a) and (b) in Figure 1A. The line (a) shows the nearest-neighbor spacing of 0.57 nm and line (b) the next-nearest-neighbor spacing of 0.99 nm.

For comparison to Figure 1, Figure 2 contains the AFM image of DT at Au(111), the perhydrido analog FT at Au(111). The image of DT at Au(111) has been previously reported[13] and is used here for a necessary comparison. The image in Figure 2 also has a hexagonal periodicity and areas as large as 100 nm^2 have been observed.[13] However, as shown by the cross-sections in Figure 2B, the respective average values of 0.50 ± 0.03 nm and 0.90 ± 0.04 nm for the nn and nnn spacings are less than those for FT at Au(111). We have found comparable spacings for *n*-alkanethiolates having between 5 and 18 carbons in the alkane chain.[13] The spacings are, in both cases, larger than those of the 0.29 nm and 0.50 nm nn and nnn spacings found in images of the uncoated Au(111) substrate.[7,8,13,14,48]

Packing Models. As previously determined, the two-dimensional arrangement of DT is consistent with a $(\sqrt{3} \times \sqrt{3})R30°$ adlayer structure at Au(111);[13] an arrangement which has previously been suggested from such macroscopic techniques as electron[57] and helium[58] diffraction, electrochemical coverage data[36], etc. This arrangement is depicted in Figure 3a where the open circles represent the Au(111) lattice and the gray circles represent the thiolate molecules. The placement of the thiolate adsorbates at the three-fold hollow positions, although not evident from the AFM/STM data, is consistent with previous accord.[57,59] The arrangement of FT at Au(111) is different from that of DT at Au(111). Although hexagonal, the separation distances between neighboring adsorbates is greater. Figure 3b presents a reasonable arrangement for FT at Au(111) where the dark circles represent the FT molecules. This arrangement represents a (2 x 2) overlayer

Figure 2. (A) A 3.02 x 3.02 nm^2 AFM image of DT at Au(111). This image is lowpass filtered. The slight elongation of the spots is due to thermal drift.

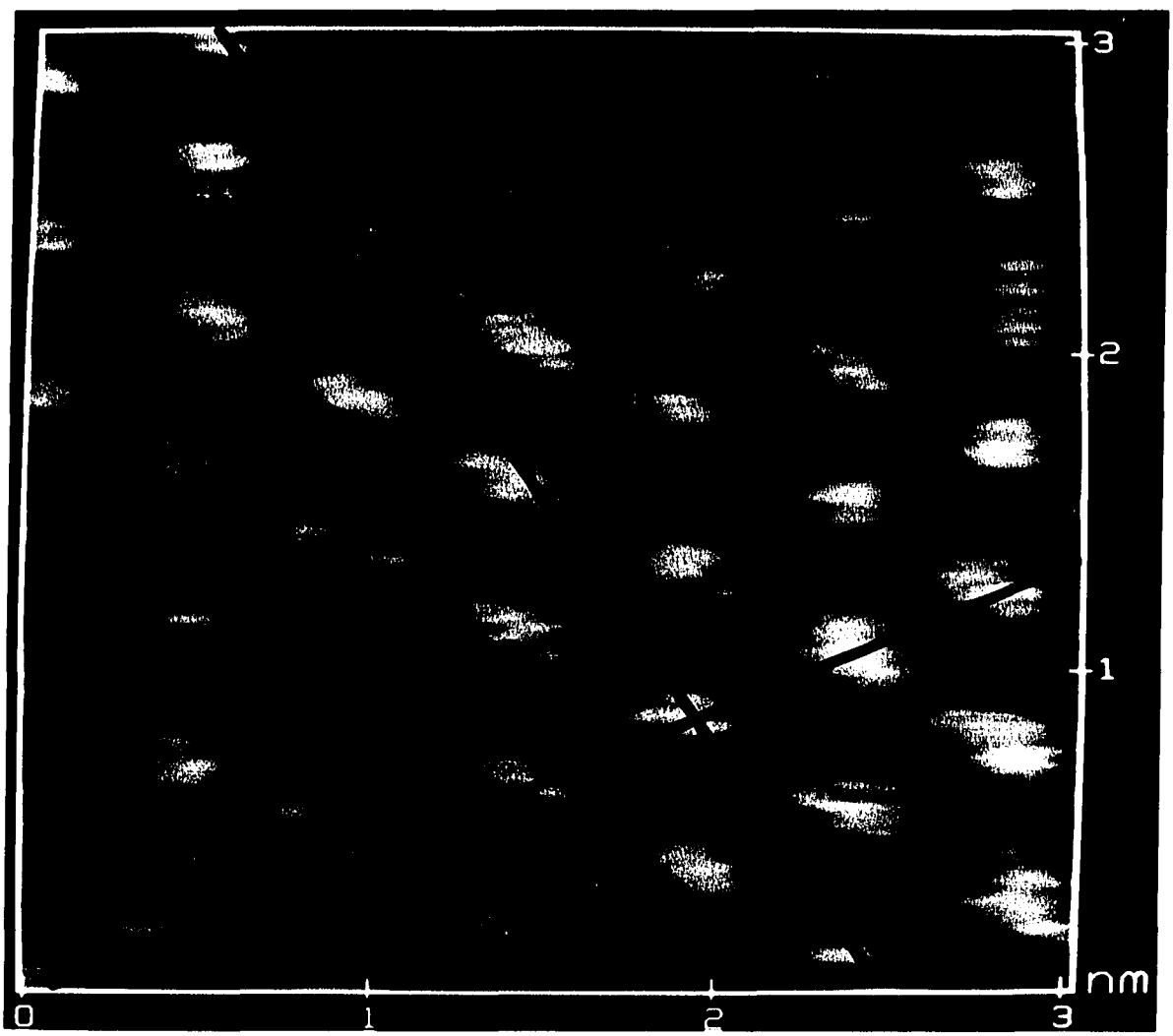
3
2
1
nm
0
1
2
3

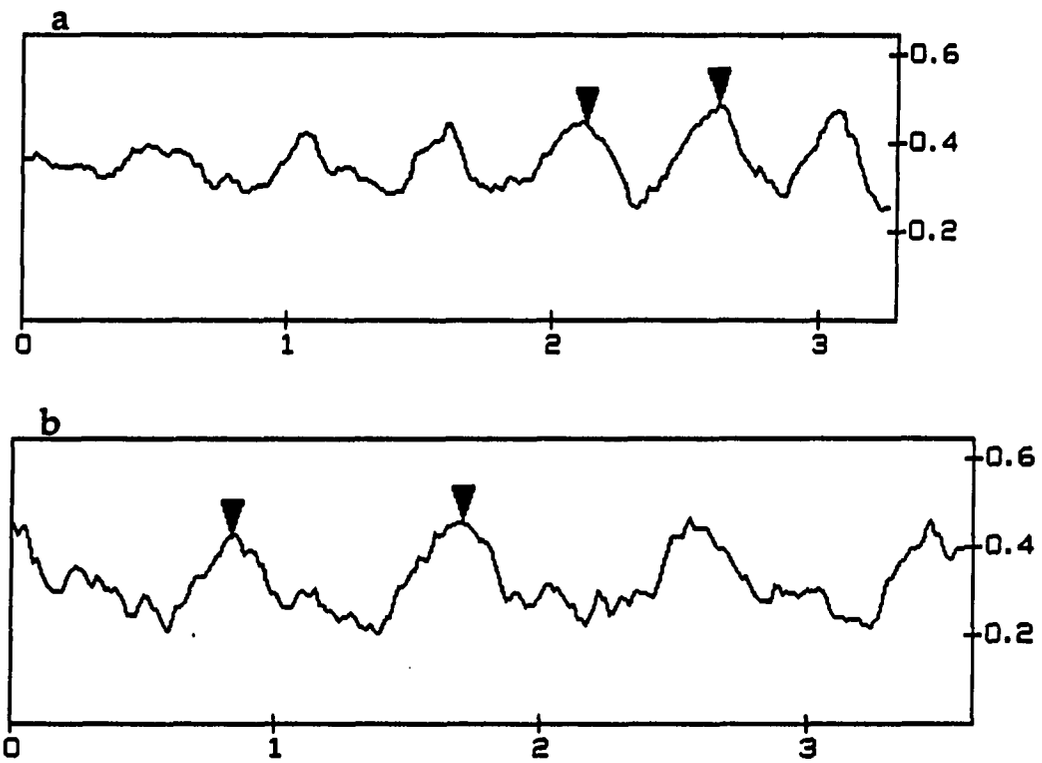

Figure 2 (cont'd). (B) The cross-sections indicated by lines (a) and (b) in Figure 2A. The line (a) shows the nearest-neighbor spacing of 0.50 nm and line (b) the next-nearest-neighbor spacing of 0.87 nm.

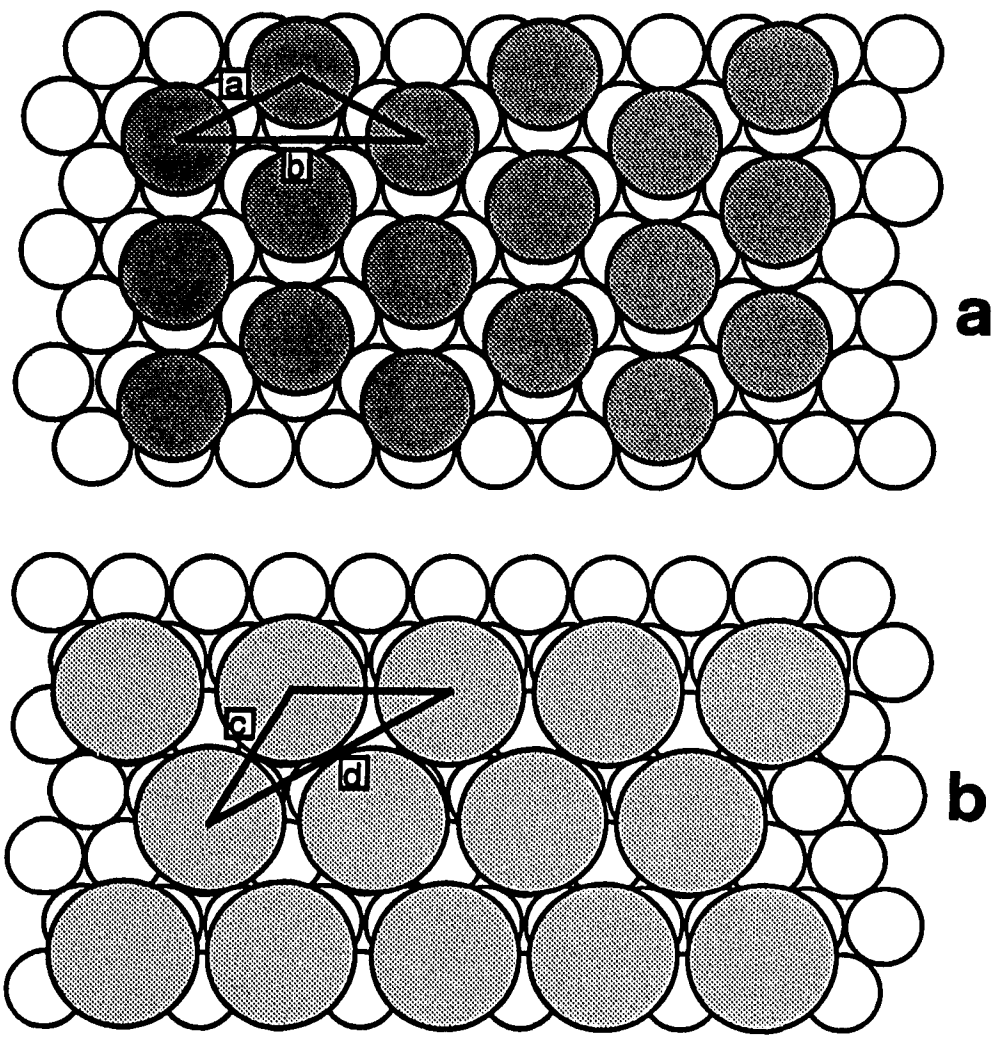

Figure 3. Schematic representations of the (a) $(\sqrt{3} \times \sqrt{3})R30°$ and the (b) (2 x 2) adlayer structures on Au(111). The open circles represent the Au atoms, the dark circles represent OT molecules, and the gray circles FT molecules. The expected spacings are a = 0.50 nm, b = 0.87 nm, c = 0.58 nm and d = 1.0 nm.

structure at Au(111) and has nn and nnn spacings of 0.58 nm and 1.0 nm, respectively. Importantly, the spacings in the model are consistent with those experimentally observed in the AFM images in Figure 1. Again, although not demonstrated by the AFM data, positioning of the adsorbates at the three-fold hollow sites is used in agreement with the alkanethiolate structure. From the spacing of the FT molecules and the van der Waals diameter of the fluorinated chains, a surface coverage of 5.7×10^{-10} mol/cm^2 is calculated at Au(111) (0.25 of a monolayer) and the expected tilt of the molecules relative to the surface normal is calculated to be ~15°. (The comparison of this tilt angle with that calculated using IR data is discussed below.) This is demonstrated in Figure 4a where the FT chains are represented by the rectangles and the angle θ is that from the surface normal to the carbon-carbon backbone. In comparison, the tilt for *n*-alkanethiolates at Au(111) as predicted by the $(\sqrt{3} \times \sqrt{3})R30°$ model is 33° as depicted in Figure 4b.

General Imaging Observations. It is uncertain what the exact position is of the tip relative to the end of the chain. We do expect that the tip is near the terminus of the fluorinated chain based primarily on comparison to the alkanethiolate.[13] As with the alkanethiolate monolayers, this ordered assembly of molecules can withstand the force of the tip (~50 nN) without destruction even though individual molecules have been calculated to withstand forces of only ~10^{-10} N.[60] Comparisons can be made between the ability to obtain images of the fluorinated vs. alkyl thiolate monolayers. Images of the fluorinated alkanethiolate monolayers are more

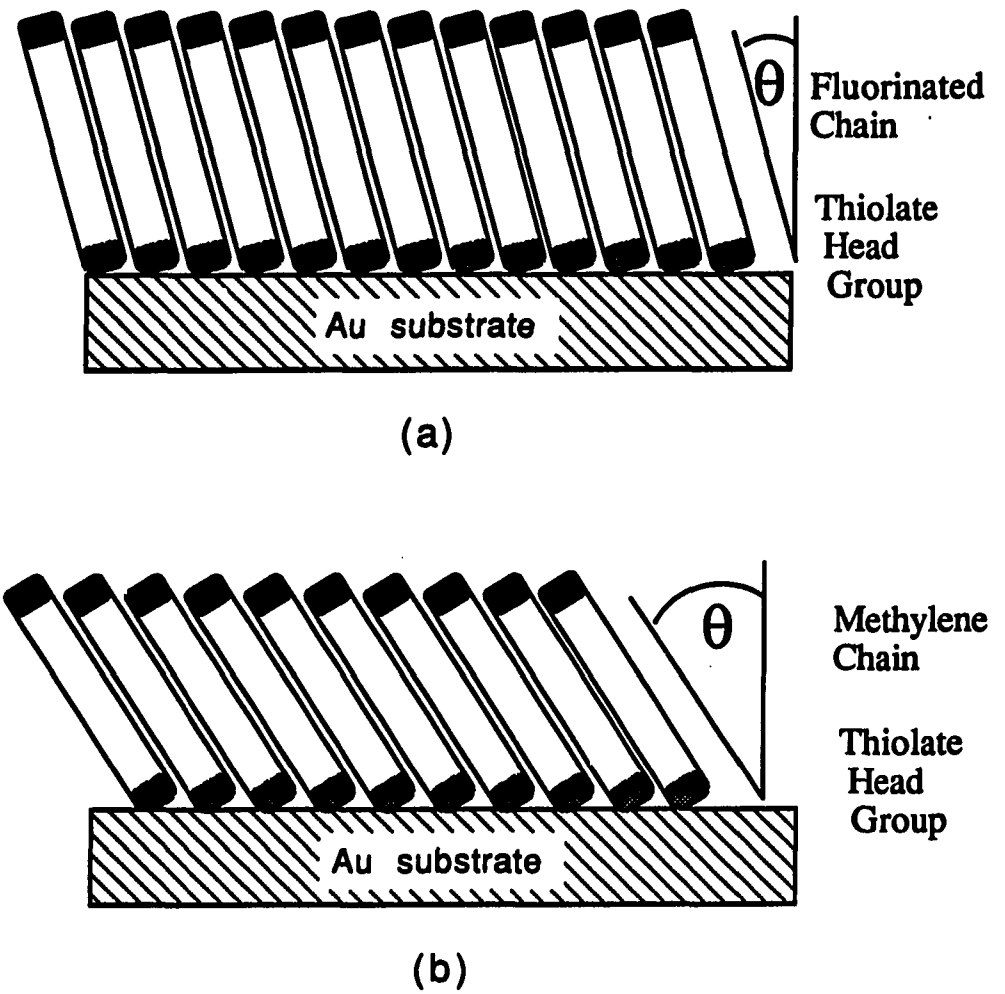

Figure 4. Schematic representation of thiolate monolayers tilted with respect to the surface normal. The fluorinated thiol (2 x 2) adlayer at Au(111) has an expected tilt of $\theta = 15^{\circ}$ as represented in (a). The expected tilt for the $(\sqrt{3} \times \sqrt{3})R30^{\circ}$ adlayer at Au(111) is 33° and represented in (b).

readily obtained using AFM than are the hydrocarbon analogs. This may be a result of the FT being less tilted with respect to the surface normal than the alkanethiolates (FT is tilted about 15° less then DT, see Figure 4) and less susceptible to compression[61] by the AFM tip during scanning. The FT also has a 15/7 helical conformation[62] versus the trans zig zag conformation of the *n*-alkanethiolates. Both properties of the FT monolayer would result in a more rigid system which is less susceptible to distortion (or induced rotation) from the AFM tip and more likely to produce ordered periodic AFM images. Examination of the FT monolayers at Au(111) using STM has been performed but has not yet been successful.

Electrochemical Characterization.

The electrochemical reductive desorption of FT from Au can be used as a means to determine surface coverage. This information can be compared to that from AFM. A cyclic voltammetric (CV) current-potential (i-E) curve for FT at Au(111) is shown in Figure 5. An i-E curve for uncoated Au(111) is included for comparison. Voltage scans were initiated at +0.2 V at a rate of 0.1 V/s and were reversed at the voltage limit imposed by solvent reduction. The supporting electrolyte was 0.5 M KOH. The large cathodic wave with a peak current near -1.05 V reflects the electrode reaction

$$\text{Au-SR} + 1e^- \rightarrow \text{RS}^- + \text{Au(0)}. \qquad (2)$$

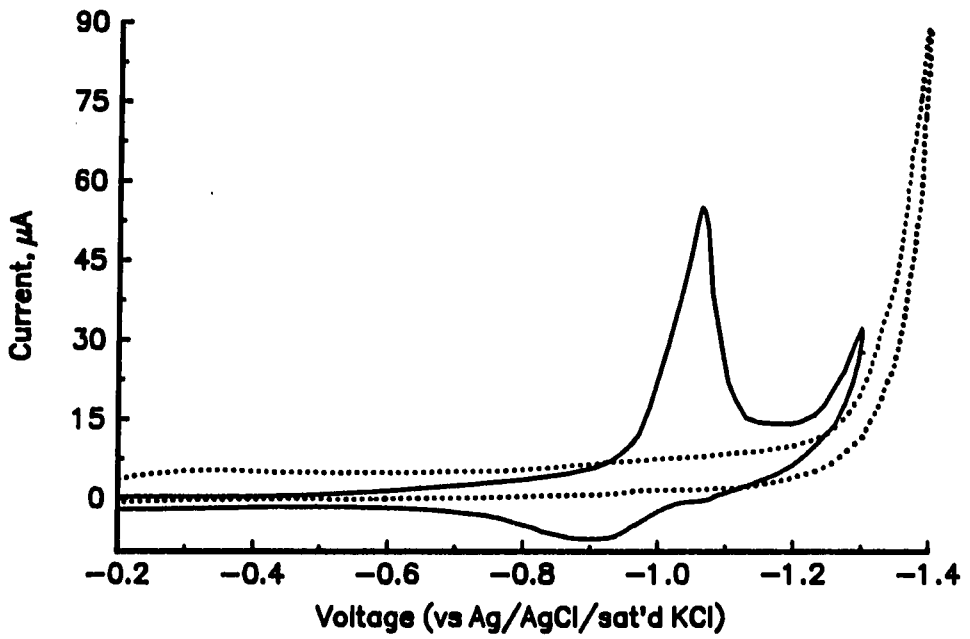

Figure 5. The i-E curve for the reductive desorption of FT (solid line) from Au(111). The i-E curve for uncoated Au(111) (dotted line) is shown for comparison. The scan rate is 0.1 V/s.

Earlier studies[36] show that thiolates desorb in alkaline solution via a one-electron reduction. The desorption voltage is comparable to that observed for alkanethiolate monolayers with an equivalent number of carbons, i.e. DT at Au(111).[63] The much smaller anodic wave found near -0.9 V upon scan reversal represents the reverse of the reaction in Equation (2), i.e. a one-electron oxidative deposition of the thiolate remaining in the diffusion layer after desorption. Details of the deposition reaction have recently appeared.[64]

From the CV i-E curve in Figure 5, the surface coverages (Γ) of thiolate monolayers at Au(111) can be determined using the electrode reaction given in Equation (2). The value of Γ is calculated as

$$\Gamma = Q/(nFA) \qquad (3)$$

where Q is the charge consumed in the reductive desorption reaction, n is the number of electrons involved in the electron-transfer process, and A is the geometric surface area of the electrode. The charge, Q, associated with the reductive desorption reaction for FT at Au(111) is determined by integrating the area under the cathodic wave after compensation for charging current. The value of Q was found to equal 33 ± 4 $\mu C/cm^2$ and is given as the average of determination of eight separate electrodes. Based on the reaction in Equation (2), Q then translates to a Γ of $(6.3 \pm 0.8) \times 10^{-10}$ mol/cm^2 for FT. This value, after accounting for the roughness of the underlying substrate (roughness factor of 1.1), correlates to a coverage of approximately 0.25 of a monolayer at Au(111), the same as expected for the (2 x 2) adlayer structure in

Figure 2b. By comparison, a Γ of $(9.3 \pm 0.6) \times 10^{-10}$ mol/cm^2 was determined for alkanethiolate at Au(111)[36], consistent with the 0.33 monolayer coverage of a $(\sqrt{3} \times \sqrt{3})$R30° adlayer at Au(111). These data support the interpretation of the AFM images.

Infrared Reflection Spectroscopic Characterization.

The composition and spatial orientation of FT at Au(111) was characterized using infrared reflection spectroscopy (IRS). Figure 6 presents the low energy spectral region (1800-1000 cm^{-1}) of the layer. Both observed (solid line) and calculated (dashed line) spectra are shown. Peak positions and tentative mode assignments are given in Table 1. As expected for a monolayer containing only two methylene groups, there are no observable features in the C-H stretching region (3000-2800 cm^{-1}) of the FT monolayer. This finding, along with the bands in the C-F stretching region (1400-1000 cm^{-1}), confirms the formation of the targeted monolayer.

The C-F stretching region exists at about 1400 cm^{-1} to 1000 cm^{-1}. Because of the complex nature of the IR spectrum for FT, a complete assessment of bands does not appear. The bands at 1372 cm^{-1} and 1335 cm^{-1} are attributed to the $\nu(CF_3)$. Bands at 1246 cm^{-1} and 1150 cm^{-1} are for $\nu(CF_2)$. Utilizing these $\nu(CF_2)$ modes which have dipole orientations parallel to the surface, a chain orientation can be determined based on the infrared surface selection rule. The average tilt between the transition dipole moments (m) and the surface normal (z) can be calculated from Equation (1).

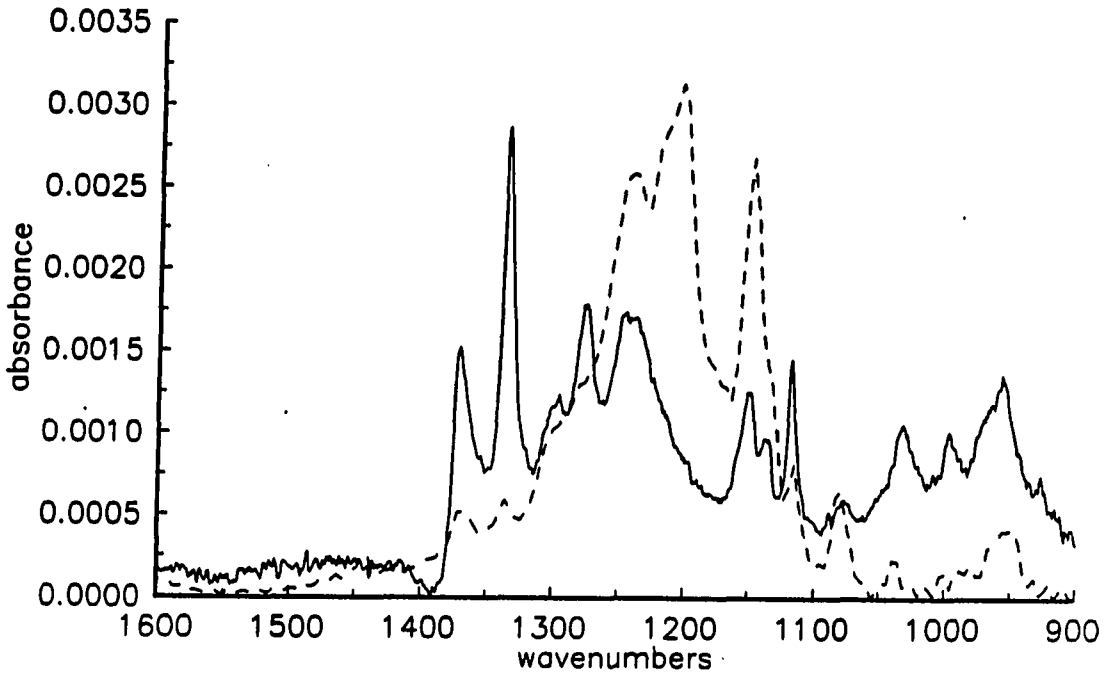

Figure 6. The experimental infrared reflection spectrum (solid line) of FT at Au(111), and the calculated spectrum (dashed line) for FT.

Table 1. IR band assignments for $C_8F_{17}(CH_2)_2SH$ at Au/mica

Peak Position (cm^{-1})	Assignment	Dipole Orientations
1372	$\upsilon(CF_3)$	
1335	$\upsilon(CF_3)$	
1295	$\upsilon(CC, E_1)$	
1276	$\upsilon_a(CF_2, E_1)$	$\perp$ to chain axis
1246	$\upsilon_a(CF_2, E)$	$\perp$ to chain axis
1150	$\upsilon_s(CF_2, E_1)$	$\perp$ to chain axis
1137		
1119		

Using the relationship in Equation (1), a tilt of ~23° was calculated for the FT chain with respect to the surface normal. This calculated tilt is reasonably close to the expected tilt for a (2 x 2) adlayer structure of FT at Au(111), 15°. The difference can be attributed to several factors. First, IR is a macroscopic technique and the spectrum is an average over a large area. Molecules near defects and step edges will have more freedom of movement and higher tilt angles. Secondly, the tilt calculation assumes that the FT molecules exhibit a nearly planar, trans zig-zag conformation. However, long fluorocarbon chains exhibit a 15/7 helical conformation above 19° C.

CONCLUSION

Using AFM, the two-dimensional arrangement of FT at Au(111) has been determined; a (2 x 2) adlayer structure. This result shows the difference in packing structure of the fluorinated versus alkane thiolates as predicted by the van der Waals diameter of the chains. Also, macroscopic measurements using electrochemistry and IRS indicate that the coverage of the monolayer and the tilt of the FT chain axis with respect to the surface normal are consistent with those predicted from the packing model obtained using AFM. Together, the microscopic and macroscopic details form a convincing picture of the packing structure. The AFM can be useful for determining packing arrangements of many densely packed organic assemblies. Future studies will focus on the determination of packing arrangements for less densely packed structures as well as determination of the AFM tip position and imaging mechanism.

ACKNOWLEDGMENTS

MDP gratefully acknowledges the support of a Dow Corning Assistant Professorship. CAA expresses appreciation for a Phillips Petroleum Fellowship. This research was partially sponsored by the Technology Laboratory of IBM Corporation. Ames Laboratory is operated for the U.S. Department of Energy by Iowa State University under Contract No. W-7405-eng-82. This work was supported by the Office of Basic Energy Sciences, Chemical Science Division.

REFERENCES AND NOTES

1. Binnig, G.; Rohrer, H. *Surf. Sci.* **1983**, *126*, 236-44.
2. Binnig, G.; Quate, C. F.; Gerber, C. *Phys. Rev. Lett.* **1986**, *56*, 930-3.
3. Biegelsen, D. K.; Bringans, R. D.; Northup, J. E.; Swartz, L. E. *Appl. Phys. Lett.* **1990**, *57*, 2419-2421.
4. Avouris, P.; Wolkow, R. *Phys. Rev. B* **1989**, *39*, 5091-5100.
5. Kim, Y.; Lieber, C. M. *J. Am. Chem. Soc.* **1991**, *113*, 2333-2335.
6. Weisenhorn, A. L.; Henriksen, P. N.; Chu, H. T.; Ramsier, R. D.; Reneker, D. H. *J. Vac. Sci. Technol. B* **1991**, *9*, 1333-1335.
7. Hallmark, V. M.; Chiang, S.; Rabolt, J. F.; Swalen, J. D.; Wilson, R. J. *Phys. Rev. Lett.* **1987**, *59*, 2879-82.
8. Emch, R.; Nogami, J.; Dovek, M. M.; Lang, C. A.; Quate, C. F. *J. Appl. Phys.* **1989**, *65*, 79-84.
9. Chen, C.-h.; Gewirth, A. A. *J. Am. Chem. Soc.* **1992**, *114*, 5439-5440.
10. Gao, X.; Hamelin, A.; Weaver, M. J. *J. Chem. Phys.* **1991**, *95*, 6993-6996.
11. Magnussen, O. M.; Hotlos, J.; Beitel, G.; Kolb, D. M.; Behm, R. J. *J. Vac. Sci. Technol. B* **1991**, *9*, 969-975.
12. Yau, S.-L.; Vitus, C. M.; Schardt, B. C. *J. Am. Chem. Soc.* **1990**, *112*, 3677-3679.
13. Alves, C. A.; Smith, E. L.; Porter, M. D. *J. Am. Chem. Soc.* **1992**, *114*, 1222-7.
14. Widrig, C. A.; Alves, C. A.; Porter, M. D. *J. Am. Chem. Soc.* **1991**, *113*, 2805-10.

15. Mate, C. M.; Lorenz, M. R.; Novotny, V. J. *J. Chem. Phys.* **1989**, *90*, 7550-7555.

16. Bourdieu, L.; Silberzan, P.; Chatenay, D. *Phys. Rev. Lett.* **1991**, *67*, 2029-2032.

17. Lang, C. A.; Horber, J. K. H.; Hansch, T. W.; Heckl, W. M.; Mohwald, H. *J. Vac. Sci. Technol. A* **1988**, *6*, 368-370.

18. Hallmark, V. M.; Chiang, S.; Brown, J. K.; Woll, C. *Phys. Rev. Lett.* **1991**, *66*, 48-51.

19. Smith, D. P. E.; Bryant, A.; Quate, C. F.; Rabe, J. P.; Gerber, C.; Swalen, J. D. *Proc. Natl. Acad. Sci. USA* **1987**, *84*, 969-972.

20. Weisenhorn, A. L.; Egger, M.; Ohnesorge, F.; Gould, S. A. C.; Heyn, S.-P.; Hansma, H. G.; Sinsheimer, R. L.; Gaub, H. E.; Hansma, P. K. *Langmuir* **1991**, *7*, 8-12.

21. Meyer, E.; Howald, L.; Overney, R. M.; Heinzelmann, H.; Frommer, J.; Guntherodt, H.-J.; Wagner, T.; Schier, H.; Roth, S. *Nature* **1991**, *349*, 398-400.

22. Drake, B.; Prater, C. B.; Weisenhorn, A. L.; Gould, S. A. C.; Albrecht, T. R.; Quate, C. F.; Cannell, D. S.; Hansma, H. G.; Hansma, P. K. *Science* **1989**, *243*, 1586-1589.

23. Miles, M. J.; McMaster, T.; Carr, H. J.; Tatham, A. S.; Shewry, P. R.; Field, J. M.; Belton, P. S.; Jeenes, D.; Hanley, B.; Whittam, M.; Cairns, P.; Morris, V. J.; Lambert, N. *J. Vac. Sci. Technol. A* **1990**, *8*, 698-702.

24. Egger, M.; Ohnesorge, F.; Weisenhorn, A. L.; Heyn, S. P.; Drake, B.; Prater, C. B.; Gould, S. A. C.; Hansma, P. K.; Gaub, H. E. *J. Struct. Biol.* **1990**, *103*, 89-94.

25. Bustamante, C.; Vesenka, J.; Tang, C. L.; Rees, W.; Guthold, M.; Keller, R. *Biochemistry* **1992**, *31*,

26. Beebe, T. P. J.; Wilson, T. E.; Ogletree, D. F.; Katz, J. E.; Balhorn, R.; Salmeron, M. B.; Siekhaus, W. J. *Science* **1989**, *243*, 370-372.

27. Haussling, L.; Michel, B.; Ringsdorf, H.; Rohrer, H. *Angew. Chem. Int. Ed. Engl.* **1991**, *30*, 569-572.

28. Whitesides, G. M.; Laibinis, P. E. *Langmuir* **1990**, *6*, 87-96 and references therein.

29. Nuzzo, R. G.; Dubois, L. H.; Allara, D. L. *J. Am. Chem. Soc.* **1990**, *112*, 558-69.

30. Dubois, L. H.; Zegarski, B. R.; Nuzzo, R. G. *J. Am. Chem. Soc.* **1990**, *112*, 570-9.

31. Chidsey, C. E. D.; Loiacano, D. N. *Langmuir* **1990**, *6*, 682-91.

32. Porter, M. D.; Bright, T. B.; Allara, D. L.; Chidsey, C. E. D. *J. Am. Chem. Soc.* **1987**, *109*, 3559-68.

33. Smith, E. L.; Alves, C. A.; Anderegg, J. W.; Porter, M. D.; Siperko, L. M. *Langmuir* **1992**, in press.

34. Czanderna, A. W.; King, D. E.; Spaulding, D. *J. Vac. Sci. Technol. A* **1991**, *9*, 2607-13.

35. Mittal, K. L. *J. Vac. Sci. Technol.* **1976**, *A7*, 1-20.

36. Widrig, C. A.; Chung, C.; Porter, M. D. *J. Electroanal. Chem.* **1991**, *310*, 335-59.

37. Bryant, M. A.; Pemberton, J. E. *J. Am. Chem. Soc.* **1991**, *113*, 8284-93.

38. Chau, L.-K.; Porter, M. D. *Chem. Phys. Letters* **1990**, *167*, 198-204.

39. Chau, L. K.; Porter, M. D. *Mat. Res. Soc. Symp. Proc.* **1989**, *153*, 267-272.

40. Naselli, C.; Swalen, J. D.; Rabolt, J. F. *J. Chem. Phys.* **1989**, *90*, 3855-3860.

41. Ulman, A.; Eilers, J. E.; Tillman, N. *Langmuir* **1989**, *5*, 1147-1152.

42. Walczak, M. M.; Alves, C. A.; Lamp, B. D.; Deinhammer, R. S.; Porter, M. D. **1992**, in preparation.

43. Rodriguez, J. F.; Mebrahtu, T.; Soriaga, M. P. *J. Electroanal. Chem.* **1987**, *233*, 283-9.

44. Schultze, J. W.; Dickertmann, D. *Surf. Sci.* **1976**, *54*, 489-505.

45. Engelsmann, K.; Lorenz, W. J.; Schmidt, E. *J. Electroanal. Chem.* **1980**, *114*, 1-10.

46. Kittel, C. *Introduction to Solid State Physics;* 5 ed.; Wiley: New York, 1976.

47. Golan, Y.; Margulis, L.; Rubinstein, I. *Surf. Sci.* **1992**, submitted.

48. Manne, S.; Butt, H. J.; Gould, S. A. C.; Hansma, P. K. *Appl. Phys. Lett.* **1990**, *56*, 1758-59.

49. Chidsey, C. E. D.; Loiacono, D. N.; Sleator, T.; Nakahara, S. *Surf. Sci.* **1988**, *200*, 45-66.

50. Bain, C. D.; Troughton, E. B.; Tao, Y.-T.; Evall, J.; Whitesides, G. M.; Nuzzo, R. G. *J. Am. Chem. Soc.* **1989**, *111*, 321-35.

51. Stole, S. M.; Porter, M. D. *Appl. Spectrosc.* **1990**, *49*, 1418-20.

52. Walczak, M. M.; Chung, C.; Stole, S. M.; Widrig, C. A.; Porter, M. D. *J. Am. Chem. Soc* **1991**, *113*, 2370-8.

53. Greenler, R. G. *J. Chem. Phys.* **1966**, *44*, 310-315.

54. Allara, D. L.; Nuzzo, R. G. *Langmuir* **1985**, *1*, 52-66.

55. Wilson, E. B., Jr.; Decius, J. C.; Cross, P. C. *Molecular Vibrations*; McGraw-Hill: New York, 1955, pp 285-6.

56. Hansen, W. N. *J. Opt. Soc. Am.* **1968**, *58*, 380-390.

57. Strong, L.; Whitesides, G. M. *Langmuir* **1988**, *4*, 546-58.

58. Chidsey, C. E. D.; Liu, G.-Y.; Rowntree, P.; Scoles, G. *J. Chem. Phys.* **1989**, *91*, 4421-3.

59. Ogletree, D. F.; Ocal, C.; Marchon, B.; Somorjai, G. A.; Salmeron, M.; Beebe, T.; Siekhaus, W. *J. Vac. Sci. Technol. A* **1990**, *8*, 297-301.

60. Persson, B. N. *J. Chem. Phys. Lett.* **1987**, *141*, 366-8.

61. Eaton, D. F.; Smart, B. E. *J. Am. Chem. Soc.* **1990**, *112*, 2821-2823.

62. Clark, E. S.; Muus, L. T. *Z. Krist.* **1962**, *117*, 119.

63. In contrast to the -1.05 V desorption voltage (E_p) for FT at Au(111), E_p for DT at Au(111) is -1.0 V vs Ag/AgCl (sat'd KCl). The uncertainties in E_p for the two different layers, coupled with the small differences in dielectric constants (2.26 for polyethylene and 2.1 for polytetrafluoroethylene) precludes the development of a distinct double layer model for FT at Au(111).

64. Weisshaar, D. E.; Lamp, B. D.; Porter, M. D. *J. Am. Chem. Soc.* **1992**, in press.

PAPER 4. SCANNING TUNNELING MICROSCOPIC AND ELECTROCHEMICAL EVIDENCE FOR THE OXIDATION OF ALKANETHIOLATE MONOLAYERS AT AU(111) UPON PROLONGED EXPOSURE TO AIR

ABSTRACT

Octadecanethiolate (OT) monolayers at Au(111) films on mica were studied as a function of exposure to laboratory ambient using scanning tunneling microscopy (STM) and electrochemical reductive desorption. At short exposure times (<2 days), the expected $(\sqrt{3} \times \sqrt{3})R30°$ structure was observed. However, upon prolonged exposure to air, evidence for the oxidation of the monolayer was obtained. The longer the exposure to air, the more likely the observation of an oxidized species of sulfur. Images from STM show evidence for a closed ring structure with dimensions similar to those of a cyclooctasulfur (cyclo-S_8) molecule. The electrochemical reductive desorption experiments indicate the appearance of a second species on the thiolate-coated Au substrate with desorption potentials similar to that of cyclo-S_8. Thus, the oxidation product has been identified as cyclo-S_8. The observation of structures other than the $(\sqrt{3} \times \sqrt{3})R30°$ and cyclo-S_8 structures seem to indicate the presence of other allotropes of sulfur on the surface as oxidation products of the thiolate decomposition.

INTRODUCTION

In recent reports, we have demonstrated the capability of imaging at an atomic-level alkanethiolate monolayers formed at Au(111)[1] ($CH_3(CH_2)_nS$-Au) using scanning tunneling (STM)[2] and atomic force (AFM)[3] microscopies. Similar findings[4] along with those obtained using various macroscopic probes (e.g. infrared reflection[5] and Raman[6] spectroscopies, and diffraction t
echniques,[7-10] and electrochemical measurements of surface coverage[11]), support the presence of a $(\sqrt{3} \times \sqrt{3})R30°$ alkanethiolate adlayer as the dominant structure at a Au(111) surface.

In this paper, we report on the observation of images that point to the presence of at least one other type of surface structure for these layers on Au. We have identified this species as elemental sulfur in the form of cyclooctasulfur (abbrev. cyclo-S_8). The presence of this species on alkanethiolate-coated Au substrates has not previously been identified. However, other recent studies indicate the presence of other forms of oxidized sulfur on these types of thiolated surfaces.[12-14]

We believe this structure results from the oxidation of the thiolate at Au to cyclo-S_8 during prolonged monolayer formation and exposure to air. Evidence for the cyclo-S_8 species is given by STM. The presence of a structure, which we refer to as the square structure, is observed. Each square consists of eight bright spots with the shape and distances comparable to those in a cyclo-S_8 molecule. The $(\sqrt{3} \times \sqrt{3})R30°$ structure, which has

recently been reported as the predominant structure observed on these samples,[2,3,7-9] continues to remain so at short (<2 days) exposures to laboratory ambient and usual monolayer formation times (<1 day). The square structure obtained by STM, however, is observed more often when the sample has been formed longer and has been exposed to the laboratory ambient for greater amounts of time. The electrochemical reductive desorption indicates the presence of another species on the surface, which, when compared to a layer made from a solution of elemental sulfur, has a peak position similar to the sulfur desorption peak potential.

EXPERIMENTAL

Substrate Preparation.

Gold substrates with a predominantly (111) crystallinity were prepared by the resistive evaporation of 300 nm of gold onto freshly cleaved green mica sheets (Asheville-Schoonmaker, Newport News, VA) as previously described.[2] The gold substrates were then immediately immersed into the thiol solutions. Previous characterizations of the Au films by STM,[2,15,16] underpotential deposition of Pb(II),[17] and electron diffraction,[15,18] indicate that the primary surface structure is the (111) crystal face.

Monolayer Film Preparation.

Monolayers of the alkanethiolates were prepared by the chemisorption of the corresponding thiol on Au from ~1 mM ethanolic solutions using previously described protocols.[19] Upon removal from solution, the samples were rinsed thoroughly with ethanol and dried in air. The molecular sulfur species were adsorbed onto the Au substrates by immersing the Au into a saturated CCl_4 solution of elemental sulfur.

Instrumentation.

STM. Images taken by STM were obtained in air using a Digital Instruments Nanoscope II (Santa Barbara, CA). The instrument was equipped with a 0.7 μm STM scan head. All atomic resolution images were obtained in the constant height scanning mode. The tips used were

fabricated by etching electrolytically a 0.01 in. diameter tungsten wire (Aldrich) in a 1 M KOH solution. The lateral distances in these images were determined by using highly ordered pyrolytic graphite (HOPG) for calibration. (All images are raw data, smoothed with and eight-point moving-algorithm (low-pass filtered), or XY spectrum filtered, as noted.)

Electrochemical Measurements. Electrochemical reductive desorption measurements were performed in 0.5 M KOH solutions using a Cypress Systems model CYSY-1 computer controlled potentiostat (Lawrence, KS). Measurements were obtained in a conventional three-electrode cell with an exposed area of 0.55 cm^2, which was defined by the diameter of a Teflon O-ring. All potential measurements are reported with respect to a Ag/AgCl/sat'd KCl electrode. The scan rate was 0.1 V/s.

Reagents.

The octadecanethiol (Aldrich) was recrystallized twice from absolute ethanol. The KOH (Aldrich, 99.99%), absolute ethanol (Midwest Grains), carbon tetrachloride (Fisher) and crystalline sulfur (Fisher) were used as received. The octadecanethiol-d_{37} was synthesized in our lab.

RESULTS AND DISCUSSION

Figure 1 is an STM image of the octadecanethiolate (OT) monolayer at Au presenting the $(\sqrt{3} \times \sqrt{3})R30°$ adsorbate structure on a Au(111) crystal face, a similar image has been presented previously.[2] This structure is the predominant structure observed on OT samples which have been formed <24 hrs and have been exposed to room ambient for <2 days. Although this structure is occasionally observed on older samples (>2 days) and on those formed >24 hrs, another structure becomes more prominent. This second structure, which has been observed using STM, is shown in Figure 2 and resembles squares. Figure 2c contains an enlarged image of this square structure. Each square consists of eight spots having three spots along each side and a spacing of 0.20-0.25 nm between the spots. Each side of the square is 0.40-0.50 nm long. The intensity of the spots usually varies, with every other spot being brighter, due perhaps to a difference in the tunneling orbitals or a difference in height. The shape of these squares are similar to that of the elemental cyclo-S_8. A representation of the cyclo-S_8 molecule from the top view is shown in Figure 3a. The top view looks very similar to a square and to the observed STM images with every other S atom raised. However, small differences in the S-S distances (the free form of cyclo-S_8 has 0.338 nm per side of each "square") exist, but it is reasonable to assume some variance in S-S distances from the free form to the Au-bound form. The orientation of these squares with respect to the underlying Au(111) lattice has not yet been determined.

Figure 1. A 3.01 x 3.01 nm^2 STM image of octadecanethiolate at Au(111) demonstrating the $(\sqrt{3} \times \sqrt{3})R30°$ structure which is the predominant structure observed on fresh samples of alkanethiolates at Au(111). The nearest-neighbor and next-nearest-neighbor spacings are 0.50 nm and 0.87 nm, respectively. The tunneling current is 2 nA and bias voltage -200 mV. This image is XY spectrum filtered.

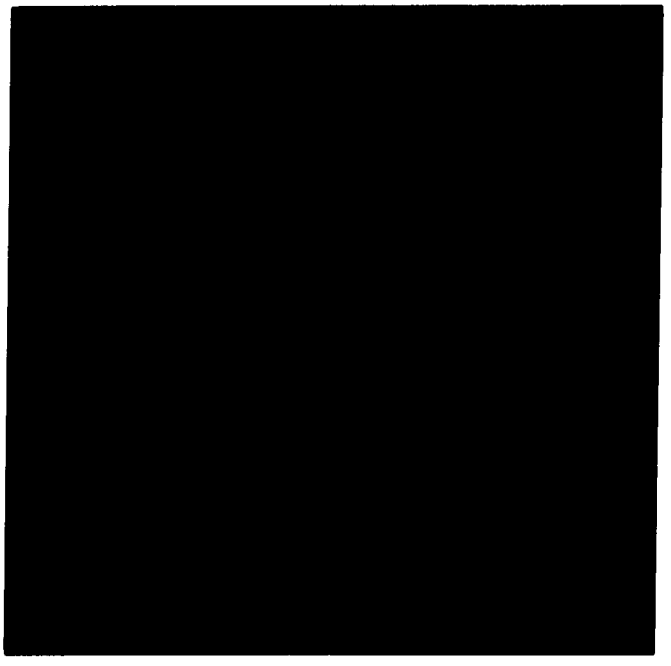

Figure 2. (a, top figure) A 7.01 x 7.01 nm^2 STM image of an aged octadecanethiolate at Au(111) sample. (b, bottom figure) The same sample as (a) but obtained 15 sec. later. Both (a) and (b) are raw data. The tunneling parameters are: I = 2 nA, V = -200 mV.

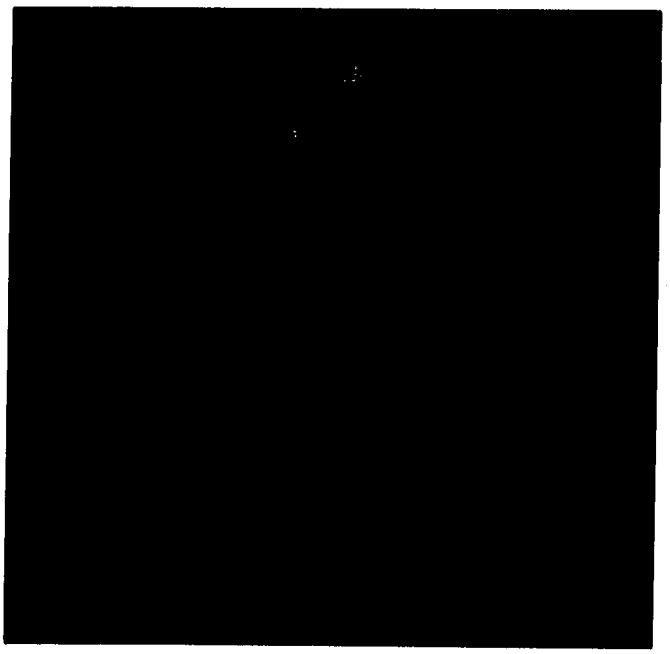

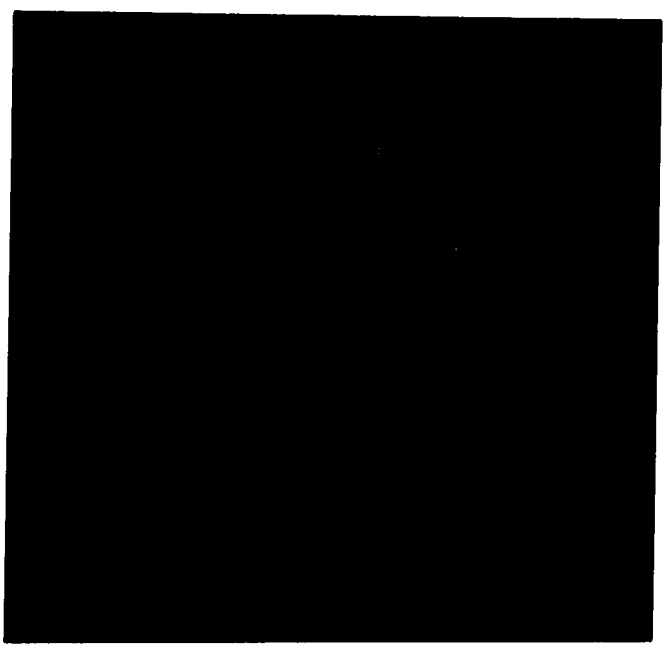

Figure 2 (cont'd). (c, upper figure) A 3.01 x 3.01 nm^2 STM image showing the details of the individual square structures shown in (a). A cross-section along the line in (c) is shown in (d, lower figure). The distance across a square, as noted by the markers, is 0.48 nm. The image in (c) is lowpass filtered. The tunneling parameters are: I = 4 nA, V = 10 mV.

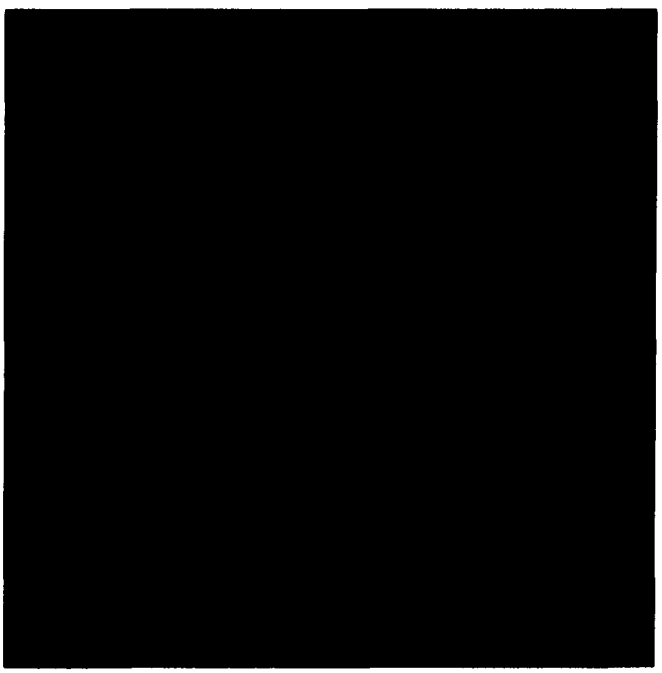

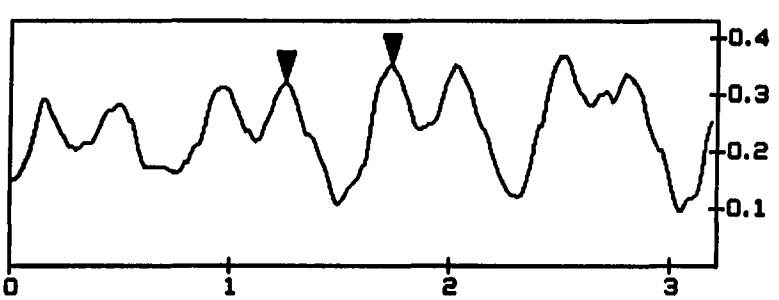
0.4
0.3
0.2
0.1
0
1
2
3

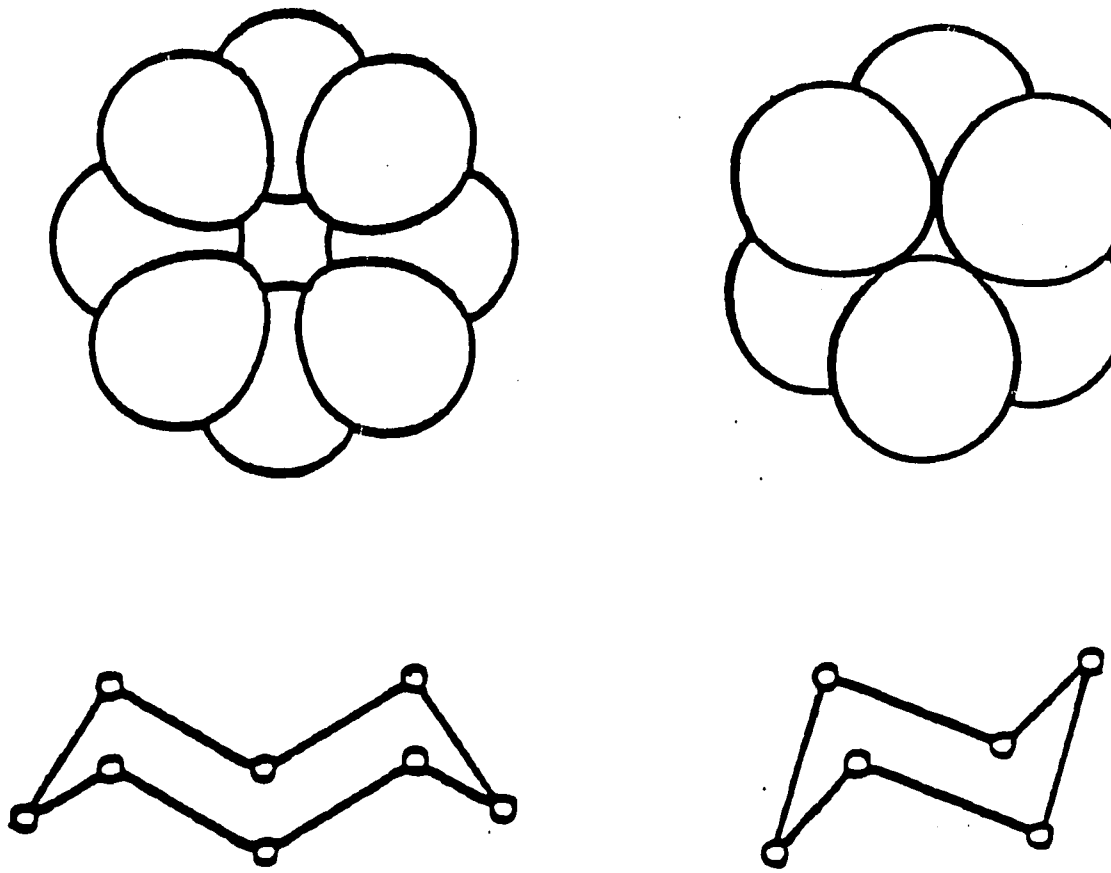

Figure 3. (a) Two representations of a cyclo-S_8 molecule. A top view is shown in the upper portion and reveals the similarity to the square structure. (b) Two representations of cyclo-S_6. Again, the upper portion is a top view representation.

To determine if elemental sulfur does take this form on the Au surface, a layer of elemental sulfur (cyclo-S_8 being the primary allotrope in such a solution[20]) was adsorbed onto Au by immersion in a CCl_4 solution. Figure 4 contains STM images of such a sample. Note the similarity to the images in Figure 2. The lengths of the sides of the squares (0.40 - 0.50 nm) are also comparable. This similarity indicates that the square structures observed for the OT monolayers are very likely due to cyclo-S_8. Also observed on the elemental sulfur layer are shapes other than the squares, such as octagons, diamonds, and rows of spots (Figure 4b). We attribute these other shapes to the different allotropes of elemental sulfur.

We have also found evidence for the formation of other allotropes of sulfur on thiolate-coated surfaces. During the investigation of ethanethiolate, a different structure was observed, one we refer to as the trimer structure. This structure is shown in Figure 5. The image contains rows of what appear to be clusters of three spots. Currently, we are unsure if these are due to the cyclo-S_6 sulfur allotrope, another fairly stable allotrope (represented in Figure 3b), or S_3 clusters. In the study of the adsorption of S on Re(0001), these S_3 clusters were formed.[21] These clusters were in a close-packed arrangement. It is possible that we have the same cluster formation. Why these clusters or molecules are not in a closest-packed arrangement is not clear. However, the structure appears to be stable and does not change with prolonged scanning. We have not observed this structure on any other thiolate surfaces. Perhaps the unique nature of ethanethiolate, with a very short alkyl tail group, allows this structure to form.

Figure 4. Two STM images of elemental sulfur adsorbed on Au(111). (a, upper figure) A 6 x 6 nm^2 image showing the square structure present on the surface. (b, lower figure) A 5.8 x 5.8 nm^2 image showing individual squares, but also several other shapes and arrangements. Both are raw data. The tunneling parameters are: (a) I = 2 nA, V = -200 mV; (b) I = 22 nA, V= 14 mV.

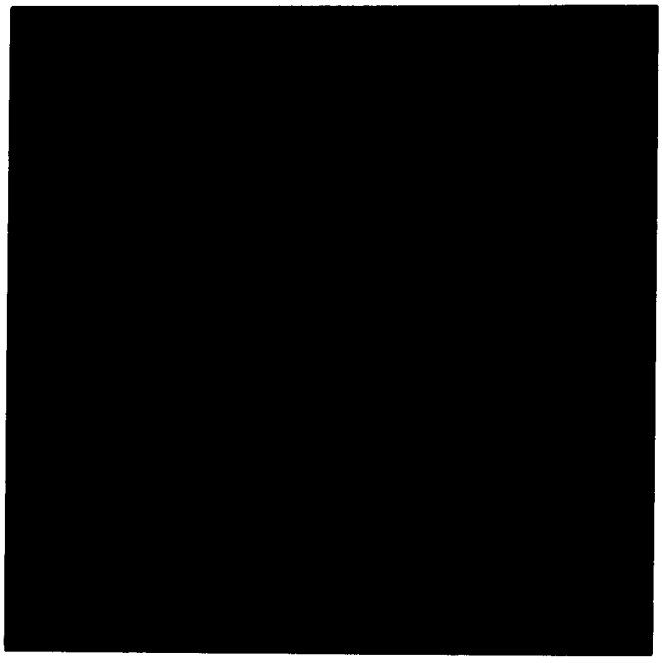

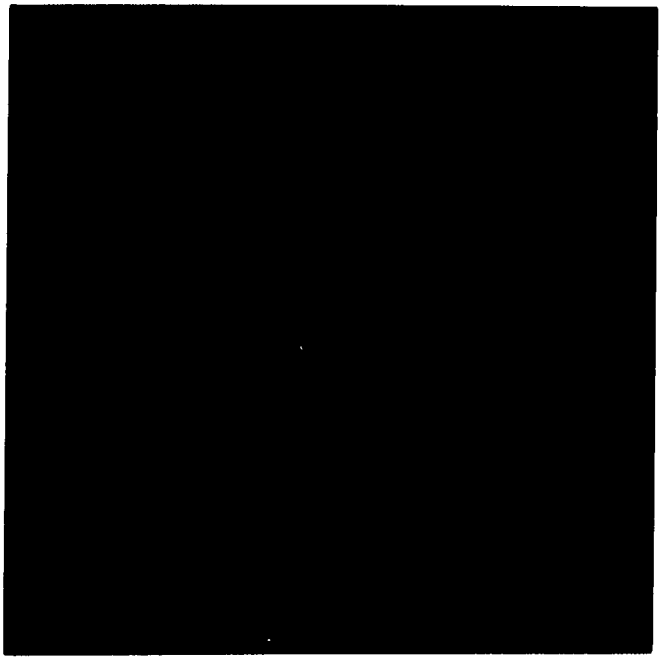

Figure 5. A 6.07 x 6.07 nm^2 STM image of ethanethiolate at Au(111). The distance between the trimers is 1.06 nm in the vertical direction. This is XY spectrum filtered and the tunneling parameters are I = 2 nA and V = 200 mV.

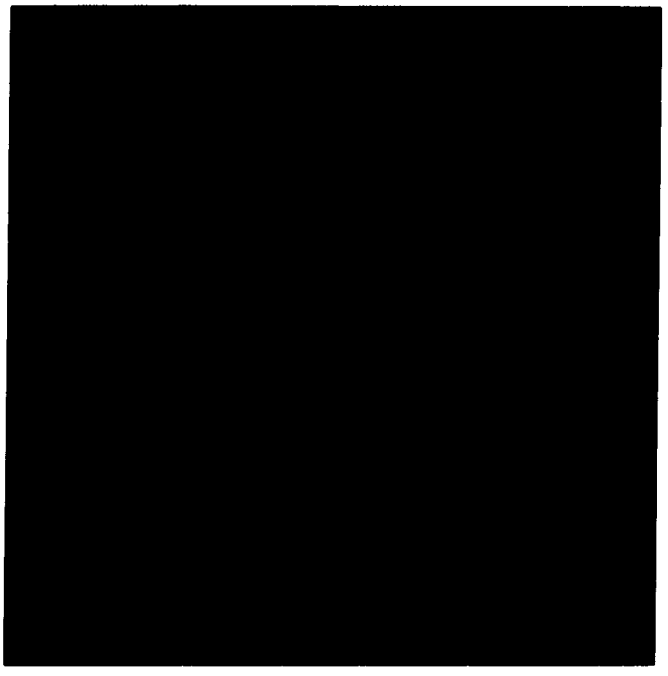

A possible mechanism for the formation of the S_8 molecule is the oxidation of the thiolate due to atmospheric oxygen. It is evident that the longer the monolayer has been exposed to the ambient, either in air or in the thiol solution, the more frequent the observation of the square structure by STM. Also, the square structure for the OT monolayer tends to occur frequently in small patches, ~7x7 nm^2, and in single rows, suggesting the formation at defect sites in the monolayer or along step edges, likely sites for the oxidation process to begin.[17] On occasion large areas (>15x15 nm^2) have been observed. These larger patches tend to be very well-ordered and in a closest-packed arrangement with little or no space between molecules and occasionally contain shapes other than the squares.

The role, if any, of the STM tip on the formation of the square structure cannot be delineated. There are precedents of tip-induced transformations of surfaces[22-25] but we believe this is not the sole factor in the formation of cyclo-S_8 on the thiolated Au surface. Experimentally, we have found large areas (>15x15 nm^2) which contain this square structure immediately upon scanning that area. If this structure were solely tip-induced, it would take time for this reaction and rearrangement of atoms to occur and such an observation would not be likely. However, it is possible that once the oxidation process begins in air, the tunneling process accelerates or completes the reaction.

It is apparent that the tip does play a role in orienting the molecules with respect to each other, although it is probably not the sole driving force. Experimental evidence is presented in Figure 2b which shows an STM image

of a well-packed array of molecules over the same area as that in Figure 2a. However, the image in Figure 2b was taken 15 sec later than the one in Figure 2a after continuous scanning (~5 scans). Note the square at the center left has essentially been pushed into a closest-packed position. Once such an arrangement of squares is achieved it is usually stable and further scanning does not noticeably degrade the packing structure.

On occasion, an OT sample which has been observed by STM to contain the square structure, exhibits the $(\sqrt{3} \times \sqrt{3})R30°$ structure when subsequently examined by AFM. This argues that both structures are present on the same surface, although it is uncertain to what extent each exists. The reason why this square structure is not observed by AFM could be due to the different part of the monolayer imaged by each technique. The AFM, which scans near the end of the alkyl chains, would be less sensitive to changes at the Au/S interface than the STM, which is thought to be tunneling near the Au-bound sulfur.[2] Also, the oxidation process, which severs the carbon-sulfur bond, leaves an alkane reaction product. Where this product goes after the reaction is uncertain. It could be laying on top of the oxidized sulfur species allowing only this disordered arrangement of alkane chains to be scanned by the AFM. However, the STM can essentially plow through this alkane layer and tunnel through to the sulfur. It is also possible that there is some function that the tunneling process plays in completing the oxidation process and allowing the formation of the cyclo-S_8 species. Whatever the reason, it is clear that the thiolate species and the oxidized form coexist on the Au surface.

An attempt to quantify the extent to which each species is present on the surface was made by performing the electrochemical reductive desorption of the monolayer from the Au surface. This technique can be used to determine the coverage of the thiolate monolayer according to the reaction[11]

$$RS\text{-}Au + 1e^- \rightarrow RS^- + Au(0), \quad (1)$$

as well as identify the presence of different species on the surface. Figure 6 contains the desorption current-potential (i-E)
curves for OT monolayers at Au with each curve representing different exposures to laboratory ambient. Curve (a) represents the desorption from an OT at Au sample in which the monolayer was formed in solution for 3 hrs and exposed to air 3 hrs. A desorption wave at about –1.15 V is observed with the charge enclosed by the peak (38.6 μC) corresponding to a coverage of 7.3×10^{-10} mol/cm^2. This is consistent for a full monolayer of coverage on Au(111) for the $(\sqrt{3} \times \sqrt{3})R30°$ structure. Curves (b) and (c) in Figure 6 represent OT monolayers at Au exposed to 1 day in solution and 3 days in air, and 4 days in solution and 2 hrs in air, respectively. Note that each curve shows a broadening of the wave at about –1.15 V in the positive direction. This broadening could be a result of the increased defectiveness in the thiolate monolayer as a result of increased oxidation and explained as a loss of neighbor interactions.[26]

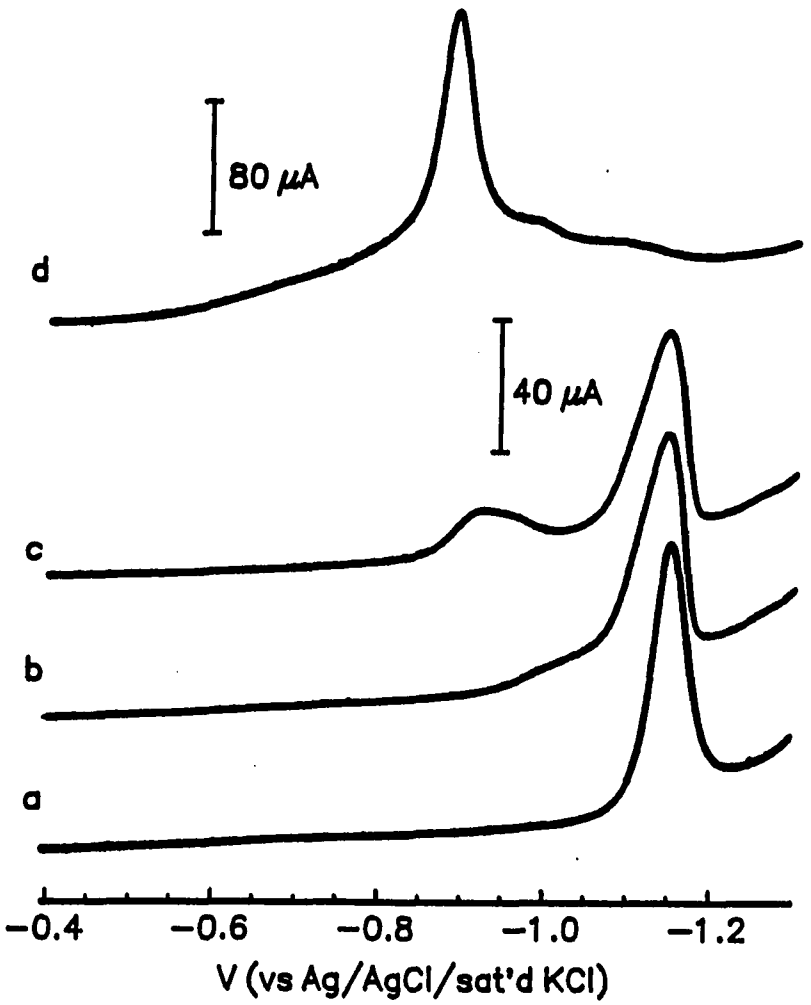

Figure 6. A series of i-E curves for octadecanethiolate at Au(111). (a) An OT monolayer formed in solution 3 hrs and exposed to air for 3 hrs. (b) An OT monolayer formed in solution 1 day and exposed to air for 3 days. (c) An OT monolayer formed in solution 4 days and exposed to air for 3 hrs. (d) An elemental sulfur layer formed in solution 1 day and exposed to air for 3 hrs.

A new reductive peak forms upon increased exposure to air. Curve (b) has a small peak at about –1.02 V and curve (c) has a peak at about –0.9 V. Neither of these peaks are present in the i-E curve of the fresh OT monolayer and indicate the presence of another species on the surface. The charge enclosed by the peaks at about –1.15 V for curves (b) and (c) are 36.3 μC and 35.0 μC respectively, corresponding to coverages of 6.8×10^{-10} mol/cm^2 and 6.6×10^{-10} mol/cm^2. These differences are relatively small compared to the error in obtaining the measurements (typically $\pm$ 0.9×10^{-10} mol/cm^2). Thus, at this point, the reductive desorption can not provide quantitative information to determine the extent of oxidation of the thiolate monolayers. However, it is clearly evident that a second species is present on the surface.

The i-E curve (d) in Figure 6 is for elemental sulfur (S_8) adsorbed on Au. The largest peak occurs at about –0.9 V, but other smaller peaks appear at about –0.95 V and about –1.05 V, possibly indicating the presence of several elemental sulfur allotropes on the surface or different adsorption sites of S_8 on the Au surface.[17] The position of the small peaks present on the oxidized OT sample (curves (b) and (c)) are in similar positions as that for elemental sulfur. Although it is clear a second species is on the thiolate surface, it is unclear if that desorption wave is actually for a polysulfur molecule. It may be that some of the oxidized sulfur species are not electroactive and do not desorb electrochemically. A recent study[27] reveals that for sulfide adsorbed on Au, polyatomic sulfur is formed under potential control and desorbs by a two electron process. The potential of this desorption is about –0.9 V, the same potential as the desorption peak in curve (d). Also, an STM study of

sulfide adsorbed at Au under potential control[28] has revealed a structure which is similar to the square structure observed here and has an electrochemical response which correlates to the formation of polyatomic sulfur.

It is thus clearly evident from STM and electrochemical desorption that a second species exists on the surface and is the elemental sulfur allotrope, cyclo-S_8. Studies of these samples using infrared reflection spectroscopy indicate no difference between fresh OT samples and those exposed to solution and laboratory ambient for up to least two weeks. Thus, the evidence for the oxidation process is only on the microscopic scale at these exposure times.

CONCLUSION

The presence of a second sulfur species that forms upon prolonged exposure to laboratory ambient, cyclo-S_8, has been observed on OT monolayers at gold. There is also evidence indicating other species as well. This degradation of the OT monolayer films upon exposure to air puts into question the long-term stability of these films and implies that these monolayers may not be useful for technological development. Further experiments are underway to determine the mechanism of the oxidation process as well as to further quantify it. Continued electrochemical investigation, including in-situ STM and AFM, are underway.

ACKNOWLEDGMENTS

MDP gratefully acknowledges the support of a Dow Corning Assistant Professorship. C.A. Alves acknowledges Phillips Petroleum for a graduate fellowship. Ames Laboratory is operated for the U.S. Department of Energy by Iowa State University under Contract No. W-7405-eng-82. This work was supported by the Office of Basic Energy Sciences, Chemical Science Division.

REFERENCES

1. The (111) crystalline face of Au has been determined to be the predominant structure on Au films on mica.
2. Widrig, C. A.; Alves, C. A.; Porter, M. D. *J. Am. Chem. Soc.* **1991**, *113*, 2805-10.
3. Alves, C. A.; Smith, E. L.; Porter, M. D. *J. Am. Chem. Soc.* **1992**, *114*, 1222-7.
4. Kim, Y.-K.; McCarley, R. L.; Bard, A. L. *J. Chem. Phys.* **1992**, submitted.
5. Porter, M. D.; Bright, T. B.; Allara, D. L.; Chidsey, C. E. D. *J. Am. Chem. Soc.* **1987**, *109*, 3559-68.
6. Bryant, M. A.; Pemberton, J. E. *J. Am. Chem. Soc.* **1991**, *113*, 8284-8293.
7. Strong, L.; Whitesides, G. M. *Langmuir* **1988**, *4*, 546-58.
8. Chidsey, C. E. D.; Loiacono, D. M. *Langmuir* **1990**, *6*, 682-691.
9. Chidsey, C. E. D.; Liu, G.-Y.; Rowntree, P.; Scoles, G. J. *J. Chem. Phys.* **1989**, *91*, 4421-4423.
10. Samant, M. G.; Brown, C. A.; Gordon, J. G., II *Langmuir* **1991**, *7*, 437-439.
11. Widrig, C. A.; Chung, C.; Porter, M. D. *J. Electroanal. Chem.* **1991**, *310*, 335-59.
12. Li, Y.; Huang, J.; McIver, R. T., Jr. *J. Am. Chem. Soc.* **1992**, *114*, 2428-2432.
13. Tarlov, M. J.; Newman, J. G. *Languir* **1992**, *8*, 1398-1405.

14. Weisshaar, D. E.; Walczak, M. M.; Porter, M. D. *Langmuir* **1992**, submitted.

15. Hallmark, V. M.; Chiang, S.; Rabolt, J. F.; Swalen, J. D.; Wilson, R. J. *Phys. Rev. Lett.* **1987**, *59*, 2879-82.

16. Emch, R.; Nogami, J.; Dovek, M. M.; Lang, C. A.; Quate, C. F. *J. Appl. Phys.* **1989**, *65*, 79-84.

17. Walczak, M. M.; Alves, C. A.; Lamp, B. D.; Deinhammer, R. S.; Porter, M. D. **1992**, in preparation.

18. Chidsey, C. E. D.; Loiacono, D. N.; Sleator, T.; Nakahara, S. *Surf. Sci.* **1988**, *200*, 45-66.

19. Walczak, M. M.; Chung, C.; Stole, S. M.; Widrig, C. A.; Porter, M. D. *J. Am. Chem. Soc* **1991**, *113*, 2370-8.

20. Meyer, B. In *Elemental Sulfur*; B. Meyer, Ed.; Interscience: New York, 1965.

21. Ogletree, D. F.; Hwang, R. Q.; Zeglinski, D. M.; Vazquez-de-Parga, A. L.; Somorjai, G. A.; Salmeron, M. *J. Vac. Sci. Technol. B* **1991**, *9*, 886-890.

22. Staufer, U.; Scandella, L.; Rudin, H.; Guntherodt, H.-J.; Garcia, N. *J. Vac. Sci. Technol. B* **1991**, *9*, 1389-1393.

23. Ehrichs, E. E.; Smith, W. F.; de Lozanne, A. L. *J. Vac. Sci. Technol. B* **1991**, *9*, 1380-1383.

24. Mizutani, W.; Shigeno, M.; Ohmi, M.; Suginoya, M.; Kajimura, K.; Ono, M. *J. Vac. Sci. Technol. B* **1991**, *9*, 1102-1106.

25. Mamin, H. J.; Chiang, S.; Birk, H.; Guethner, P. H.; Rugar, D. *J. Vac. Sci. Technol. B* **1991**, *9*, 1398-1402.

26. Brown, A. P.; Anson, F. C. *Anal. Chem.* **1977**, *49*, 1589-1595.

27. Gao, X.; Zhang, Y.; Weaver, M. J. *J. Phys. Chem.* **1992**, *96*, 4156-4159.

28. Gao, X.; Zhang, Y.; Weaver, M. J. *J. Phys. Chem.* **1992**, *96*, 4156-4159.

SUMMARY AND DISCUSSION

The microscopic characterization of self-assembled thiolate monolayers at epitaxially grown Au(111) films on mica was performed. Alkanethiolates were found to exhibit a $(\sqrt{3} \times \sqrt{3})R30°$ packing structure on Au(111) as observed by both scanning tunneling (STM) and atomic force microscopies (AFM). The fluorinated thiol, $CF_3(CF_2)_7(CH_2)_2SH$, however, was found to exhibit a (2 x 2) adlayer structure at Au(111), a structure consistent with the van der Waals diameter of the fluorinated chain. Complementary electrochemical coverage determinations reveal a surface coverage which agrees with this (2 x 2) arrangement. Evidence for the oxidation of these thiolate monolayers at Au(111) was revealed using STM. A structure was observed which closely resembled that of cyclooctasulfur. Electrochemical evidence was also found to support the presence of this species, while infrared reflection spectroscopy provided no evidence for a change in the adsorbed species. Thus, the importance of microscopic characterization is evident.

Finally, the study of these seemingly simple monolayer systems is quite a complex process. Macroscopic techniques have provided information as to bulk properties and several surface properties. The STM and AFM have allowed these systems to be studied at a molecular level for the first time, allowing confirmation of previous structural data. However, STM and AFM not only confirm previous findings, but have allowed new information to be gained. Because of this, the evolution of STM and AFM continues. Each day

more applications are found for these techniques and their popularity increases. Much emphasis is being place on the in situ characterization of surfaces (i.e. in water or other liquids). In this way, dynamic processes, such as adsorption on surfaces or biological processes, can be studied in real time at the molecular level. Such investigation would be useful in further characterizing the thiolate monolayer systems presented in this dissertation. Also, when studying systems in situ, it becomes possible to provide potential control of the surface of interest, a property which is useful in the study of electrochemical properties. With all of these applications, it is clear that the STM and AFM are invaluable techniques and have limitless potential.

REFERENCES

1. Binnig, G.; Rohrer, H.; Gerber, C.; Weibel, E. *Phys. Rev. Lett.* **1982**, *49*, 57.
2. Binnig, G.; Quate, C. F.; Gerber, C. *Phys. Rev. Lett.* **1986**, *56*, 930-933.
3. Hansma, P. K.; Tersoff, J. *J. Appl. Phys.* **1987**, *61*, R1-R23.
4. Tersoff, J.; Hamann, D. R. *Phys. Rev. B* **1985**, *31*, 805-813.
5. Bardeen, J. *Phys. Rev. Lett.* **1961**, *6*, 57.
6. Tersoff, J. *Phys. Rev. B* **1989**, *39*, 1052.
7. Tersoff, J. *Phys. Rev. B* **1989**, *40*, 11 990.
8. Binnig, G.; Rohrer, H.; Salvan, F.; Gerber, C.; Baro, A. *Surf. Sci.* **1985**, *157*, L373.
9. Feenstra, R. M.; Stroscio, J.; Tersoff, J.; Fein, A. *Phys. Rev. Lett.* **1987**, *58*, 1192.
10. Tersoff, J. *Phys. Rev. B* **1990**, *41*, 1235.
11. Tromp, R. M.; van Loenen, E.; Demuth, J.; Lang, N. *Phys. Rev. B* **1988**, *37*, 9042.
12. Binnig, G.; Rohrer, H.; Gerber, C.; Weibel, E. *Surf. Sci.* **1983**, *131*, L379.
13. Robinson, I. K. *Phys. Rev. Lett.* **1983**, *50*, 1145.
14. Kuk, Y. *Bull. Am. Phys. Soc.* **1983**, *28*, 260.
15. Lang, N. D. *Phys. Rev. Lett.* **1986**, *56*, 1164-1167.
16. Lang, N. D. *Phys. Rev. Lett.* **1985**, *55*, 230-233.
17. Sacks, W.; Noguera, C. *J. Microsc.* **1988**, *152*, 23.
18. Stroscio, J.; Feenstra, R.; Fein, A. *Phys. Rev. Lett.* **1986**, *57*, 2579.

19. Stroscio, J.; Feenstra, R.; Fein, A. *Surf. Sci.* **1987**, *181*, 295.

20. Brodde, A.; Tosch, S.; Neddermeyer, H. *J. Microsc.* **1988**, *152*, 441.

21. Wintterlin, J.; Wiechers, J.; Brune, H.; Gritsch, T.; Hofer, H.; Behm, R. *Phys. Rev. Lett.* **1989**, *62*, 59.

22. Hallmark, V.; Chiang, S.; Rabolt, J.; Swalen, J.; Wilson, R. *Phys. Rev. Lett.* **1987**, *59*, 2879-2882.

23. Caroli, C.; Combescot, R.; Nozieres, P.; Saint-James, D. *J. Phys. C* **1971**, *4*, 916, 2598.

24. Feuchtwang, T. E. *Phys. Rev. B* **1974**, *10*, 4121.

25. Combescot, R. *J. Phys. C* **1971**, *4*, 2611.

26. Ciraci, S.; Batra, I. *Phys. Rev. B* **1987**, *36*, 6194.

27. Ciraci, S.; Baratoff, A.; Batra, I. *Phys. Rev. B* **1990**, *41*, 2763.

28. Lucas, A.; Morawitz, H.; Henry, G.; Vigneron, J. P.; Lambin, P.; Cutler, P.; Feuchtwang, T. *Phys. Rev. B* **1988**, *37*, 10 708.

29. Kopatzki, E.; Doyen, G.; Drakova, D.; Behm, R. *J. Microsc.* **1988**, *152*, 687.

30. Doyen, G.; Koetter, E.; Vigneron, J. P.; Scheffler, M. *Appl. Phys. A* **1990**, *51*, 281.

31. Stoll, E.; Baratoff, A.; Selloni, A.; Carnevali, P. *J. Phys. C* **1984**, *17*, 3073.

32. Emch, R.; Nogami, J.; Dovek, M. M.; Lang, C. A.; Quate, C. F. *J. Appl. Phys.* **1989**, *65*, 79-84.

33. Woll, C.; Chiang, S.; Wilson, R. J.; Lippel, P. H. *Phys. Rev. B* **1989**, *39*, 7988-7991.

34. DeRose, J. A.; Thundat, T.; Nagahara, L. A.; Lindsay, S. M. *Surf. Sci.* **1991**, *256*, 102-108.

35. Holland-Moritz, E.; Gordon II, J.; Borges, G.; Sonnenfeld, R. *Langmuir* **1991**, *7*, 301-306.

36. Holland-Moritz, E.; Gordon II, J.; Kanazawa, K.; Sonnenfeld, R. *Langmuir* **1991**, *7*, 1981-1987.

37. Lang, C. A.; Dovek, M. M.; Nogami, J.; Quate, C. F. *Surf. Sci.* **1989**, *224*, L947-L955.

38. Trevor, D. J.; Chidsey, C. E. D.; Loiacono, D. N. *Phys. Rev. Lett.* **1989**, *62*, 929-932.

39. Honbo, H.; Sugawara, S.; Itaya, K. *Anal. Chem.* **1990**, *62*, 2424-2429.

40. Gao, X.; Hamelin, A.; Weaver, M. J. *J. Chem. Phys.* **1991**, *95*, 6993-6996.

41. Hwang, R. Q.; Behm, R. J. *J. Vac. Sci. Technol. B* **1992**, *10*, 256-261.

42. Magnussen, O. M.; Hotlos, J.; Nichols, R. J.; Kolb, D. M.; Behm, R. J. *Phys. Rev. Lett.* **1990**, *64*, 2929-2932.

43. Vitus, C. M.; Chang, S.-C.; Schardt, B. C.; Weaver, M. J. *J. Phys. Chem.* **1991**, *95*, 7559-7563.

44. Yau, S.-L.; Vitus, C. M.; Schardt, B. C. *J. Am. Chem. Soc.* **1990**, *112*, 3677-3679.

45. Schardt, B. C.; Yau, S.-L.; Rinaldi, F. *Science* **1989**, *243*, 1050-1053.

46. Ogletree, D. F.; Ocal, C.; Marchon, B.; Somorjai, G. A.; Salmeron, M.; Beebe, T.; Siekhaus, W. *J. Vac. Sci. Technol. A* **1990**, *8*, 297-301.

47. Ogletree, D. F.; Hwang, R. Q.; Zeglinski, D. M.; Vazquez-de-Parga, A. L.; Somorjai, G. A.; Salmeron, M. *J. Vac. Sci. Technol. B* **1991**, *9*, 886-890.

48. Marchon, B.; Bernhardt, P.; Bussell, M. E.; Somorjai, G. A.; Salmeron, M.; Siekhaus, W. *Phys. Rev. Lett.* **1988**, *60*, 1166-1169.

49. Green, M. P.; Hanson, K. J.; Carr, R.; Lindau, I. *J. Electrochem. Soc.* **1990**, *137*, 3493-3498.

50. Scott, E. R.; White, H. S.; McClure, D. J. *J. Phys. Chem.* **1989**, *93*, 5249-5253.

51. Becker, R. S.; Swartzentruber, B. S.; Vickers, J. S. *J. Vac. Sci. Technol. A.* **1988**, *6*, 472-477.

52. Avouris, P.; Wolkow, R. *Phys. Rev. B* **1989**, *39*, 5091-5100.

53. Kohler, U.; Jusko, O.; Pietsch, G.; Muller, B.; Henzler, M. *Surf. Sci.* **1991**, *248*, 321-331.

54. Biegelsen, D. K.; Bringans, R. D.; Northup, J. E.; Swartz, L. E. *Appl. Phys. Lett.* **1990**, *57*, 2419-2421.

55. Whitman, L. J.; Stroscio, J. A.; Dragoset, R. A.; Celotta, R. J. *J. Vac. Sci. Technol. B* **1991**, *9*, 770-774.

56. Ohtani, H.; Wilson, R. J.; Chiang, S.; Mate, C. M. *Phys. Rev. Lett.* **1988**, *60*, 2398-2401.

57. Lippel, P. H.; Wilson, R. J.; Miller, M. D.; Woll, C.; Chiang, S. *Phys. Rev. Lett.* **1989**, 171-174.

58. Hallmark, V. M.; Chiang, S.; Brown, J. K.; Woll, C. *Phys. Rev. Lett.* **1991**, *66*, 48-51.

59. Hallmark, V. M.; Chiang, S.; Woll, C. *J. Vac. Sci. Technol. B* **1991**, *9*, 1111-1114.

60. Widrig, C. A.; Alves, C. A.; Porter, M. D. *J. Am. Chem. Soc.* **1991**, *113*, 2805-10.

61. Sotobayashi, H.; Schilling, T.; Tesche, B. *Langmuir* **1990**, *6*, 1246-1250.

62. Smith, D. P. E.; Bryant, A.; Quate, C. F.; Rabe, J. P.; Gerber, C.; Swalen, J. D. *Proc. Natl. Acad. Sci. USA* **1987**, *84*, 969-972.

63. Lang, C. A.; Horber, J. K. H.; Hansch, T. W.; Heckl, W. M.; Mohwald, H. *J. Vac. Sci. Technol. A* **1988**, *6*, 368-370.

64. Smith, D. P. E.; Horber, J. K. H.; Binnig, G.; Nejoh, H. *Nature* **1990**, *344*, 641-644.

65. Yang, R.; Naoi, K.; Evans, D. F.; Smyrl, W. H.; Hendrickson, W. A. *Langmuir* **1991**, *7*, 556-558.

66. Watson, B. A.; Barteau, M. A.; Haggerty, L.; Lenhoff, A. M.; Weber, R. S. *Langmuir* **1992**, *8*, 1145-1148.

67. Wu, X.-L.; Lieber, C. M. *J. Phys. Chem.* **1988**, *92*, 5556-5557.

68. Mou, J.; Sun, W.; Yan, J.; Yang, W. S.; Liu, C.; Zhai, Z.; Xu, Q.; Xie, Y. *J. Vac. Sci. Technol. B.* **1991**, *9*, 1566-1569.

69. Miles, M. J.; McMaster, T.; Carr, H. J.; Tatham, A. S.; Shewry, P. R.; Field, J. M.; Belton, P. S.; Jeenes, D.; Hanley, B.; Whittam, M.; Cairns, P.; Morris, V. J.; Lambert, N. *J. Vac. Sci. Technol. A* **1990**, *8*, 698-702.

70. Beebe, T. P. J.; Wilson, T. E.; Ogletree, D. F.; Katz, J. E.; Balhorn, R.; Salmeron, M. B.; Siekhaus, W. J. *Science* **1989**, *243*, 370-372.

71. Keller, R. W.; Dunlap, D. D.; Bustamante, C.; Keller, D. J.; Garcia, R. G.; Gray, C.; Maestre, M. F. *J. Vac. Sci. Technol. A* **1990**, *8*, 706-712.

72. Salmeron, M.; Beebe, T.; Odriozola, J.; Wilson, T.; Ogletree, D. F.; Siekhaus, W. *J. Vac. Sci. Technol. A* **1990**, *8*, 635-641.

73. Thundat, T.; Nagahara, L. A.; Oden, P.; Lindsay, S. M. *J. Vac. Sci. Technol. A* **1990**, *8*, 645-647.

74. Haussling, L.; Michel, B.; Ringsdorf, H.; Rohrer, H. *Angew. Chem. Int. Ed. Engl.* **1991**, *30*, 569-572.

75. Kittel, C. *Introduction to Solid State Physics*; 5 ed.; Wiley: New York, 1976.

76. Batra, I. P.; Barker, J. A.; Auerbach, D. J. *J. Vac. Sci. Technol. A* **1984**, *2*, 943.

77. Feenstra, R. M.; Thompson, W. A.; Fein, A. P. *Phys. Rev. Lett.* **1986**, *56*, 608.

78. Tersoff, J. *Phys. Rev. Lett.* **1986**, *57*, 440.

79. Kaiser, W. J.; Jaklevic, R. C. *Surf. Sci.* **1987**, *181*, 55.

80. Kaiser, W. J.; Jaklevic, R. C. *Surf. Sci.* **1987**, *182*, L227.

81. Woodruff, D. P.; Royer, W. A.; Smith, N. V. *Phys. Rev. B* **1986**, *34*, 764.

82. Perderau, J.; Biberian, J. P.; Rhead, G. E. *J. Phys. F* **1974**, 798.

83. Melle, H.; Menzel, E. *Z. Naturforsch.* **1978**, *33a*, 282.

84. Harten, U.; Lahee, A. M.; Toennies, J. P.; Woll, C. *Phys. Rev. Lett.* **1985**, *54*, 2619.

85. Hansma, P. K.; Elings, V. B.; Marti, O.; Bracker, C. E. *Science* **1988**, *242*, 209-216.

86. Weisenhorn, A. L.; Hansma, P. K.; Albrecht, T. R.; Quate, C. F. *Appl. Phys. Lett.* **1989**, *54*, 2651-2653.

87. Rugar, D.; Hansma, P. *Physics Today* **1990**, 23-30.

88. Sarid, D.; Elings, V. *J. Vac. Sci. Technol. B* **1991**, *9*, 431-437.

89. Martin, Y.; Williams, C. C.; Wickramasinghe, H. K. *J. Appl. Phys.* **1987**, *61*, 4723-4729.

90. Israelachvili, J. N. *Intermolecular and Surface Forces*; Academic Press: London, 1985.

91. Howells, S.; Chen, T.; Gallagher, M.; Yi, L.; Sarid, D. *J. Appl. Phys.* **1991**, *69*, 7330-7332.

92. Gould, S. A. C.; Burke, K.; Hansma, P. K. *Phys. Rev. B* **1989**, *40*, 5363-5366.

93. Burnham, N. A.; Dominguez, D. D.; Mowery, R. L.; Colton, R. J. *Phys. Rev. Lett.* **1990**, *64*, 1931-1934.

94. Blackman, G. S.; Mate, C. M.; Philpott, M. R. *Phys. Rev. Lett.* **1990**, *65*, 2270-2273.

95. Persson, B. N. J. *Chem. Phys. Lett.* **1987**, *141*, 366-368.

96. Abraham, F. F.; Batra, I. P.; Ciraci, S. *Phys. Rev. Lett.* **1988**, *60*, 1314-1317.

97. Abraham, F. F.; Batra, I. P. *Surf. Sci.* **1989**, *209*, L125-L132.

98. Albrecht, T. R.; Quate, C. F. *J. Appl. Phys.* **1987**, *62*, 2599.

99. Manne, S.; Butt, H. J.; Gould, S. A. C.; Hansma, P. K. *Appl. Phys. Lett.* **1990**, *56*, 1758-1759.

100. Weisenhorn, A. L.; Henriksen, P. N.; Chu, H. T.; Ramsier, R. D.; Reneker, D. H. *J. Vac. Sci. Technol. B* **1991**, *9*, 1333-1335.

101. Chen, C.; Gewirth, A. A. *J. Am. Chem. Soc.* **1992**, *114*, 5439-5440.

102. Chen, C.; Vesecky, S. M.; Gewirth, A. A. *J. Am. Chem. Soc.* **1992**, *114*, 451-458.

103. Manne, S.; Hansma, P. K.; Massie, J.; Elings, V. B.; Gewirth, A. A. *Science* **1991**, *251*, 183-186.

104. Weisenhorn, A. L.; Egger, M.; Ohnesorge, F.; Gould, S. A. C.; Heyn, S.-P.; Hansma, H. G.; Sinsheimer, R. L.; Gaub, H. E.; Hansma, P. K. *Langmuir* **1991**, *7*, 8-12.

105. Meyer, E.; Howald, L.; Overney, R. M.; Heinzelmann, H.; Frommer, J.; Guntherodt, H.-J.; Wagner, T.; Schier, H.; Roth, S. *Nature* **1991**, *349*, 398-400.

106. Bourdieu, L.; Silberzan, P.; Chatenay, D. *Phys. Rev. Lett.* **1991**, *67*, 2029-2032.

107. Mate, C. M.; Lorenz, M. R.; Novotny, V. J. *J. Chem. Phys.* **1989**, *90*, 7550-7555.

108. Saurenbach, F.; Wollmann, D.; Terris, B. D.; Diaz, A. F. *Langmuir* **1992**, *8*, 1199-1203.

109. Magonov, S. N.; Qvarnstrom, K.; Elings, V.; Cantow, H.-J. *Polymer Bull.* **1991**, *25*, 689-694.

110. Alves, C. A.; Smith, E. L.; Porter, M. D. *J. Am. Chem. Soc.* **1992**, *114*, 1222-7.

111. Egger, M.; Ohnesorge, F.; Weisenhorn, A. L.; Heyn, S. P.; Drake, B.; Prater, C. B.; Gould, S. A. C.; Hansma, P. K.; Gaub, H. E. *J. Struct. Biol.* **1990**, *103*, 89-94.

112. Drake, B.; Prater, C. B.; Weisenhorn, A. L.; Gould, S. A. C.; Albrecht, T. R.; Quate, C. F.; Cannell, D. S.; Hansma, H. G.; Hansma, P. K. *Science* **1989**, *243*, 1586-1589.

113. Bustamante, C.; Vesenka, J.; Tang, C. L.; Rees, W.; Guthold, M.; Keller, R. *Biochem.* **1992**, *31*, 22-26.

114. Hansma, H. G.; Vesenka, J.; Siegerist, C.; Kelderman, G.; Morrett, H.; Sinsheimer, R. L.; Elings, V.; Bustamante, C.; Hansma, P. K. *Science* **1992**, in press.

115. Gould, S. A. C.; Drake, B.; Prater, C. B.; W eisenhorn, A. L.; Manne, S.; Hansma, H. G.; Hansma, P. K.; Massie, J.; Longmire, M.; Elings, V.; Dixon Northern, B.; Mukergee, B.; Peterson, C. M.; Stoeckenius, W.; Albrecht, T. R.; Quate, C. F. *J. Vac. Sci. Technol. A* **1990**, *8*, 369-373.

116. Lin, J. N.; Drake, B.; Lea, A. S.; Hansma, P. K.; Andrade, J. D. *Langmuir* **1990**, *6*, 509-511.

117. Kaupp, G. *Angew. Chem. Int. Ed. Engl.* **1992**, *31*, 592-595.

118. Kaupp, G. *Angew. Chem. Int. Ed. Engl.* **1992**, *31*, 595-598.